# MORPHOGENESIS OF THE ARABIDOPSIS SHOOT APICAL MERISTEM

Thesis by

Cory James Tobin

In Partial Fulfilment of the Requirements

for the Degree of

Doctor of Philosophy

California Institute of Technology

Pasadena, California

2016

(Defended December 01, 2015)

# Abstract

Phyllotaxis patterns in plants, or the arrangement of leaves and flowers radially around the shoot, have fascinated both biologists and mathematicians for centuries. The current model of this process involves the lateral transport of the hormone auxin through the first layer of cells in the shoot apical meristem via the auxin efflux carrier protein PIN1. Locations around the meristem with high auxin concentration are sites of organ formation and differentiation. Many of the molecular players in this process are well known and characterized. Computer models composed of all these components are able to produce many of the observed phyllotaxis patterns. To understand which parts of this model have a large effect on the phenotype I automated parameter testing and tried many different parameter combinations. Results of this showed that cell size and meristem size should have the largest effect on phyllotaxis. This lead to three questions: (1) How is cell geometry regulated? (2) Does cell size affect auxin distribution? (3) Does meristem size affect phyllotaxis? To answer the first question I tracked cell divisions in live meristems and quantified the geometry of the cells and the division planes using advanced image processing techniques. The results show that cell shape is maintained by minimizing the length of the new wall and by minimizing the difference in area of the daughter cells. To answer the second question I observed auxin patterning in the meristem, shoot, leaves, and roots of Arabidopsis mutants with larger and smaller cell sizes. In the meristem and shoot, cell size plays an important role in determining the distribution of auxin. Observations of auxin in the root and leaves are less definitive. To answer the third question I measured meristem sizes and phyllotaxis patterns in mutants with altered meristem sizes. These results show that there is no correlation between meristem size and average divergence angle. But in an extreme case, making the meristem very small does lead to a switch on observed phyllotaxis in accordance with the model.

# Contents

# Chapter 1

# Analysis of Cell Divisions Patterns in the Arabidopsis Shoot Apical Meristem

## 1.1 Introduction

The Arabidopsis SAM is a structure at the tip of the shoot that is responsible for generating almost all of the above-ground tissue of the plant[1]. Its epidermal and subepidermal cells are organized into layers with very few cells moving between layers[2, 3]. When these cells expand they do so laterally, pushing other cells towards the periphery of the meristem. Division in these cells is anticlinal such that each layer remains one cell thick. Since plant cells are bound to each other by common walls and can't move past each other, the position of the walls created during cytokinesis is critical to patterning and morphogenesis at the tissue and organ level.

### 1.1.1 Qualitative Observations

While the underlying mechanisms that control positioning of the cell plate are not completely known (discussed in detail later), the qualitative properties of meristematic cell division are well documented. Perhaps the three most well known of these observations are those of the 19th century botanists Wilhelm Hofmeister, Léo Errera, and Julius von Sachs.

1. Errera observed that soap bubbles and plant cells often divide in much the same way; the plane of division corresponds to the shortest path that will halve the volume of the mother cell[4]. According to Errera (1888, section IV) the new wall will be a surface "mit constanter mittlerer Krümmung (= Minimalfläche) [with constant average curvature (minimal area)]". Since then, other authors have also compared plant tissue to soap foam, often suggesting that since the outcome is qualitatively similar, plant cells and soap bubbles may share a common underlying mechanism[5, 6, 7, 8]. In foams, surface tension causes the volume to be maximized while being bound by the least amount of material. Whether plant cells also use mechanical forces to govern locations of new walls has yet to be determined 125 years after Errera's initial observation. Nevertheless, Errera's rule is still used to describe plant cell division patterns. But since this rule does not specify a single, unique location for the new cell wall, more recent authors have added to this that the mother cell divides evenly[9, 10]. With these modifications, Errera's rule is easily quantifiable.

2. Hofmeister observed that new cell walls usually form in a plane normal to the principal axis of cell elongation[11]. This rule is more difficult to quantify because the principal axis of cell elongation is often confused with the direction of growth. Cells are asymmetrical and hence a principal direction of cell elongation can easily be calculated (e.g., the principal axis of inertia or principal component of a segmentation). The assumption is often made that because the cell is more elongated in one direction that the primary growth of the cell has been along that direction, but this is not necessarily the case, as the elongation may be derived from a prior cell division. For example, if a symmetrical square divides into two rectangular cells, this does not mean that the two daughter cells have grown primarily along their longer axis. Quantification of cell growth direction is much more difficult: it requires the observation of matching points over time and varies with the internal and external tensile forces on the cell. It is not clear whether or not the instantaneous direction of cell growth or the longer-term average (e.g., as measured over a significant fraction of a cell generation) is more directly relevant to forming the division plane. Under compression, single cells tend to divide in a plane perpendicular to the long axis of the cell[12] which, similar to Errera's rule, could indicate a mechanical basis for cell wall placement.

3. Sachs observed that new cell walls form in a plane perpendicular to existing cell walls and that the daughter cells are of equal volume[13]. These rules are an accurate description of cells that

have already divided but do not necessarily allow one to predict the plane of division in a cell that has yet to divide since there are often multiple wall positions that fulfil Sachs' rules as illustrated by Minc and Piel[14] in Figure 1.

Other qualitative observations are that cell walls tend to avoid four-way junctions[15] and that cell division planes tend to be staggered, like bricks in a wall[16]. Since chemical signals can be induced by physical interactions such as mechanical stress and strain it is conceivable that these geometric indicators are merely emergent properties of the underlying physico-chemical interaction processes that drives cell division. While most of the geometric observations tend to be true most of the time, none of them are true all of the time, and it is not possible for all of them to be true at once. For example, the actual growth direction is rarely in alignment with the principal geometric axis of the cell and hence the division cannot simultaneously satisfy shortest length and perpendicularity requirements. Such conflicting results can in principle be resolved by minimizing a sum of potential functions[17], and insight into the underlying mechanisms can often be gained by examining the results of the optimization.

### 1.1.2 Mechanism of Cell Plate Positioning

The earliest work to determine the mechanism of division plane formation in plant cells were observations of (what would be later known as) the mitotic spindle and phragmoplast (the scaffold for the cell plate that eventually becomes the wall)[18, 19, 20]. These early observations lead to the discovery of the preprophase band, which is the earliest known indication of the future location of the phragmoplast[21]. The preprophase band is a gathering of microtubules into a circular (not spherical) structure at the periphery of the cell, just inside the plasma membrane. The accumulation of micorubules forms bundle structures[22, 23] that probably also include $\gamma$-tubulin ring complex elements as well as other microtubule binding proteins[24, 25, 26].

Though there is still not much evidence that the preprophase band is directly responsible for positioning the phragmoplast, it has been shown to be necessary for non-random positioning in most Arabidopsis cell types aside from endosperm[27] and meiocites[28]. In tissue culture Arabidopsis cells often lack a preprophase band and exhibit random phragmoplast positioning [29]. Additionally, tissue treated with small molecules that depolymerize microtubules and tissue with genetically inhibited microtubules also exhibit random phragmoplast positioning [30, 31, 32, 33, 34].

So the cell plate, in most cases, is positioned by the organization of the preprophase band. But this changes the question "how is the cell plate positioned?" to "how is the preprophase band positioned?" This is accomplished through a variety of proteins homologous to those in animal centrosome complexes even though plant cells lack centrosomes. For example, the TON1 proteins interact with the preprophase band, the cortical microtubules and the CEN proteins[35]. TON2 mutants display disorganization of the interphase cortical microtubule array and also lack a preprophase band[36]. MOR1, a microtubule binding protein of the MAP25 class, is also required for orderly cortical microtubule arrays and mutants display random phragmoplast orientation[37]. CLASP is typically found along microtubules enriched at the positive end of microtubules[38] and near the plasma membrane and prevents edge-induced microtubule depolymerization, a process that occurs when a microtubule oriented perpendicular to the plasma membrane encounters a sharp cell edge such as those found at a three way junction[39]. Other plant-specific proteins (non-homologous to animal proteins) are involved as well, such as many members of the TRM family which link the TON1 proteins to microtubules[40].

These proteins are all necessary parts of a system guiding the cytoskeleton of Arabidopsis cells but still don't provide a mechanism by which positioning of the preprophase band and phragmoplast are controlled. For a short time CLASP looked like a possible master regulator of preprophase band positioning. It was thought to localize laterally within growing cells and be necessary for the maintenance of the cortical microtubules in such a way that promotes anticlinal (parallel to the apical basal axis) divisions, at least within the meristem. Further, it was suggested that MAP65 expression causes CLASP to relocate within the cell and subsequently causes *periclinal* (perpendicular to the apical basal axis) divisions[41]. This provided a direct link between the transcription of a gene and the positioning of the division plate and provided an obvious mechanism for different cell types to alter their division patterns. But this paper as well as another related paper[42] were retracted because the data were faked so I find it unlikely that this particular connection is true.

While we still don't have a molecular mechanism for the positioning of the cell plate, it is evident that microtubules play a major part in the process. And since there is strong evidence that mechanical forces experienced by cells can influence the position of the cytoskeleton, it is tantalizing to think stress or strain act as regulators of the cell plate positioning process.

### 1.1.3 Stress and Strain as Controlling Factors in Cell Division

If mechanical forces are the significant driver of wall placement this would suggest that (a) the plant cells can somehow detect and respond to mechanical stress/strain, perhaps through some intermediary signalling mechanism, and that (b) the geometric observations are indicators that emerge as a consequence of the physically induced signalling and not the ultimate cause of cell division. None of these observations are sufficient to predict the orientation of the division plane with any confidence; in fact, they are sometimes in conflict, e.g., the current growth direction at any given time results from a complex interaction of mechanical stresses and strains and is not necessarily in alignment with the principal geometric axis of the cell and hence the division cannot simultaneously satisfy shortest length and perpendicularity requirements. Conflicting results can in principle be resolved by minimizing a sum of potential functions[17].

### 1.1.4 Modeling

Additionally, recent work by Besson and Dumais suggests that cell division in plants is inherently random[9]. The new wall tends to find a global minimum length but in situations where there are multiple similar local minima the global minimum is not necessarily chosen.

Previously we looked at cell divisions in the shoot meristem using two dimensional maximum intensity projections[43]. Some of the results from that work may have been biased due to the inconsistent perspective on cells in the peripheral zone compared to the center created by projecting a 3D object into 2D space. Since the meristem is dome-shaped, when projecting the meristem from the top the cells in the center are viewed perpendicularly while the cells towards the edges are viewed at an angle. This non-perpendicular viewing angle distorts the lengths of the cell walls and the angles at which the walls join each other. To rectify that problem the geometry of the cells must be examined in 3D. Here we expand on earlier work with new image processing techniques to analyze the division patterns in 3 dimensions. By using the image processing software MorphoGraphX[44] we were able to reconstruct the cell boundaries in the first layer of a growing SAM [44].

Having a 3-dimensional model of the structure of the L1 layer over time allowed us to generate a model composed of a set of functions, each incorporating a different feature from the observed cell divisions. The functions each contribute a single term to a greater potential function and new walls are predicted to form where the combined potential is reduced. This model also brought to light some of the shortcomings of previously proposed plant cell division rules. Additionaly, these data allowed us to make new observations of the dynamics of cell expansion and division in different regions of the SAM.

## 1.2 Methods

### 1.2.1 Plants

Seeds from the pUBQ::tdTomato-29-1 line in the L-er background were sterilized with 70% ethanol and added to agar plates containing MS and sucrose (30g/L). After a 3-day vernalization at 4°C, seeds were germinated under constant light at room temperature. 10 days after germination, plants were transferred to boxes containing solid growth medium and grown under constant light at room temperature. Plastic boxes 4cm high were prepared under sterile conditions and filled 1cm high with a growth media consisting of MS, MS vitamins, and agar. 1 thin layer of agar without MS was poured on top of the solid MS agar.

### 1.2.2 Time-Series Images

Laser scanning confocal images of four different Arabidopsis meristems were taken at 2 hour intervals during which 207 cell divisions were observed. To image the meristems, the boxes containing the plants were filled with sterile water and placed under the microscope objective. A 63x 0.95NA Achroplan objective was used for imaging. Z-stacks containing 20 optical sections were acquired using a Zeiss LSM 510 with 543nm laser, 543nm dichroic mirror, 560nm longpass filter, 2$\mu$s second scan time per pixel, a resolution of 0.25um(X) by 0.25um(Y) by 1.0um(Z) creating images of 512x512 pixels.

### 1.2.3 Static Images

For comparison geometric statistics were also measured on a collection of 12 additional images of four different meristems at different time points (approximately 200 cells per image). Arabidopsis seeds of the L-er background were germinated on soil under constant light at room temperature. When the shoots bolted, flowers and flower primordia were dissected from the inflorescence. The meristems were cut from the shoot 1cm below the top and inserted into dishes of solid agar. The meristems were stained with 10uM FM4-64 (Invitrogen) at 4°C for 15 minutes. The meristems were then washed with distilled water to remove the excess stain and the dishes were filled with distilled water. The same microscope parameters from the time series imaging were used here.

### 1.2.4 Image Processing

Z-stacks in LSM format were first converted into a TIF series using ImageJ[45] and the LSMToolbox plugin. The functions performed in ImageJ were

1. Import (LSMToolbox plugin)
2. Conversion to 8-bit from 12-bit (Zeiss LSM510 by default captures images in 12-bit)
3. Reverse the image order so the first image is now the last image
4. Save as TIF series

These series of TIF images were then imported into MorphoGraphX. The cell boundaries of the L1 were extracted and segmented using the general methods described previously[44].

Z-stacks in LSM format were first converted into TIF series using ImageJ[45] and the LSMToolbox plugin. These series of TIF images were then imported into MorphoGraphX[44]. The surface of the meristem was extracted using the Closing, Edge_Detect, and Marching_Cubes_Surface functions. The surface mesh was then smoothed and subdivided to around 500,000 vertices. The fluorescent signal from 0 to $3\mu m$ below the surface was projected onto the surface mesh. Segmentation seeds were added by manually clicking in the center of each cell. The surface image was then segmented using the seeds. Cells were created from the segmented boundaries with a minimum of $1\mu m$ between vertices. The full Python code used to automate this method is as follows.

The Python code to generate the 3D mesh was as follows:

```
Stack.Resize_Canvas("Yes","Yes",0,0,20)

Stack.Shift_Stack(0,0,10)

Stack.Average(1,1,1,1)

Stack.Closing(15,15,3)

Stack.Edge_Detect(50000,2,0.3,30000)

Mesh.Marching_Cubes_Surface(5,5000)

Mesh.Smooth_Mesh(1)

Mesh.Subdivide()
```

```
Mesh.Smooth_Mesh(3)

Mesh.Subdivide()

Mesh.Smooth_Mesh(1)

Mesh.Subdivide()

Mesh.Subdivide()

Mesh.Project_Signal("No",1,2,0,50000)
```

Manual seeding of each cell in the image was then performed followed by this Python code

```
Mesh.Segment_Mesh(20000)

count = 0

while count < 2:

    try:

        Mesh.Make_Cells(1)

        break

    except:

        Mesh.Fix_Corners()

        Mesh.Smooth_Mesh(1)

        Mesh.Segment_Mesh(20000)

    count += 1
```

The cells generated by this were exported to a text file for further analysis.

### 1.2.5 Projection to Local Euclidean Plane

A local Euclidean plane was fit to each cell before division, and to the pair of cells after division. The least squares fit to $z = Ax + By + C$ is described by the normal equations:

$$\begin{bmatrix} \sum x_i^2 & \sum x_i y_i & \sum x_i \\ \sum x_i y_i & \sum y_i^2 & \sum y_i \\ \sum x_i & \sum y_i & n \end{bmatrix} \begin{bmatrix} A \\ B \\ C \end{bmatrix} = \begin{bmatrix} \sum x_i z_i \\ \sum y_i z_i \\ \sum z_i \end{bmatrix} \tag{1.1}$$

Each raw data point $(p_i, q_i, r_i)$ was then projected to the local Euclidean by dropping a perpendicular. Let the nearest point in the projection be $(x_i, y_i, z_i)$, where $z_i = Ax_i + By_i + C$; the coordinates

$(x_i, y_i)$ are found by minimizing the square distance function

$$f = (p_i - x_i)^2 + (q_i - y_i)^2 + (r_i - Ax_i - By_i - C)^2 \tag{1.2}$$

which can be reduced to solving the linear system

$$\begin{bmatrix} A^2+1 & AB \\ AB & B^2+1 \end{bmatrix} \begin{bmatrix} x_i \\ y_i \end{bmatrix} = \begin{bmatrix} Ar_i + p_i - AC \\ Br_i + q_i - BC \end{bmatrix} \tag{1.3}$$

Once the point $(x_i, y_i)$ is known, $z_i = Ax_i + By_i + C$. Both the normal equations for the least squares fit and the projection to the plane are solved using the Mathematica function LinearSolve.

### 1.2.6 Alignment of Principal Axes

After translation to the local coordinate system each cell is represented by a matrix of data points

$$X = \begin{bmatrix} x_1 - x_c & y_1 - y_c \\ \vdots & \vdots \\ x_n - x_c & y_n - y_c \end{bmatrix} \tag{1.4}$$

where $x_c$ and $y_c$ are the means of the $x$ and $y$ coordinates. The covariance matrix is calculated using the Mathematica function Covariance as

$$M = \frac{1}{n-1} X^T X \tag{1.5}$$

The eigenvectors of this matrix give the principal directions.

Each cell is rotated into a new coordinate system with $x'$ oriented along the eigenvector first principal component (the one with the larger eigenvalue), $y'$ along the second principal component, and oriented so that $x'y'$ points outward from the meristem. The angle of rotation between the before and after coordinate systems is

$$tan\Theta \frac{x'_A \cdot y'_B}{x'_A \cdot x'_B} \tag{1.6}$$

in terms of the unit vectors $x'_A$,$y'_A$,$x'_B$,$y'_B$ in the after and before Euclidean planes. The after-cells can be aligned with the before-cells by rotating through an angle $\Theta$. Finally, each cell is translated to the center of mass frame[46],

$$x_i = \frac{1}{6}\sum_{j=0}^{n}(x_j + x_{j+1})(x_j y_{j+1} - x_{j+1} y_j) \tag{1.7}$$

$$y_i = \frac{1}{6}\sum_{j=0}^{n}(y_j + y_{j+1})(x_j y_{j+1} - x_{j+1} y_j) \tag{1.8}$$

where the vertices are numbered counter clockwise and vertex 0 is associated with vertex $n$.

## 1.3 Results

A total of 207 cell divisions were observed from four Arabidopsis thaliana L-er pUBQ1::2x-tdTomato-29-1 meristems observed from live imaging using laser scanning confocal microscopy. Since the original segmentation was performed in three dimensions the segmentation points for any given cell do not lie precisely in a plane. To perform subsequent analysis, a best fit local Euclidean plane (see Supplemental Information “Projection to Local Euclidean Plane”) was found using the method of least squares, and each point was then projected to the local Euclidean plane by dropping the local perpendicular to the plane. The mean offset was 0.07±0.05±6.2$\mu$m$^2$ (Figure 1.1a). The mean area of the cells before division was 40.0±6.2$\mu$m$^2$ (mean ± standard deviation). The mean area of the daughter cells was 21.0±5.5±6.2$\mu$m$^2$. Mean cell perimeter before division was 24.9±2.1±6.2$\mu$m, and of the daughter cells was 18.2±2.4$\mu$m (Figure 1.1b). The distribution of areas was more symmetric for the parent cell than the daughter cells (skewness of 0.22 vs 0.71). For comparison a study of 4 meristems showed cells areas with mean, sd, skewness. This more closely resembles the skewness in the areas as distributed across the entire SAM (Figure 1.1c) in which the average area was 22.6±6.5$\mu$m$^2$.

### 1.3.1 Cell Expansion and Division in Space and Time

It is known that cells must expand and divide to maintain the amount of tissue in the SAM as groups of cells are incorporated into flower primordia around the periphery and exit the SAM. To quantify this phenomenon we measured the expansion of each cell over each two hour period. The cell expansion occurs in waves as can be seen in Figure 1.2a. This wave phenomenon is also observed in the quantity of divisions over time. Over the observed 38 hours the average expansion rate and

Figure 1.1: (a) Distribution of mean error (mean of the absolute value of perpendicular distance) in fit to local Euclidean. (b) Distribution of parent cell areas before division (white, dashed) and child cell areas after division (gray, solid). (c) Distribution of areas globally across the SAM L1 layer (excluding floral meristems) (4 meristems, 200±26 cells per meristem) and one-sigma errors.

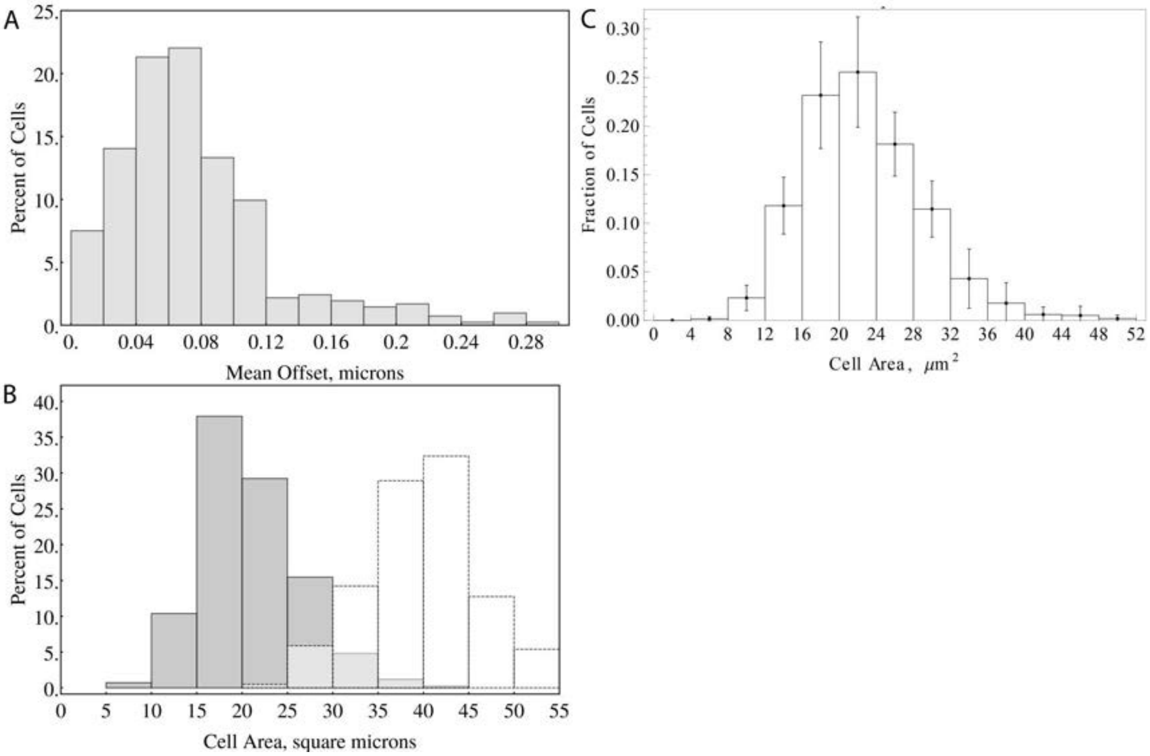

quantity of divisions gradually decreases possibly due to the exposure to laser light, dissection of surrounding flowers, or the repeated submersion in water, all of which effect the health of the plant. It should be noted that while the waves of expansion and division are approximately in phase with each other, the cells that are dividing are not necessarily the same cells that expand the most during any 2 hours.

As shown in Figure 1.2b, cells in the center of the meristem expand very little and in some cases shrink between time points. This phenomenon is observed at all time points and does not fluctuate with the waves of expansion observed elsewhere in the meristem.

To quantify the relation of expansion and division we measured the expansion ratio of cells that divided and cells that did not divide separately, the results of which are shown in the Figure 1.2c. The mean expansion ratio of the 207 dividing cells barely different from that of the nondividing cells: the variance of both populations is too large to differentiate statistically. This suggests that expansion and division are not directly coupled, at least in the two hours prior to division. Given that the cells are all of similar sizes, expansion over the entire cell cycle must be correlated with division.

While rapidly expanding cells have no correlation to dividing cells, there is a bias in the spatial location of the rapidly dividing cells. As seen in the Figure 1.2b, cells towards the top of the meristem are dividing more slowly than those toward the bottom, but there is no clear boundary between rapidly and slowly expanding regions. This phenomenon was observed at all time points.

### 1.3.2 Analysis of Traditional Heuristics of Cell Division

Many rules about cell division have been reported and widely quoted. Care must be taken in applying these rules as they are all only valid in an approximate sense (as will be shown below) and are often in conflict with one another. Since they are only generally (but not absolutely) valid and are only applicable in the proper context, we refer to them as the heuristics (rather than laws or rules) as they are experience-based guidelines that will often, but not always, work. In addition to the three heuristics that we address below, we also analyzed Hoffmeister's Rule, new walls forming perpendicular to existing walls, and growth immediately after division in the supplementary text (see section “More Heuristics”).

Figure 1.2: (a) Solid line indicates the quantity of cells dividing within a given period. Dotted line indicates the mean ratio of cell expansion within a 2 hour period. (b) Heat map on the left shows the amount of cell expansion between the time points at 2 and 4 hours as a ratio. Stars indicate cells that divided during this time period. (c) Histogram on the right shows the mean expansion of cells that divided during any 2h period compared to cells that did not divided.

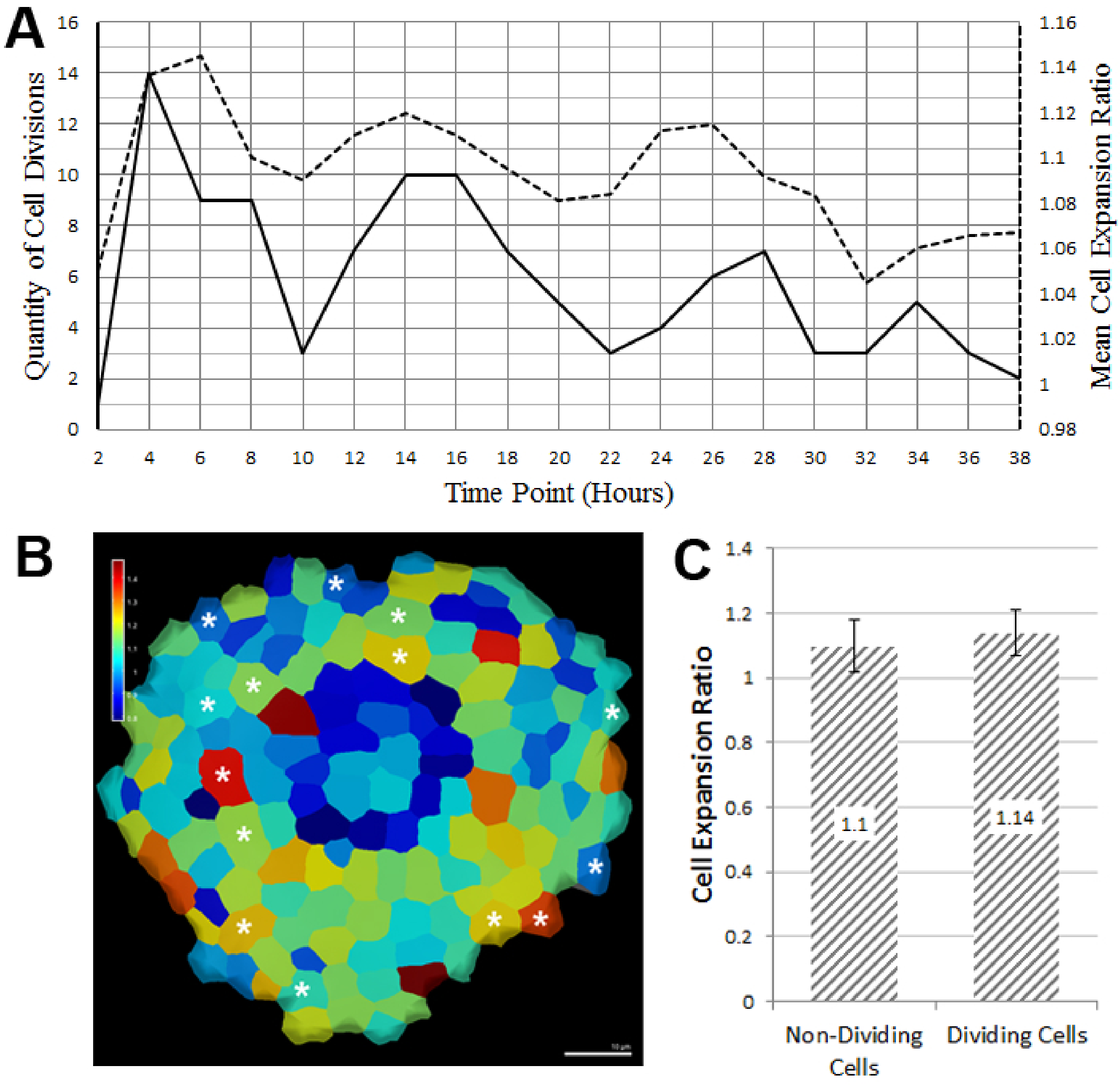

**Heuristic 1: The new wall is a minimal surface that divides the mother cell equally**

Errera's rule (1888) states that the cell divides along a surface that minimizes the area of the new wall[4]. Errera did not specify the position of the new cell wall (the intersection of the new wall with the cortex). If the wall position is not specified, its minimum area could approach zero in cells of many shapes (conical or spherical for example). To make a predictive model we add as do other modern authors[9, 47, 48, 49] that the division halves the volume of the mother cell. We thus are not testing Errera's actual rule; rather, we are testing the heuristic that modern authors call Errera's rule. For cells in the L1 layer, with uniform depth and anticlinal divisions, we can make a two-dimensional equivalent of this heuristic in which the cell divides along a curve that minimizes the length of the new wall, and that halves the mother cell.

The cells in the 207 cell division sibling pairs ranged from 24 percent to 76 percent of the total area, with a standard deviation of 9.3% within the full range (0.0 to 1.0), as illustrated in Figure 1.3a, which shows the ratio $r = A_i/(A_1 + A_2)$, where $A_i$ is the projected area of the cell in the tangent plane

The divisions that fit this heuristic the worst (bottom 20 percentile) were not evenly distributed throughout the meristem. As it can be seen in Figure 1.3b, in one of the meristems we investigated many of the divisions most poorly predicted occur in the periphery of the meristem. In fact, 72% of the divisions in the bottom 20 percentile occur within three cells of the edge of the meristem. If these uneven divisions are occurring in regions that eventually become primordia, the unevenness of the division might be due to the previously reported phenomenon of a change in the polarity of divisions within founder cells in vegetative meristems [50, 51].

**Heuristic 2: The new cell wall passes through the center of the cell**

The shortest distance from the new cell wall to the centroid of the cell was determined by (a) fitting a least-squares quadratic to the new cell wall, and (b) finding the minimum distance between the quadratic and the centroid of the combined pair of cells immediately after cell division. The quadratic fit was used to smooth the segmentation which would otherwise be composed of a joined sequence of line segments (Figure 1.4a). To obtain a size-independent (dimensionless) measure, the distance was measured in units of $P/2\pi$, where P is cell perimeter, which would correspond to an effective radius for a spherical cell (illustrated on the right side of figure 5). Some 30%, 50%, and 88% of the cell walls passed within 0.05, 0.1 , and 0.2 effective radii, respectively (Figure 1.5a).

Figure 1.3: (a) Distribution of daughter cells as a fraction of the total area. The total area is defined as the sum of the areas of the two siblings. (b) Division of area of mother cell. (c) How well each division matches the modern interpretation of Errera's rule ranked by percentile and grouped into 10 bins indicated by colors.

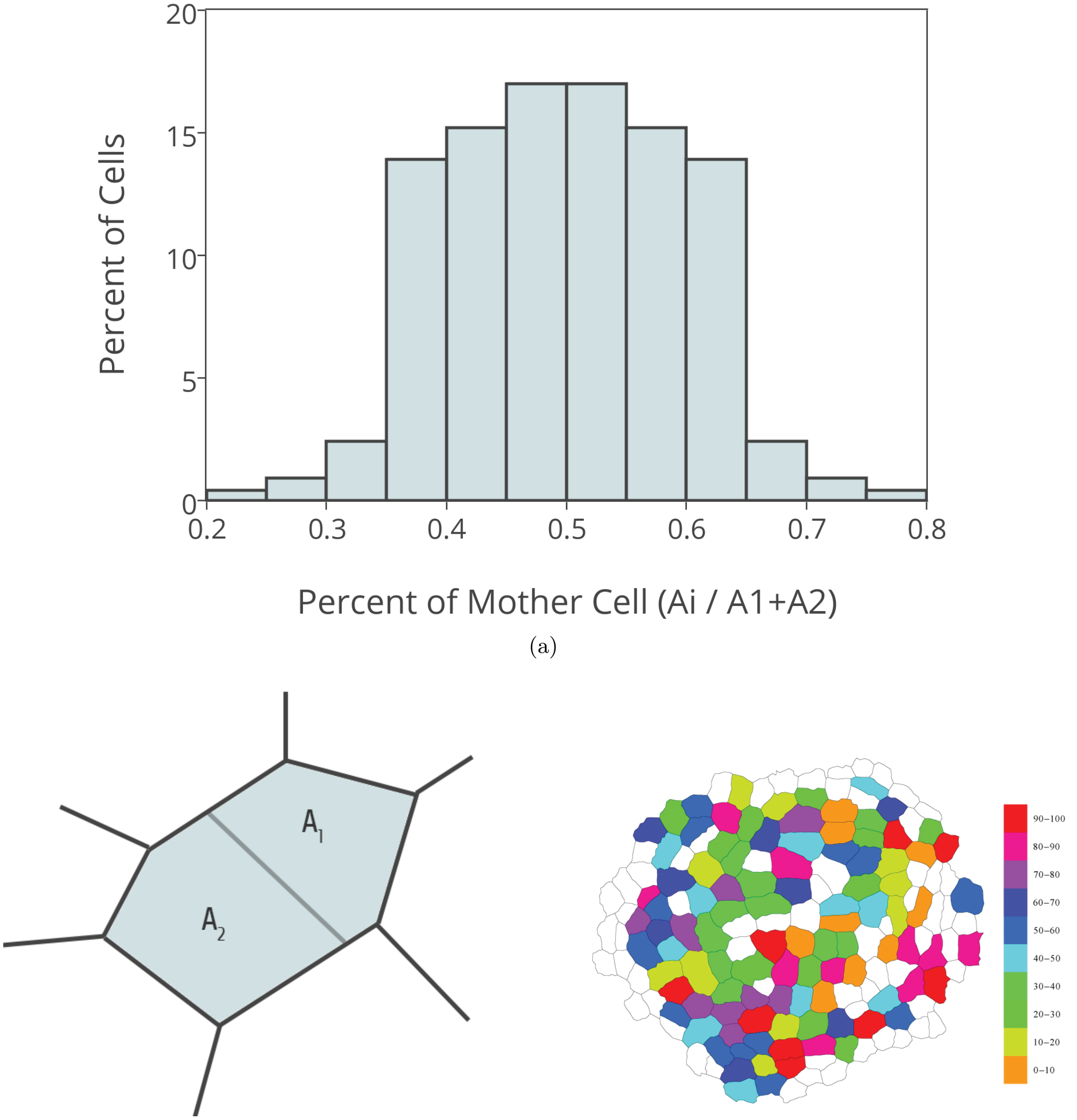

(a)

(b)

(c)

Figure 1.4: (a) Left: Definition of shortest distance of new cell wall from centroid, for a typical cell. Right: Illustration of the units for values of r=0.05 ,0.1, 0.2, 0.3, and 0.4 for a circular cell. The dashed circles would correspond to a typical cell nucleus that is just skirted by the tangential curved new cell wall. (b) Closest approach of new cell wall to centroid, relative to $r = P/2\pi$, where $P$ is the cell perimeter. Left: distribution; Right: cumulative distribution.

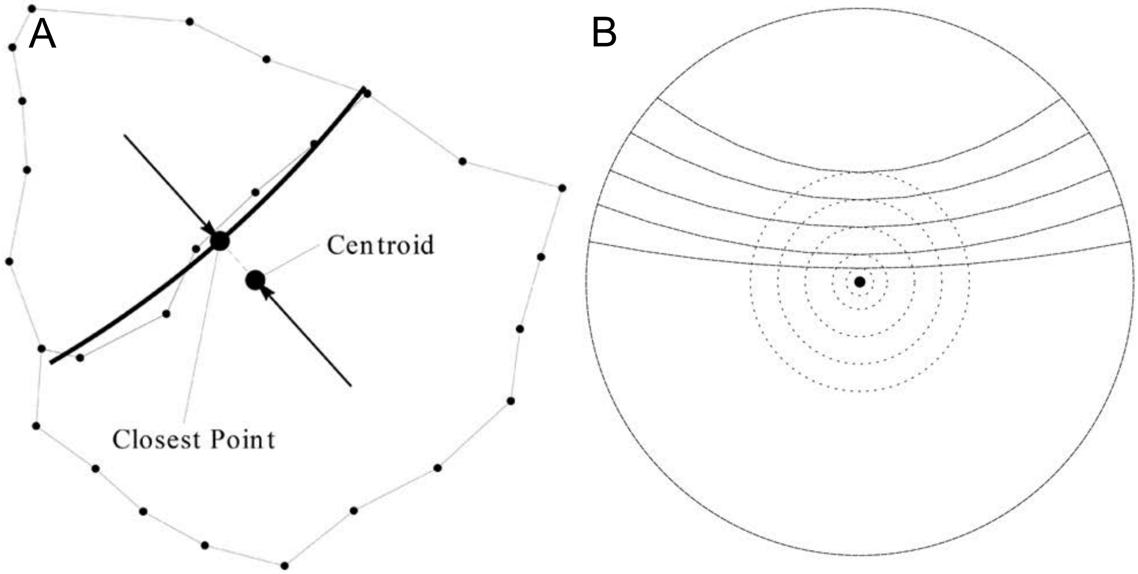

A second measure of how nearly the new cell wall passes through the center of the cell is to measure the angle $\Delta\Theta$ subtended between vectors from the center to the endpoints of the new wall (Fig. 4). In this measure, a straight line wall that passes through the centroid would subtend an angle of 180 degrees. With one exception (at $\Delta\Theta = 88deg$) virtually every cell division subtended an angle of more than 100 deg. As illustrated in Figure 1.5b, 130 deg is exceeded over 90% of the time, 140 deg is exceeded over 80% of the time, 150 deg is exceeded two thirds of the time, and over half the cell division had a central angle exceeding 160 deg, or within 20 degrees of the maximum 180 degrees to make a stright line.

### Heuristic 3: The plane of cell division is the shortest path (Soap Bubble Dynamics)

The modern interpretation of Errera's rule (translated to the tangent plane of the L1 layer) suggests that a new cell wall should form along the shortest path that divides the cell evenly. This prediction cannot completely dissociate into two independent heuristics of length minimization and area equalization, in that it minimizes wall length subject to the constraint that the wall divides the cell evenly. However, to assess the significance of a wall shortness constraint we compared

Figure 1.5: (a) Closest approach of new cell wall to centroid relative to $r = P/2\pi$, where $P$ is the cell perimeter. (b) Distribution of new cell wall central angles.

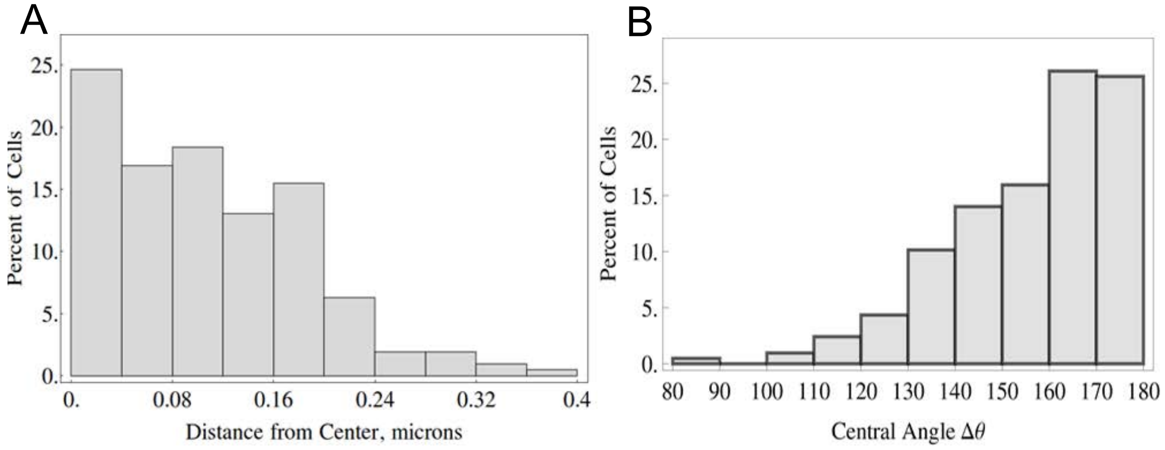

the actual wall lengths to the minimum and maximum diameters of each cell with the statistic $d_{rel} = (d - d_{min})/(d_{max} - d_{min})$. A cell diameter is defined as the length of a line segment passing through the centroid from one cell wall to the opposite cell well. As this line segment is rotated about the centroid its length will change. We call its maximum and minimum values the maximum and minimum diameters. When $d_{rel} = 0$, the wall has the same length as the minimum diameter; when $d_{rel} = 1$, the wall has the same length as the maximum diameter (Figure 1.6). A value of $d_{rel} < 0$ indicates that the actual wall length is shorter than the minimum diameter, because the actual wall does not pass directly through the center but is skewed somewhat. The wall length was defined as the length of the quadratic fit to the new wall (so as to eliminate noise from the image segmentation, see Figure 1.4), and the diameters were defined as the lengths of line segments through the centroid that spanned the entire cell. We found that in 49% of the cell divisions the relative wall length fell within 10% ($|d_{rel}| < 0.1$) of the minimum diameter, and that in 69% of the cell divisions it was within 20% of the minimum diameter. The longest wall had $d_{rel} = 0.67$. More notably, in 76% of the cases, the actual wall length was shorter than the minimum diameter (Figure 1.7).

### Heuristic 4: The cell divides perpendicular to the main axis of growth (Hofmeister's Rule)

The difficulty with applying this rule is that it is difficult to calculate the main axis of growth without a fine time-resolution set of live images. Hofmeister (1863) emphasized that the axis of growth is not necessarily the longest diameter of the cell. The instantaneous direction of growth can be defined

Figure 1.6: Definition of cell coordinates in local frame (left) and various parameters used in the definitions of fitness measure (right). The reference axes for definition of angles are the principal components of the segmentation.

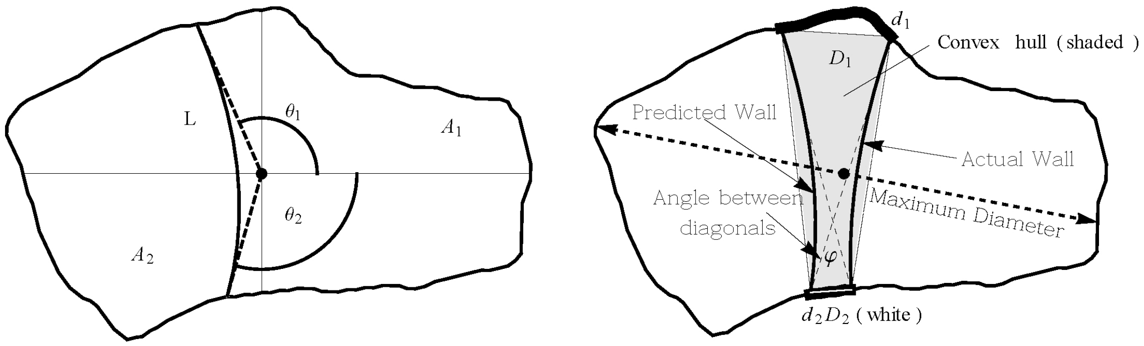

mathematically as the principal axis of the velocities of the vertices (corresponding to the eigenvector with largest eigenvalue of the covariance matrix of the velocities of the vertices)[52]. Alternatively, one might conjecture that since more material will accumulate in the principal direction of growth, that the cell will be extended primarily along that direction. This would imply that the principal axis of the cell (corresponding to the eigenvector with the largest eigenvalue of the covariance matrix of the vertices of the cell, or of the segmentation points, or the principal axis of inertia) should be used to define this main axis of growth. It is challenging to measure the instantaneous direction (despite the algorithm given by [52]) because (1) matching vertices at two different time points assumes that the material at the vertex at one time point should be matched to the vertex at the succeeding time point, and (2) we have observed that cells often shrink (see cell growth heuristic, below) during the time around cell division so it is difficult to assign a meaning to the growth direction in these cells. Because the change in area over the few hours around cell division is very small, and sometimes negative, small errors in segmentation can lead to significant differences in determination of the velocity axis.

Hofmeister's rule (using cell elongation for principal axis) is supported by a change in the distribution of the isoperimetric ratios before and and after cell division. This ratio is $i = 4\pi A^2/P^2$, where $A$ is the area and $P$ is the cell perimeter. It gives a size-independent measure of the elongation of a polygon. A value of $i = 1$ indicates that the cell is nearly circularly shaped; all other closed curves will have a value of less than 1. The further away from 1, the more elongated the cell is. The inequality $4\pi A \leq P^2$ has been attributed to the ancient Greek geometer Zenodorus, in the sense that a circle has greater area than any other regular polygon of equal perimeter. Using the Calculus of Variations it was proven for any closed curve by Jakob Steiner 1836[53]. The typical distribution of

Figure 1.7: Distribution of new wall length. New wall length is expressed as a ratio of the difference between the observed wall length and the minimal wall length to the difference between the maximum wall length and the minimum wall length.

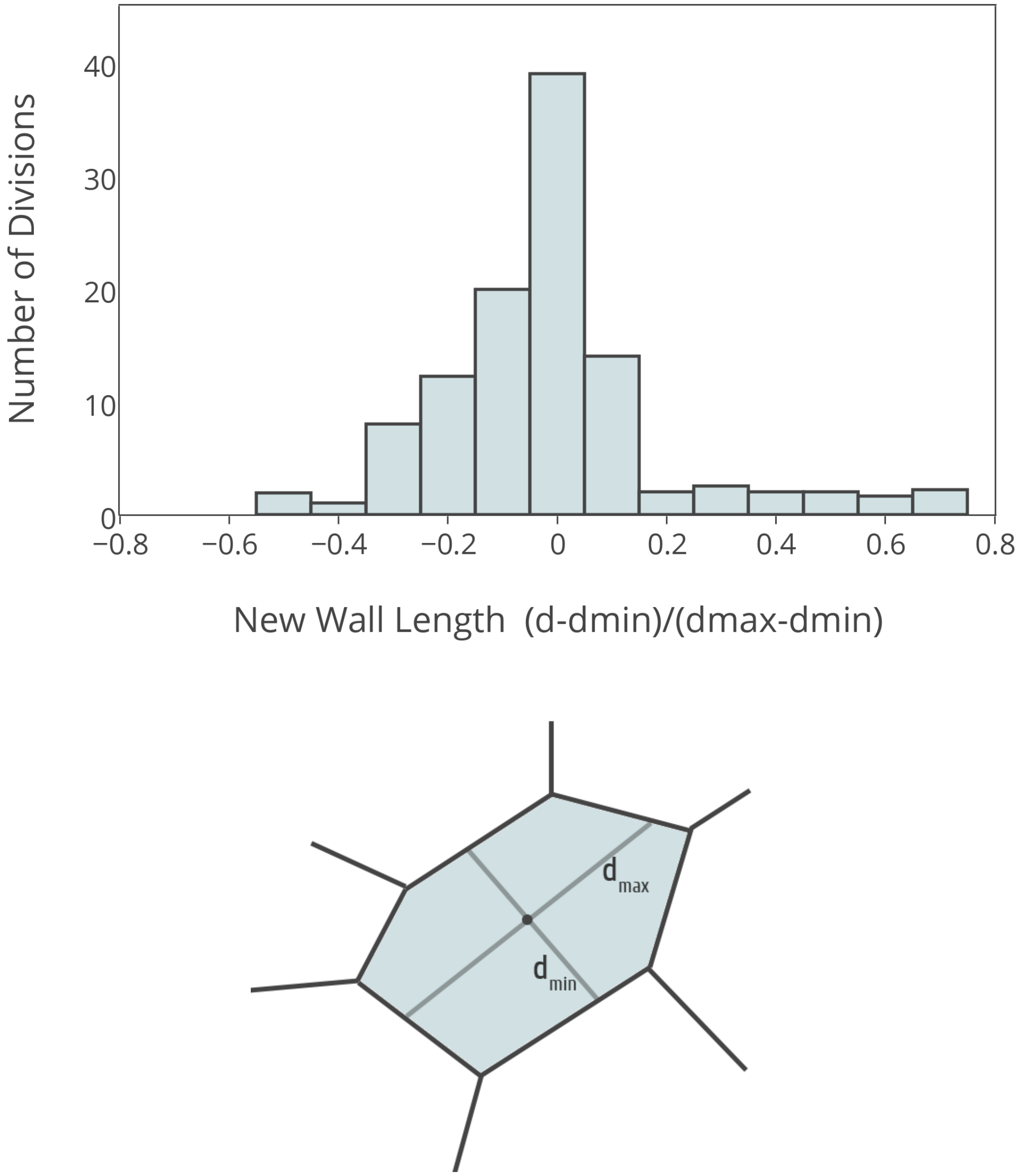

isoperimetric ratio in the L1 layer is illustrated in Figure 1.8a. In Figures 1.8b and 1.8c we compare the isoperimetric ratios before and after cell division. Statistically there is very little difference in the average value of isoperimetric ratio before and after cell division, but the distribution is tighter after division ($i = 0.78 \pm 0.07$) (identical to the global surface average) than before ($i = 0.76 \pm 0.10$). Furthermore, the skewness of the distribution as evident in the overall data is reproduced by the cells after division, but is not as evident in the cells before division. In other words, cells that are about to divide are shaped differently than typical cells. However, this difference does not indicate any particular body shape as the data spread is fairly wide.

The angle between the new cell wall and the principal cell axis is heavily weighted towards perpendicularity (90 degrees), with a differentiation from perpendicular of less than 10 degrees in 30% of the data, less than 20 degrees in 55% of the data, and less than 30 degrees in 75% of the data. This supports the notion that cell elongation should be used to determine new cell wall direction. The actual distribution of these angles is shown in Figure 1.9a. The principal axis is determined as the eigenvector, corresponding to the largest eigenvalue, of the covariance matrix of the projection of the segmentation to the least-squares local Euclidean plane. The direction of the cell wall is found from a least-squares parabolic fit to the new cell wall, as illustrated in Figure 1.9e.

#### Heuristic 5: The new cell wall forms in a plane that is perpendicular to existing cell walls

To quantify how often the new cell wall forms in a plane perpendicular to existing cell walls the angle between the new cell wall and the existing wall was measured (Figure 1.10). Because the segmentation is pinched in around the intersection, a short arc of the segmentation (up to around 30 degrees central angle in either direction) was fit with a parabola, and the intersection between that parabola and a similar quadratic least squares fit to the new cell wall was used to determine the angle of intersection. The measure used was the smaller of the two interior angles formed by the intersection of the two tangent lines. Some 25% of the intersections were within 5 deg of perpendicular 52% within 10 deg of perpendicular, and 84% within 20 deg of perpendicular when measured in this manner. This is consistent with Sachs' observation, as an emergent property in a statistical sense.

Figure 1.8: (a) Distribution of isoperimetric ratio over 12 timepoints from four different meristems having 200±28 cells in each meristem. (b,c) Distribution of isoperimetric ratios over 207 cell division events for the parents in the last observation before cell division (b) and the first observation after cell division (c). (d) Distribution of angle between new cell wall and normal to principal axis of cell extension (e) Projection of typical segmentation to local Euclidean. The arrow shows the direction of the new cell wall.

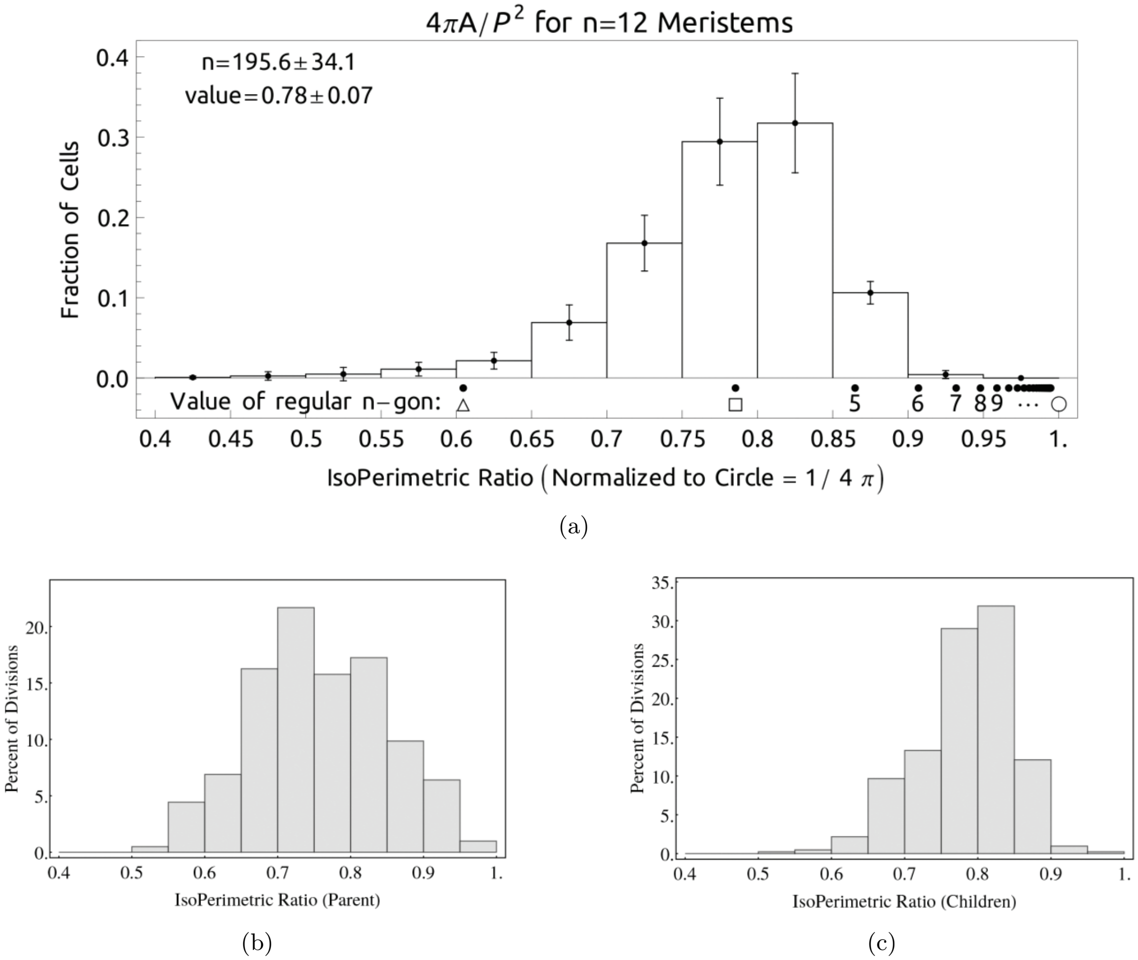

(a)

(b)

(c)

Figure 1.9: (a) Distribution of angle $\theta$ between new cell wall and normal to principal axis of cell elongation. (b) Long arrow indicates primary direction of elongation. Theta is the angle of this direction with respect to the new wall. (c) Least squares fit to vertices.

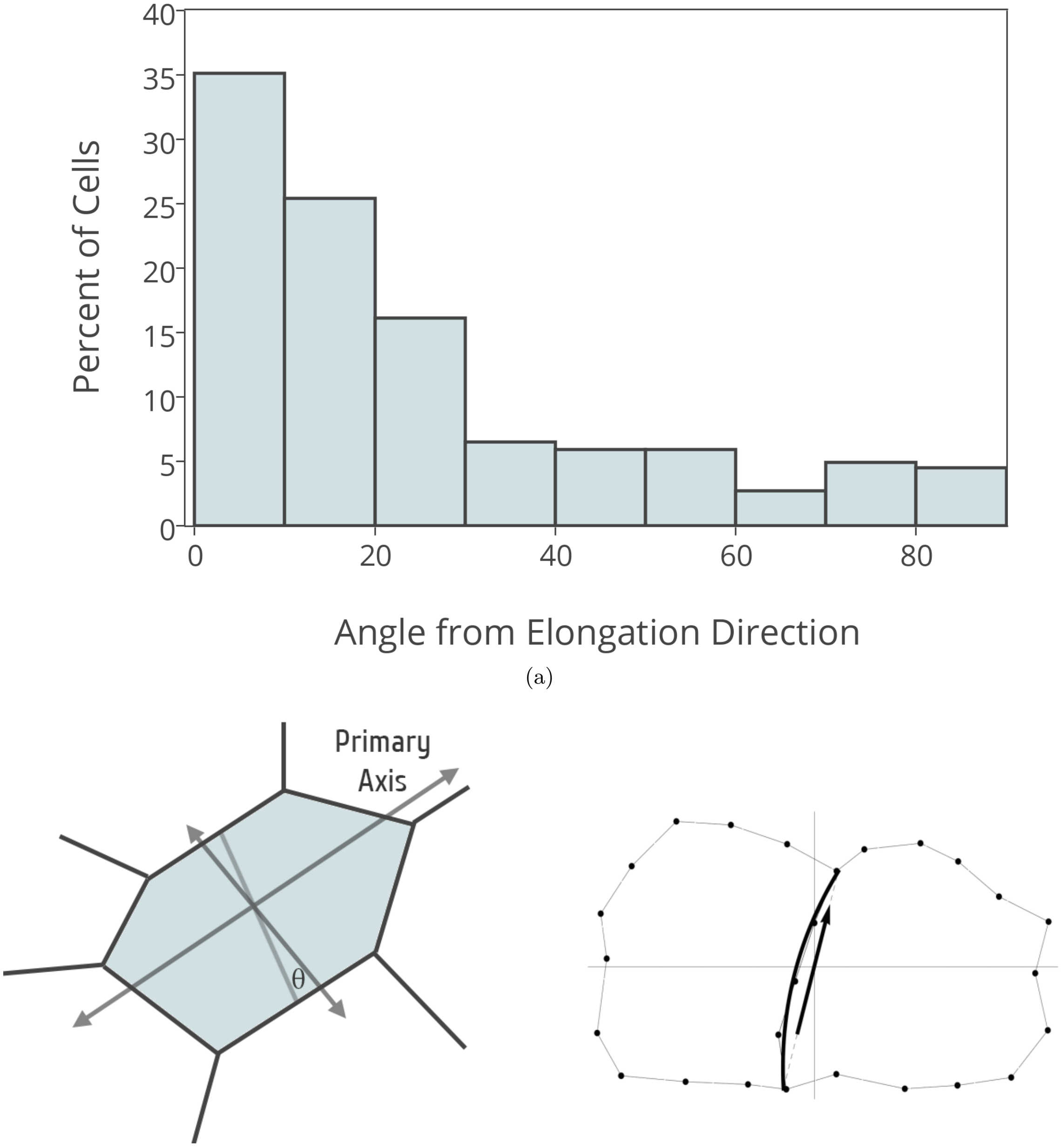

(a)

(b)

(c)

Figure 1.10: The angle between existing cell wall and new cell wall, degrees. (a) Least-squares quadratics used to calculate angles so as to reduce noise from the segmentation – see dotted line), for a typical cell. (b) Distribution of angle between new wall and existing wall for all cell divisions.

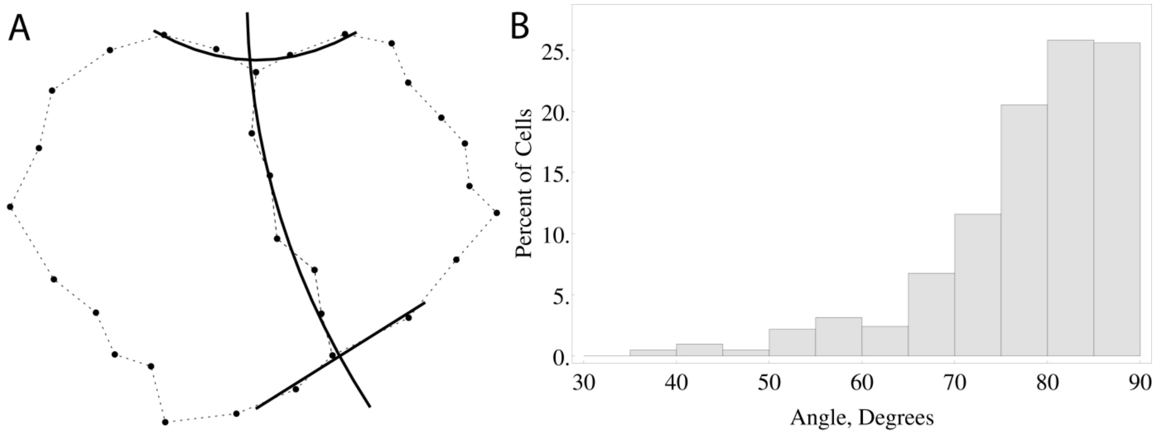

**Heuristic 6: The cell continues to grow immediately after cell division**

In only 65% of the 207 cell divisions was the area, as measured in the first time point after cell division, greater than the area as measured at the last time point before cell division. The ratio of the area after cell division ($A_{after} = A_1 + A_2$, where $A_1$ and $A_2$ are the areas of the sibling pair) to the area before cell division ($A_{before}$) is illustrated in Figure 1.11. While this may be partially due to an artifact of the image segmentation algorithm (which may favor "pinching" in the corners near the new wall), it may also indicate that perhaps the additional tension added by the new wall may inhibit additional growth for a short period of time after cell division. The various heuristics fall into two categories: those that determine the cell wall completely, and those that put constraints on the optimization process, but do not fully determine wall position on their own.

### 1.3.3 Model

Four potential functions $V_i$ were defined (see equations (4.5), (1.10), (1.11), (1.12), and (1.13)). For any given weight vector $w = (w_1, w_2, w_3, w_4)$ the cell division potential function $V(\Theta_1, \Theta_2) = \sum_{A,L,g} w_i V_i(\Theta_1, \Theta_2)$ will describe a landscape in $(\Theta_1, \Theta_2)$ space such that the lowest point of this landscape corresponds to the predicted wall location, with $\Theta_1$ and $\Theta_2$ given the central angles of the two end points of the wall as measured from the cell centroid. When plotted as a function of $(\Theta_1, \Theta_2)$, this landscape is symmetric about the 45 degree line $\Theta_1 = \Theta_2$ and hence only points above (or below) the line need be considered, as the data are duplicated in both parts of the plot. This landscape may be represented by a contour plot, analogous to a topographic map (see Figure 1.13).

Figure 1.11: Distribution of areas after as compared to before cell division. The ratio of the area after cell division to the area before cell division is shown.

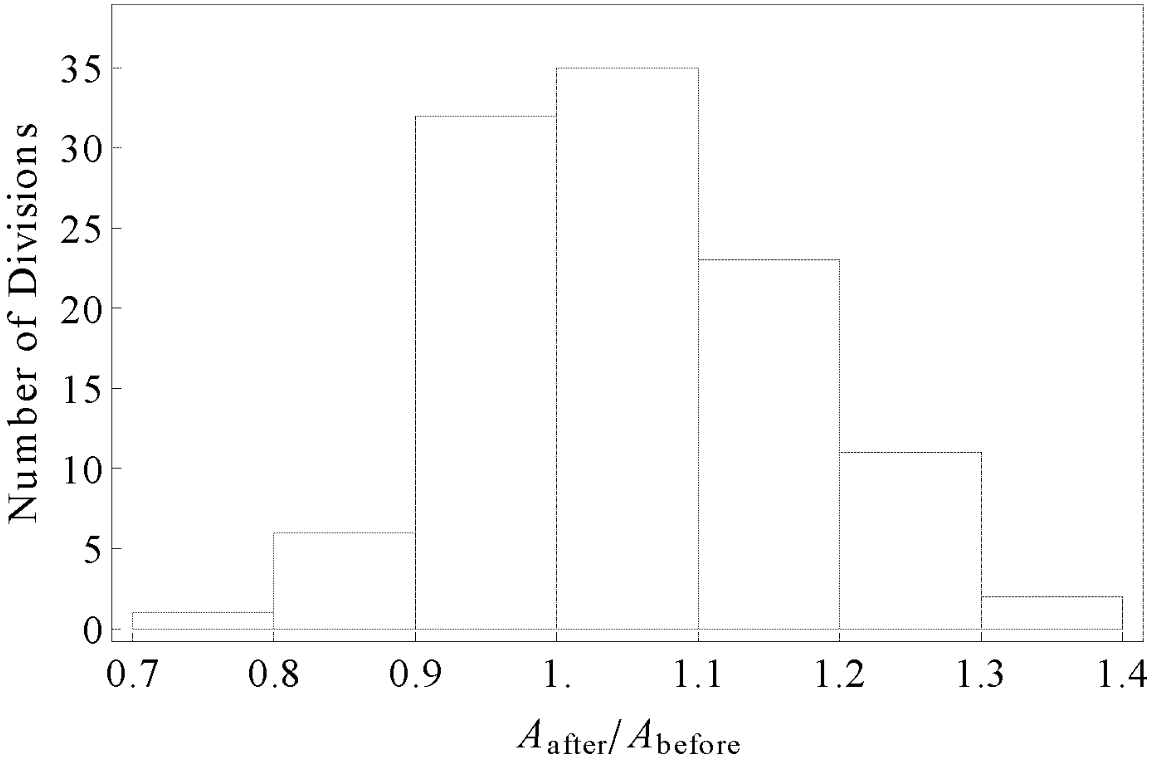

The object of the optimization process is then to find a weight vector that works best in as many cells as possible. Thus the potential is minimized for each cell and each possible weight vector; for each $w$, the prediction errors are calculated (as a fitness function) for each cell and combined to produce a net fitness for that weight vector.

The cell division model defines a potential function[43, 54]

$$V(\Theta_1, \Theta_2) = \sum_{A,L,e,g} w_i V_i(\Theta_1, \Theta_2) \tag{1.9}$$

where $\Theta_1$ and $\Theta_2$ give the central angles of the end points of the new wall measured from the cell center of mass (Figure 1.6), $w$ is a weight vector, and $V_i$ represents each contributor to cell division.

Four components were include in the sum (4.5): an area potential, a length potential, a perpendicularity potential, and a growth direction potential.

Figure 1.12: (a) Angles $\theta$ of new wall from growth direction in 15 degree bins. (b) Relationship between growth axis and plane of cell division, measured by angle $\theta$. (c) $\theta$ from all 207 cell divisions.

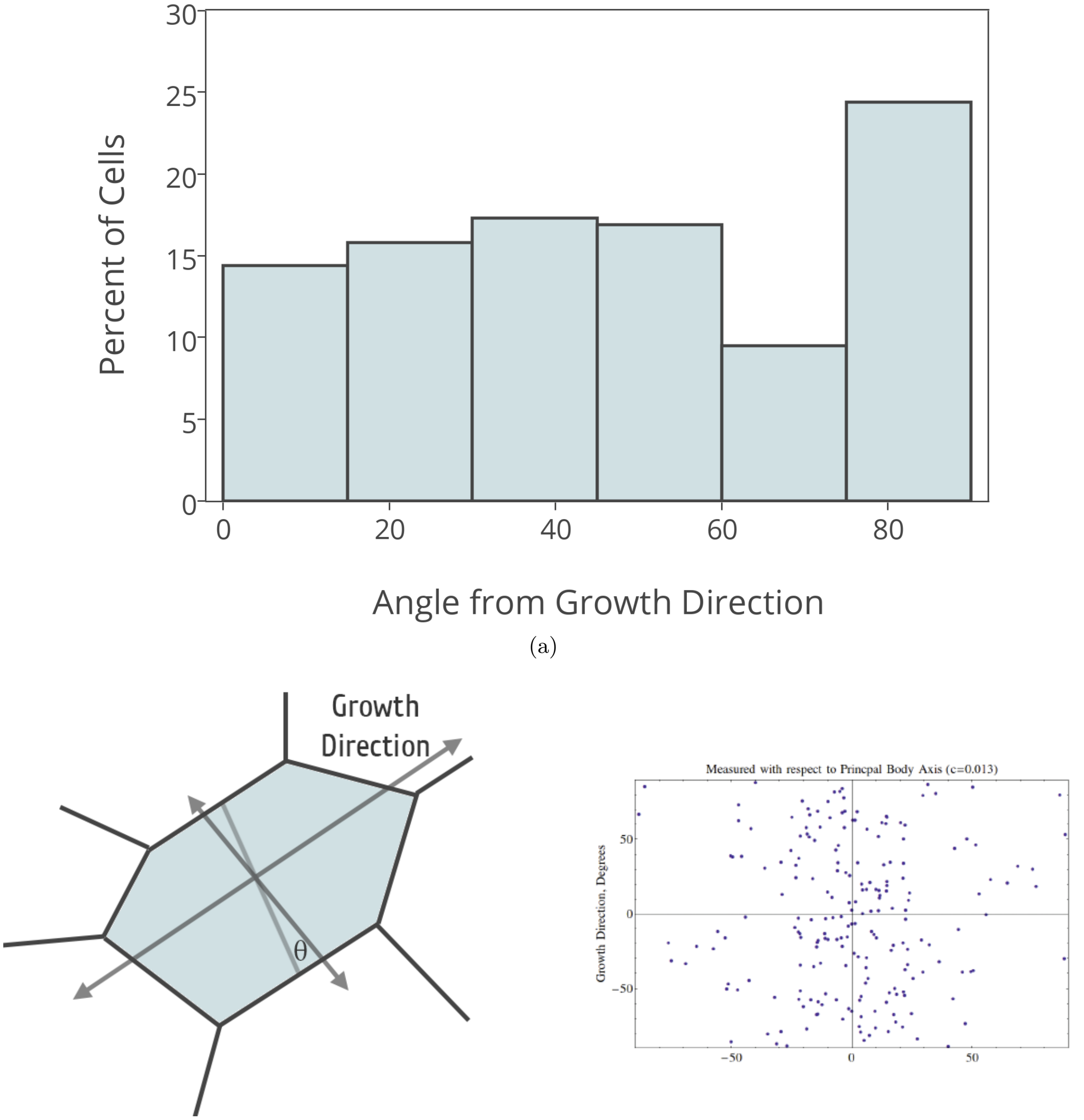

(a)

(b)

(c)

Figure 1.13: Example of potential function landscape, shown for cell 25 using a weight vector $w = (1, 1, 0, 0)$. Darker regions correspond to higher altitudes and light regions to valleys. The global minimum is show with an open circle and the actual wall endpoints by a dot. The two axes give the angle of $\Theta_1$ and $\Theta_2$ in degrees, and the inset shows an outline of the actual and predicted cell walls.

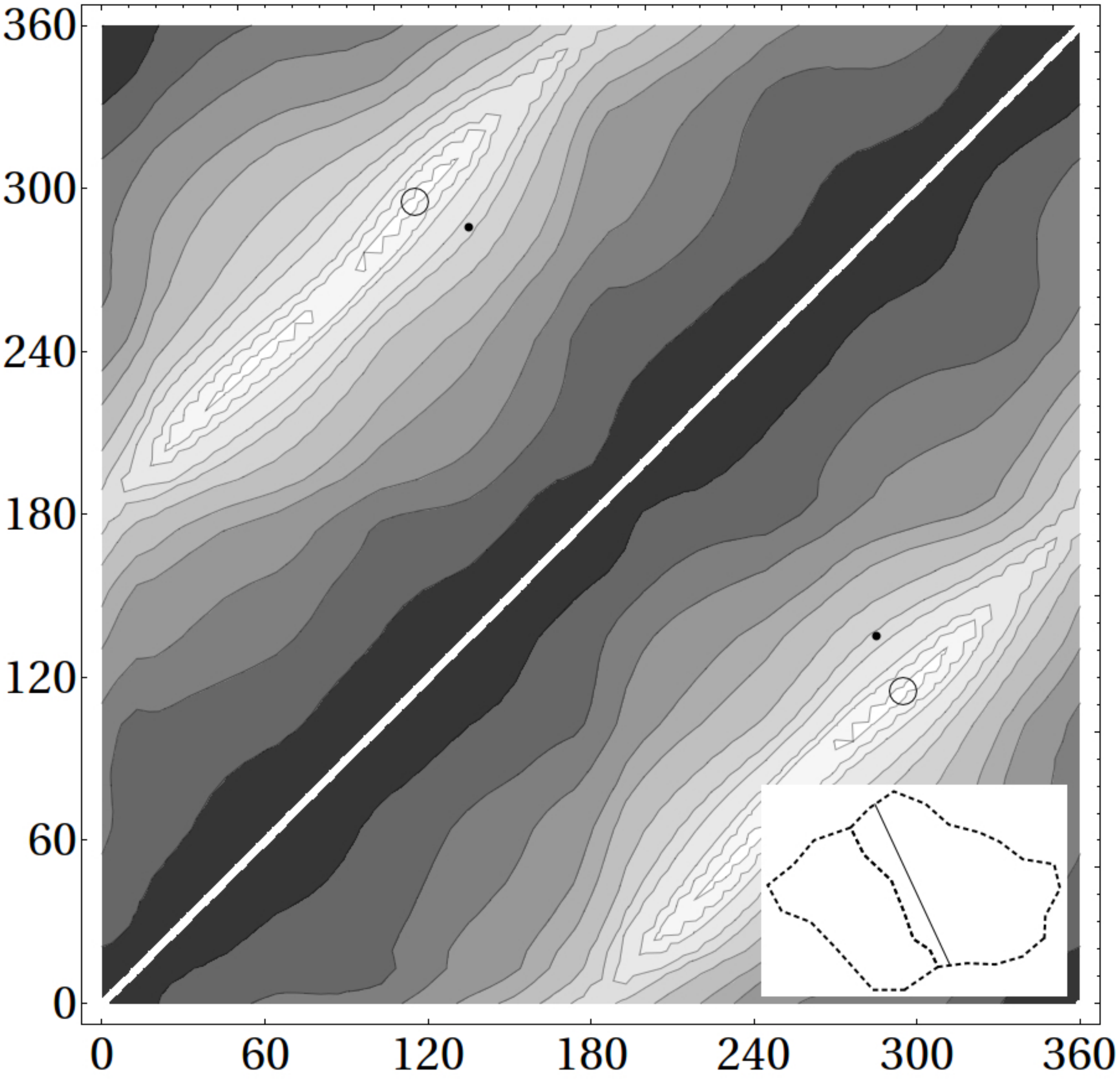

1. The area potential $V_A$ is minimized when the two daughter cells are equal in area:

   $$V_A = \left(\frac{A_1 - A_2}{A}\right)^2 \tag{1.10}$$

   The function is squared to improve computational stability near the minimum (which would otherwise have a non-differentiable corner there). The disadvantage of this potential is that it does not have a unique global minimum, i.e., any line of cell division will that divides the area in half will give a value of zero. Thus the area potential must be tempered by either an additional potential function (such as the perpendicularity and/or length potential) or an additional heuristic to select the desired minimum value that does not require a unique minimum (e.g, randomly select division direction from amongst all equivalent minima).

2. The length potential $V_L$ is:

   $$V_L = \frac{(d - d_{min})^2 + c_L\Delta^2}{(d + d_{min})^2} \tag{1.11}$$

   where $d$ is the actual wall length and $d_{min}$ is the minimum length diameter. Thus $V_L$ will be minimized when the cell wall is most closely aligned with the shortest possible diameter.

3. The extension potential $V_e$ is minimized when the new wall is perpendicular to the direction of maximal cell extensionsion potential $V_e$ is minimized when the new wall is perpendicular the direction of maximal cell extension $e$:

   $$V_e = (w \cdot e)^2 + \frac{\varepsilon_g \Delta}{d} \tag{1.12}$$

4. The growth direction parameter $V_g$ is minimized when the new wall is perpendicular to the vector of maximal cell growth $g$:

   $$V_g = (w \cdot g)^2 + \frac{\varepsilon_g \Delta}{d} \tag{1.13}$$

   Maximal cell growth direction is calculated using the method described in [52].

The parameter $\Delta$ in (1.11), (1.12) and (1.13) gives the shortest distance between the wall and the cell center, with weighting factors $\varepsilon_e$ and $\varepsilon_g$. In (1.12) $d$ is the actual wall length. The purpose of the $\Delta$ term is to help distinguish between different walls of the same length (for $V_L$) or direction (for $V_g$): one that passes closer to the center is more likely than of the same length (or direction) that skirts the edge of the cell; such "skirting" walls would otherwise be predicted by $V_L$ or $V_g$, especially in more oblong cells.

The cell division potential was minimized and the fitness function calculated for each of the six methods described in the sup. An average value (corresponding to the fitness function averaged over all 207 cell divisions) was assigned to each value of the weight vectors. Since only the direction of the weight vector, and not its actual length, is important in finding the minimum value, the four component weight vector $w = (w_1, w_2, w_3, w_4)$ can be represented by a unit vector in the same direction; e.g., the weight vector $(1, 1, 0, 0)$ is completely equivalent to a weight vector $(\sqrt{2}, \sqrt{2}, 0, 0)$. The four dimensional weights were found by taking three dimensional slices along two planes, holding parameter three fixed and holding parameter four fixed. With this constraint, each three component weight vectors in a slice can be described by two angles $(\alpha, \delta)$, giving the azimuth and elevation in $w$ space, where $w_x = cos\delta cos\alpha$, $w_y = cos\delta sin\alpha$, and $w_z = sin\delta$. A global search of weight vector space was then performed at approximately 3 degree increments (620 values) to obtain a coarse description of the fitness. A spatial resolution of 3 degrees was also used. For computational efficiency only cell walls with a minimum central angle of 90 degrees were considered during the optimization (as suggested by Figure 1.4). Predictions were made using the pre-division observations (“before" data) obtained at the start of a two hour window during which cell division took place, and evaluated in comparison to the observed location of the cell wall as determined from post-division observations (“after" data) obtained at the end of the same window. For comparison, a second set of predictions were calculated using only the "after" data (“hindsight” predictions). In the hindsight predictions the outer boundary of the pair of daughter cells was used to represent the pre-division cell wall.

### 1.3.4 Fitness Functions

We asked the question whether any weight vector $w$ could be found such that $V(\Theta_1, \Theta_2)$ is minimized when the predicted angle pair matches the actual cell division plane. To determine the weights we performed a coarse global search on the first quadrant of the global hyper-sphere $|w| = 1$. For each $w$ value, the location of the minimum potential in $(\Theta_1, \Theta_2)$-space was determined and subjected to a fitness measure. For any given cell $i$, the following fitness measures were considered:

1. Error in distance between endpoints of actual and predicted wall, as measured along the circumferential path of the boundary, measured relative to the maximal cell diameter:

$$f_{i,boundary} = \sum_{j=1}^{n} \frac{d_1 + d_2}{d} \tag{1.14}$$

2. Actual distance between endpoints of actual and predicted cell wall, relative to maximal cell diameter:
$$f_{i,boundary} = \sum_{j=1}^{n} \frac{d_1 + d_2}{d} \tag{1.15}$$

3. Area of the convex hull of the four endpoints of the actual and predicted cell wall, relative to the total cell area:
$$f_{i,area} = \frac{A_{convexhull}}{A_{cell}} \tag{1.16}$$

4. Smaller of the two angles between the diagonals of the convex hull of the four endpoints, divided by 90 degrees; if on of the endpoints falls inside the convex hull of the other three points, this devolves to the angle between the actual and predicted cell wall
$$f_{i,angle} = \frac{\varphi}{90} \tag{1.17}$$

5. Relative Euclidean distance in angle space; if the actual and predicted walls have endpoints at central angles $(\Theta_{A,1}, \Theta_{A,2})$ and $(\Theta_{A,1}, \Theta_{A,2})$ measured in degrees, then
$$f_{i,\Theta} = \frac{\sqrt{(\Theta_{A,1} - \Theta_{P,1})^2 + (\Theta_{A,2} - \Theta_{P,2})^2}}{90\sqrt{2}} \tag{1.18}$$

6. The Hausdorff distance between the actual and predicted cell division line. The Hausdorff distance between two sets gives the maximum distance in the first set to the nearest point in the second set. Hausdorff distances were estimated numerically by computing distances at 100 equally spaced points along each wall.

Each fitness measure was averaged over all 207 cell division. The results were sorted by fitness (lower is better) and clustered by location in -space to find a best fit vector, which could be used to, for example, to predict cell division, as implemented in Cellzilla.

### 1.3.5 Cellzilla Growth Model

Cell growth is described by a Hooke's law spring potential $\phi = \frac{1}{2}\sum k_{ij}(|\Delta x_{ij}| - \ell_{ij})^2$ applied to each pair of vertices, and summed over all adjacent vertices. Here $k_{ij}$ is a constant assigned to the wall joining vertex $i$ with vertex $j$, and $\Delta x_{ij}$ is an extension or compression of a virtual spring beyond its equilibrium length $\ell_{ij}$. The net force will pull vertex $v_i$ towards $v_j$ if if the spring is extended, and push the vertices apart if the spring is compressed, as described below by (1.19). Pressure is described as a force per unit wall length, so that it can be applied equally at each vertex.

Cellzilla is a two-dimensional tissue growth simulation extension for Cellerator[55]. Each cell is described as a single polygonal compartment. Growth occurs via dynamics assigned to each vertex $v_i$ as

$$\frac{dv_i}{dt} = -\sum_j k_{ij} \left( \frac{v_i - v_j}{|v_i - v_j|} \right) (|v_i - v_j| - \ell_{ij}) + \frac{1}{2} P \sum_j \sum_a n_{ij,a} |v_i - v_j| \tag{1.19}$$

where the sums over $j$ are over all vertices that are connected to $i$ and the sum over $a$ is over all cells that abut the edge connecting vertices $i$ and $j$. The first term describes a weak spring dynamics, where $k_{ij}$ and $\ell_{ij}$ are the spring relaxation constant and resting length for the edge connecting vertices $i$ and $j$. The second term describes an internal turgor pressure $P$ in each cell that is applied normal to the cell wall (normal vector $n_{ij,a}$ and divided equally between the vertices; similar dynamics have been used by others, e.g.[56, 57]). Isotropic linear growth is described by increasing the resting length of cells:

$$\frac{\ell_{ij}}{dt} = \mu \Theta \left( |v_i - v_j| - \ell_{ij} \right) \tag{1.20}$$

where

$$\Theta(x) = \frac{x + |x|}{2} \tag{1.21}$$

Cell division occurs when the cell passes a mass threshold. Each cell is randomly assigned a unique mass threshold at creation, with the population of thresholds distributed normally. The placement of the new cell wall may be assigned either by the modern interpretation of Errera's rule or a potential model as described elsewhere in the paper.

We optimized a the third component of the weight vector for growth direction rather than the geometrical prinicipal axis using a subset of cell divisions (14) using the protocol of Goodall and Green[52] to determine cell growth direction over a two hour period. The optimal weight vector shifted to w=(0.9, 0.4, 0). There was very little difference as either of the first two components (area and length) are varied. However, optimality rapidly decreases as the third component becomes non-zero. This would indicate that the actual instantanteous direction of growth (as measured over a two-hour period) is not a significant predictor of cell division.

The minimum fitness results were clustered around a weight vector of $w = (0.68, 0.73, 0, 0)$, where the three values represent the relative importance of area equalization, length minimization, and perpendicularity to cell elongation (Figure 1.14). Variations in the first component have very little

Figure 1.14: Result of optimization of potential.

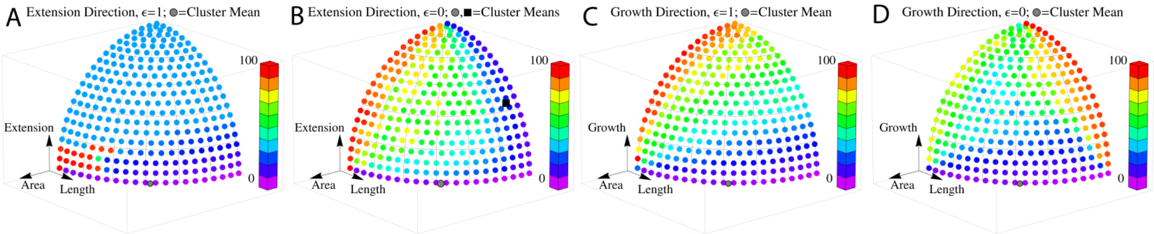

effect, except as $w_1 \to 1$, where it becomes rapidly worse for $w_1/w_2 > 19$. The fitness decreases gradually as $w_3$ increases from zero. There were no significant differences between the different types of fitness measure. All of our fits indicate that the third component in w is zero. This indicates that neither geometrical elongation nor instantaneous direction of growth (as measured over a two-hour period) are significant predictors of cell division.

When the constants $c_1$ and $c_2$ were relaxed to zero in (11) and (12) the minimum moved to $w = (1, 0.6, 0)$, with the valley of minimums spread widely along the equator (Figure 1.14c), indicating that almost any combination of area equalization and and length minimization will work so long as both factors are taken into account (i.e., avoiding the end-points of pure-length and pure-area). In the first set of optimization runs, area equalization was not so important because the length-potential forced the new wall to pass near the center. When this restriction is removed, a delicate balancing between length-minimization and area-equalization is required to compensate for this. The direction of cell elongation did not appear to be a significant driving factor in either situation; in fact, incorporation of this factor with $c_2 = 0$ seemed to make matters worse.

This result would, indeed, suggest that when the different predictors are dissociated in this manner, that the best predictor is the shortest length wall that passes near the center. This prediction is very similar to the modern interpretation of Errera's rule that the wall will form in the shortest path that divides the cell in half. To compare these statements, the predicted wall location according to this rule were computed for all 207 cell divisions. The distribution of fitnesses for a potential function minimization with $w = (0.68, 0.73, 0, 0)$ were slightly better than for the modern interpretation of Errera's rule (Figure 1.16). Thirteen of the 14 worst cases were the same cells for both methods. Visually there is very little difference between the two methods of prediction. Using a distance fitness measure, the potential method gave a better fit in 68 of the 207 cell division, the modern interpretation of Errera's method in 40 cases, and both had identical fitnesses in two cases. In the hindsight model the numbers were 36 (Errera), 2 (tie), and 72 (potential) (see supplemental material

Figure 1.15: Simulated z-projection of meristem grown from a single cell in Cellzilla after 1000 cell divisions. (a) The modern interpretation of Errera's Rule used for cell division. (b) Optimized potential model using $w = (0.1, 1, 0)$ (area, length, cell extension).

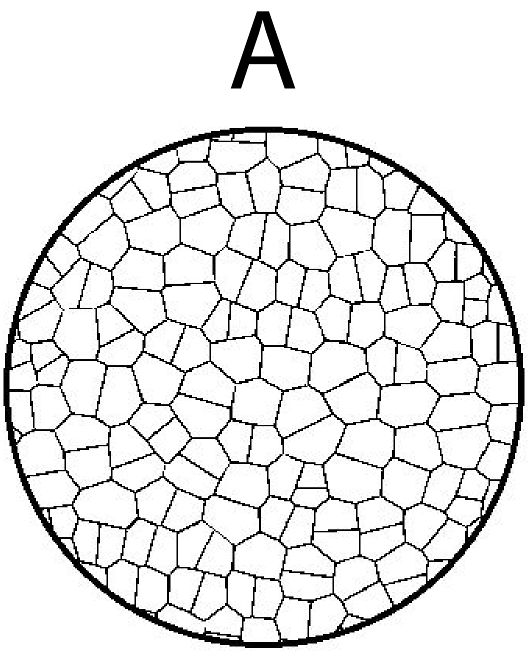

items 1 - 3).

Simulation results for both the modern interpretation of Errera's model and the optimized potential model are illustrated in Figure 1.15 after 1000 cell division have occurred (see also the movies in supplemental material 4 and 5). The tissues were grown in-silico from single quadrilateral cells and projected onto a parabolic surface. The resulting cell division patterns in both cases are evocative of observed data.

### Cell Division is a Boltzmann Distribution

Following the work of Besson and Dumais[9] we evaluated the hypothesis that selection of cell division surface may follow a Boltzmann distribution

$$Pr_{surface} = \frac{exp(-\beta \Delta V_{surface})}{Z(\beta)} \tag{1.22}$$

where $X(\beta)$ normalizes the distribution and beta is the inverse of temperature) in a phenomenological potential function, rather than actually minimizing the potential function for each cell all the time. In the limit of zero temperature such a model is equivalent to minimizing the potential; nonzero temperatures (finite betas) record departures from minimality. In this analysis we applied the prior authors' concept of a thermodynamic model to our data; we applied their model to our data to see how their potential function $\Delta V = lp$ compared with ours (4.5) in a thermodynamic analysis. We evaluated the Besson & Dumais model against our data, as our model uses straight lines for cell division and theirs uses arcs of circles. When we evaluated their model we used arcs of circles. Figure 1.17 supports this hypothesis with quantitative evidence from SAM cell images, both for our potential function (Equation (4.5) and Figure 1.17a) and for the Besson-Dumais potential function (Supplement Equation (1.13) and Figure 1.17a), though with a substantially lower effective temperature for our proposed potential function.

### 1.3.6 Model Predictions

The minimum fitness results were clustered around a weight vector of $w = (0.68, 0.73, 0, 0)$, where the four values represent the relative importance of area equalization, length minimization, perpendicularity to cell elongation and perpendicularity to growth direction (Figure 1.14). Variations in the first component have very little effect,except as $w_1 \to 1$, where it becomes rapidly worse for $w_1/w_2 > 19$. The fitness decreases gradually as $w_3$ increases from zero. There were no significant differences between the different types of fitness measure. All of our fits in the primary cluster indicate that the third component in w is zero. This indicates that neither geometrical elongation nor instantaneous direction of growth (as measured over a two-hour period) are significant predictors of cell division. A second cluster of minima occurs around $(0.02, 0.81, 0.58, 0)$ in the case where $c_p = 0$ in (1.12) corresponding to cell extension. No significant change was observed in changing the constant $c_p$ corresponding to cell growth direction, nor with any change with any change observed when the constant $c_L$ in (1.11) was changed.

This result would, indeed, suggest that when the different predictors are dissociated in this manner, that the best predictor is the shortest length wall that passes near the center. This prediction is very similar to the modern interpretation of Errera's rule that the wall will form in the shortest path that divides the cell in half. To compare these statements, the predicted wall location according to this rule were computed for all 207 cell divisions. The distribution of fitnesses for a potential function minimization with $w = (0.68, 0.73, 0, 0)$ was slightly better than for the modern interpretation of Errera's rule (Figure 1.16). Thirteen of the 14 worst cases were the same cells for both methods.

Figure 1.16: Comparison of predictions between the length-minimization potential, and the Besson-Dumais model. Dotted lines: actual new wall. Solid lines: predicted new wall.

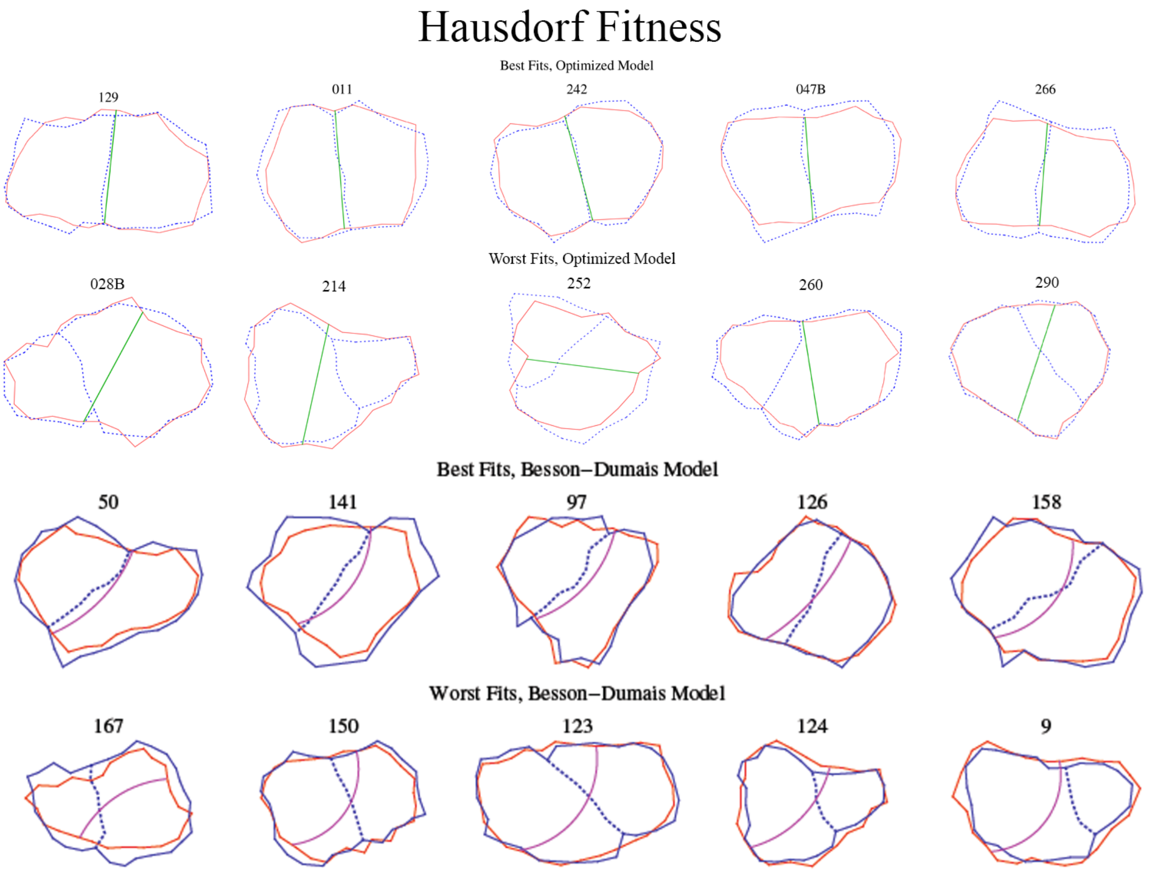

Visually there is very little difference between the two methods of prediction. Using a distance fitness measure, the potential method gave a better fit in 68 of the 207 cell division, the modern interpretation of Errera's method in 40 cases, and both had identical fitnesses in two cases. In the hindsight model the numbers were 36 (Errera) 2 (tie), and 72 (potential).

Simulation results for both the modern interpretation of Errera's model and the optimized potential model are illustrated in Figure 1.15 after 1000 cell division have occurred (see also the movies in supplemental material 4 and 5). The tissues were grown in-silico from single quadrilateral cells and projected onto a parabolic surface. The resulting cell division patterns in both cases are evocative of observed data.

### 1.3.7 Comparison to the Besson-Dumais Model

We evaluated the Besson-Dumais model on our data set by calculating the most likely wall location from among all allowed wall locations, where a wall location was allowed if its endpoints subtend a minimum central angle, as measured from the cell centroid, of 135 degrees (a restriction we have justified by the histogram in Figure 1.8c). In Figure 1.17 we compare the results of our model with the Besson-Dumais model. In order to make a valid comparison we computed the loghistogram of $|\Delta V|$, the difference between the predicted and actual potential used by the cell, for each model. For our model we plotted the log-histogram of $|\Delta V|$, where $V$ is computer by (4.5) and for the Besson-Dumais model we plotted the log-histogram of $|\Delta V|$ where $V = l/p$. In each case we computed the weighted least squares fit:

$$\log N = a|\Delta V| + b \tag{1.23}$$

where the slope $b$ and intercept $a$ are solutions of the normal equations

$$\begin{bmatrix} \langle|\Delta V|^2\rangle & |\Delta V| \\ |\Delta V| & 1 \end{bmatrix} \begin{bmatrix} a \\ b \end{bmatrix} = \begin{bmatrix} \angle|\delta V| \log N\rangle \\ \langle \log N \rangle \end{bmatrix} \tag{1.24}$$

The expectations are computed by defining a normalized weight vector $w = \frac{1}{N}n$, where n is the vector of counts in each bin, and $N = \sum n_i$. Then

$$\langle|\Delta V|\rangle = \sum w_i |\Delta V|_i \tag{1.25}$$

$$\langle|\Delta V|\rangle = \sum w_i |\Delta V|_i^2 \tag{1.26}$$

$$\langle|\Delta V| \log N\rangle = \sum w_i |\Delta V|_i \log n_i \tag{1.27}$$

$$\langle|\log N|\rangle = \sum w_i \log n_i \tag{1.28}$$

The negative of the slope corresponds to inverse temperature, the parameter $\beta$ in the Besson-Dumais model. As can be seen the resulting distributions are similar. The corresponding fits (the straight lines in Figures 1.17 A and B) have slope -10.4 (Besson-Dumais) and -62.1 (Potential Model). When a similar least squares fit was computed without the weighting the corresponding slopes were -9.0

(Besson-Dumais) and -45.9 (Potential Model). By comparison, the similar empirical fits by Besson-Dumais of a Boltzmann distribution with energy function $V_{BD} = l/p$, on their data in their figure 6B for four species (Coleochaete, Microsorum, Dionaea, and Zinnia) resulted in a slope of with a "universal" or cross-species best fit slope $\beta$ of 20.6. This difference of results for the potential function $V_{BD}$ may be accounted for by the different ways we and Besson-Dumais use the same potential function. Besson-Dumais consider just a few cell division surfaces between pairs of cell sides, allowing arcs; we consider straight lines, specified by two continuous intersection angles finely discretized into 10000 angle pairs, and restricted by central angle as above. Thus, in the direct comparisons that have been made, we find a substantially lower effective temperature $1/\beta$ and thus substantially less randomness, using our proposed potential function rather than that of Besson-Dumais.

## 1.4 Discussion

Previous work in this field has shown that rules must exist to control the positioning of new cell walls in the meristem in order to produce the patterns (size, shape, and connectedness) that are observed[43, 56]. Here we determined that the rules are not simple, and in fact the rules seem to be different depending on the location in the meristem. This might be a result of flower founder cells changing their "preferred" division polarity prior to the rapid growth characteristic of flower primordia. This is similar to the observation in vegetative meristems of pea plants where leaf founder cells often divide periclinally (parallel to the surface of the meristem) about one half plastochron before primordial growth where non-founder cells would usually divide anticlinally (perpendicular to the surface)[58, 59]. This is different than the phenomenon observed in Arabidopsis inflorescence meristems where periclinal divisions are not observed, but similar in that the divisions which don't abide by the modern interpretation of Errera's rule or our potential minimization rule are found preferentially near the edge, possibly in regions of flower founder cells. One explanation for the deviation from the rules near the perimeter of the meristem is that it helps make the elongated cells commonly observed in the boundary region of new primordia.

Explanations for these rules get more complicated when we consider the underlying mechanisms controlling plant cell divisions. Prior to cell division actin filaments and microtubules expand outward from the nuclear to the cellular membrane, in a pattern that resembles a concentric spoked wheel[60]. Following this, the region defined by the ends of the spokes develops the preprophase

Figure 1.17: Comparison of our model with that of Besson and Dumais [9]. Histograms show $log|\Delta V|$, the difference between the predicted and actual potential used by the cell, for each model. The negative of the slope corresponds to inverse temperature, and the parameter $\beta$ in the Besson-Dumais model.

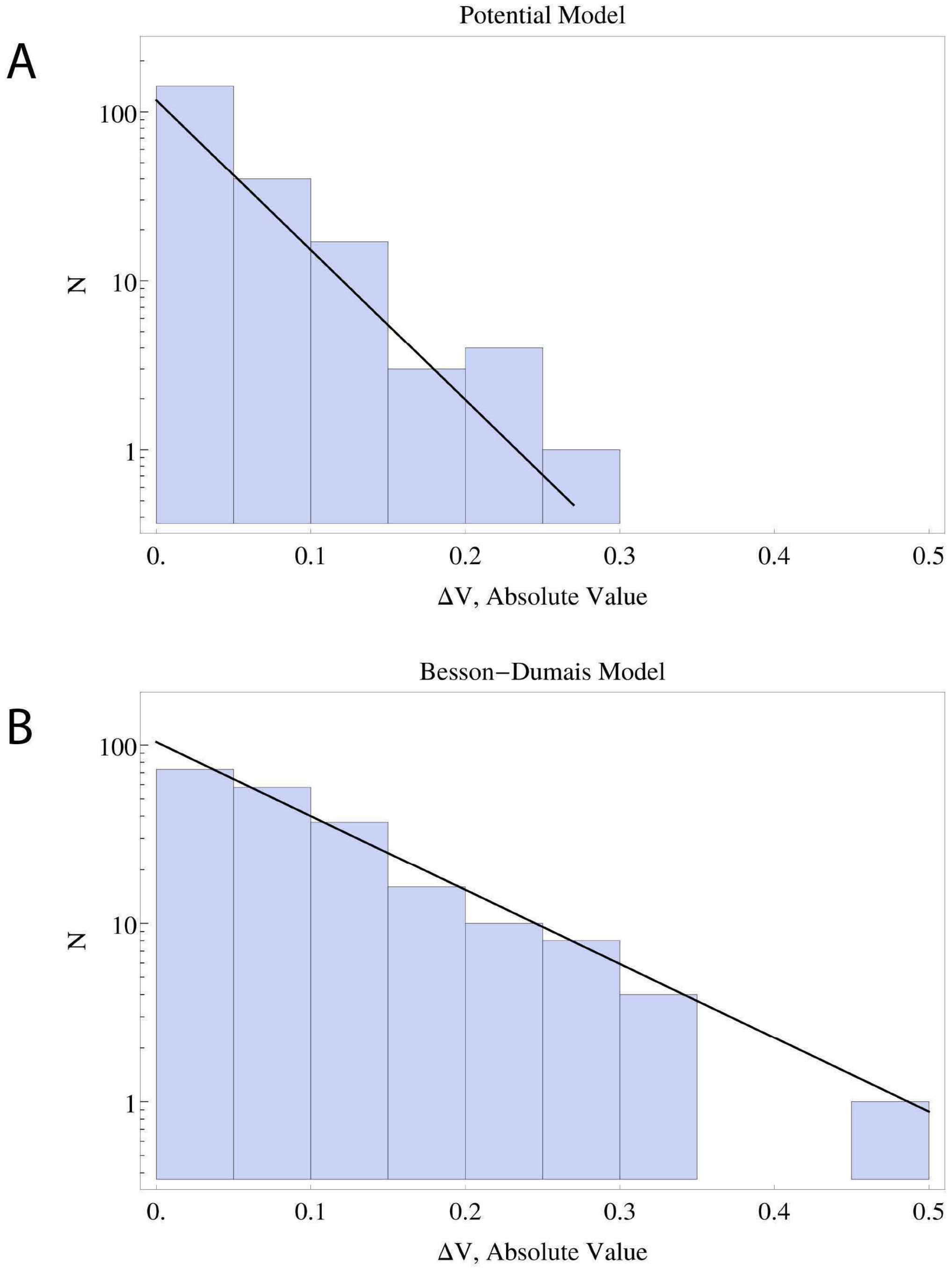

band of microtubules, which defines the position of the new cell wall. If the shape of the spoked wheel is then perturbed somewhat from circular, and the inner wheel is perturbed somewhat from the center of mass, we have an oblong cell with an off-center nucleus. Presuming that multiple spokes grow outward from the inner wheel, starting at the same time, the first spokes to reach the outer wheel will be the ones that have to travel the shortest distance. Reaching the outer membrane will induce a change in tensile forces and this could be transmitted as a signal back to the nuclear end of the spoke. In this model a new cell wall would be represented by the first two spokes to reach the outer wall, together with a collection of filaments tangent to inner circle (e.g., near the nuclear membrane) that connect them. At this point the full PPB has not coalesced yet and the filaments of the new proto-wall are free to increase their tension, forming into a more smoothly aligned curve that connects the two endpoints, perhaps tangent to the inner circle or even forming a straight line.

This argument would support a model in which shortest distance paths that pass close to the cell nucleus dominate (as suggested by a weight vector heavily dominated by the length potential). Since lines that pass through the center of the cell will, on the average, divide the cell in half, a rule stating that a new wall be the shortest path that divides the cell in half will emerge as a consequence. Furthermore, since the shortest distance from a point (e.g., the nucleus) to a line (e.g., the outer cell wall) is along a perpendicular path, Sachs' observation that new walls are perpendicular to existing walls and daughter cells are equal in volume[13] will also emerge. Finally, since the principal axis of elongation is, by definition, the longest axis of the cell, there paths will cluster about the shortest path normal to the principal axis that passes through (or nearly through) the cell center. Thus Hofmeister's Rule[11] is also emergent.

Nevertheless, the modern interpretation of Errera's rule is a poor predictor in a number of cases. In many of these cases the actual wall forms closer to the longest wall that divides the cell in half rather than the shortest. This may indicate that additional dynamic forces are involved in these cells that are not accounted for by a minimum length heuristic.

The model of shortest path that passes nearly through the cell center thus eliminates the need for the cellular machinery to somehow "sense" either the cellular orientation (elongation) or direction of growth. That biomechanical forces could affect the growth of the microtubules is nevertheless likely, perhaps changing their growth rate or causing a preferential growth direction. This could possibly explain the cases in which none of the traditional rules are followed.

It should be noted that this study only considered the first layer of cells in the meristem which have a uniform thickness and divide only periclinally. More could be learned about the mechanisms of cell division if divisions were observed in tissues that divide in all directions and the images were processed in 4D (3D z-stacks over time) using the methods of Fernandez et. al., for example[60]. Such a study would be indicative of how universal or narrow our rules are throughout plant tissues in general. Additional studies should also look at how cell divisions planes are affected by mechanical perturbations of the tissue prior to division.

# References

[1] Ian J Furner and Joanne E Pumfrey. “Cell fate in the shoot apical meristem of Arabidopsis thaliana”. In: *Development* 764 (1992), pp. 755–764.

[2] Jan Traas and Teva Vernoux. “The shoot apical meristem: the dynamics of a stable structure.” In: *Philosophical Transactions of the Royal Society of London. Series B, Biological Sciences* 357.1422 (June 2002), pp. 737–47. ISSN: 0962-8436.

[3] S Satina, AF Blakeslee, and Amos G Avery. *Demonstration of the Three Germ Layers in the Shoot Apex of Datura by Means of Induced Polyploidy Periclinal Chimaeras*. 1940.

[4] L Errera. “Über Zellformen und Seifenblasen”. In: *Botanisches Centralblatt* 34 (1888), pp. 395–398.

[5] Frederic T. Lewis. “The effect of cell division on the shape and size of hexagonal cells”. In: *The Anatomical Record* 33.5 (Sept. 1926), pp. 331–355. ISSN: 0003-276X.

[6] D’Arcy Wentworth Thompson. *On Growth and Form*. Cambridge University Press, 1992, p. 345. ISBN: 0521437768.

[7] E B Matzke. “The Three-Dimensional Shapes of Bubbles in Foams.” In: *Proceedings of the National Academy of Sciences of the United States of America* 31.9 (Sept. 1945), pp. 281–9. ISSN: 0027-8424.

[8] Clive W. Lloyd. “How does the cytoskeleton read the laws of geometry in aligning the division plane of plant cells?” In: *Development* 113.Supplement_1 (Jan. 1991), pp. 55–65.

[9] Sébastien Besson and Jacques Dumais. “Universal rule for the symmetric division of plant cells.” In: *Proceedings of the National Academy of Sciences of the United States of America* 108.15 (May 2011), pp. 6294–9. ISSN: 1091-6490.

[10] Laurie G Smith. “Division Plane Determination in Plant Cells”. In: *Plant Physiology*. Ed. by Lincoln Taiz and Eduardo Zeiger. 5th ed. Sinauer Associates, 2006. Chap. 16.1.

[11] W Hofmeister. “Zusatze und berichtigungen zu den 1851 veröffentlichen untersuchungen der entwicklung höherer kryptogamen”. In: *Jahrbucher fur Wissenschaft und Botanik* 3 (1863), pp. 259–293.

[12] T M Lynch and P M Lintilhac. “Mechanical signals in plant development: a new method for single cell studies.” In: *Developmental Biology* 181.2 (Jan. 1997), pp. 246–56. ISSN: 0012-1606.

[13] J Sachs. "Uber die Anordnung der Zellen in jungsten Pflanzentheilen". In: *Arbeiten des Botanisches Institut Wurzburg* 2 (1878), pp. 46–104.

[14] Nicolas Minc and Matthieu Piel. "Predicting division plane position and orientation." In: *Trends in Cell Biology* 22.4 (Apr. 2012), pp. 193–200. ISSN: 1879-3088.

[15] D J Flanders et al. "Nucleus-associated microtubules help determine the division plane of plant epidermal cells: avoidance of four-way junctions and the role of cell geometry." In: *The Journal of cell biology* 110.4 (Apr. 1990), pp. 1111–22. ISSN: 0021-9525.

[16] Edmund W Sinnott and Robert Bloch. "The Relative Position of Cell Walls in Developing Plant Tissues". In: *American Journal of Botany* 28.7 (1941), pp. 607–617.

[17] D.J Chadi. "Energy-minimization approach to the atomic geometry of semiconductor surfaces". In: *Surface Science* 299-300 (Jan. 1994), pp. 311–318. ISSN: 00396028.

[18] H.G. Timberlake. "The development and function of the cell plate in higher plants." In: *Botanical Gazette* 30.3 (1900), pp. 154–170.

[19] G Yamaha. "Uber die Zytokinese bei der Pollentetradenbildung, zugleich weitere Beitrage zur Kenntnis uber die Zytokinese im Pflanzenreich". In: *Journal of Japanese Botany* 3 (1926), pp. 139–162.

[20] Shinya Inoue. "Polarization optical studies of the mitotic spindle". In: *Chromosoma* 5.1 (Dec. 1953), pp. 487–500. ISSN: 0009-5915.

[21] J. D. Pickett-Heaps and D. H. Northcote. "Organization of Microtubules and Endoplasmic Reticulum During Mitosis and Cytokinesis in Wheat Meristems". In: *Journal of Cell Science* 1.1 (Mar. 1966), pp. 109–120.

[22] Chunhua Zhang, Leah E Halsey, and Daniel B Szymanski. "The development and geometry of shape change in Arabidopsis thaliana cotyledon pavement cells." In: *BMC plant biology* 11.1 (Jan. 2011), p. 27. ISSN: 1471-2229.

[23] Chris Ambrose and Geoffrey O Wasteneys. "Nanoscale and geometric influences on the microtubule cytoskeleton in plants: thinking inside and outside the box." In: *Protoplasma* 249 Suppl (Feb. 2012), S69–76. ISSN: 1615-6102.

[24] B Liu et al. "gamma-Tubulin in Arabidopsis: gene sequence, immunoblot, and immunofluorescence studies." In: *The Plant cell* 6.2 (Feb. 1994), pp. 303–14. ISSN: 1040-4651.

[25] Martine Pastuglia et al. "Gamma-tubulin is essential for microtubule organization and development in Arabidopsis." In: *The Plant cell* 18.6 (June 2006), pp. 1412–25. ISSN: 1040-4651.

[26] Natacha Janski et al. “The GCP3-interacting proteins GIP1 and GIP2 are required for $\gamma$-tubulin complex protein localization, spindle integrity, and chromosomal stability.” In: *The Plant cell* 24.3 (Mar. 2012), pp. 1171–87. ISSN: 1532-298X.

[27] M C Webb and B E Gunning. “The microtubular cytoskeleton during development of the zygote, proemhryo and free-nuclear endosperm in Arabidopsis thaliana (L.) Heynh.” In: *Planta* 184.2 (May 1991), pp. 187–95. ISSN: 0032-0935.

[28] Marisa S Otegui and L Andrew Staehelin. “Electron tomographic analysis of post-meiotic cytokinesis during pollen development in Arabidopsis thaliana.” In: *Planta* 218.4 (Feb. 2004), pp. 501–15. ISSN: 0032-0935.

[29] Jordi Chan et al. “Localization of the microtubule end binding protein EB1 reveals alternative pathways of spindle development in Arabidopsis suspension cells.” In: *The Plant cell* 17.6 (June 2005), pp. 1737–48. ISSN: 1040-4651.

[30] Yoshinobu Mineyuki, Takashi Murata, and MasamItsu Wada. “Experimental Obliteration of the Preprophase Band Alters the Site of Cell Division, Cell Plate Orientation and Phragmoplast Expansion in Adiantum Protonemata”. In: *Journal of Cell Science* 100.3 (Nov. 1991), p. 551. ISSN: 0021-9533.

[31] Jan Traas et al. “Normal differentiation patterns in plants lacking microtubular preprophase bands”. In: *Nature* 375.6533 (June 1995), pp. 676–677. ISSN: 0028-0836.

[32] Marleen Vanstraelen et al. “Cell cycle-dependent targeting of a kinesin at the plasma membrane demarcates the division site in plant cells.” In: *Current biology : CB* 16.3 (Feb. 2006), pp. 308–14. ISSN: 0960-9822.

[33] Amanda J Wright, Kimberly Gallagher, and Laurie G Smith. “discordia1 and alternative discordia1 function redundantly at the cortical division site to promote preprophase band formation and orient division planes in maize.” In: *The Plant cell* 21.1 (Jan. 2009), pp. 234–47. ISSN: 1040-4651.

[34] Lara Spinner et al. “The function of TONNEAU1 in moss reveals ancient mechanisms of division plane specification and cell elongation in land plants.” In: *Development (Cambridge, England)* 137.16 (Aug. 2010), pp. 2733–42. ISSN: 1477-9129.

[35] Juliette Azimzadeh et al. “Arabidopsis TONNEAU1 proteins are essential for preprophase band formation and interact with centrin.” In: *The Plant cell* 20.8 (Aug. 2008), pp. 2146–59. ISSN: 1040-4651.

[36] Christine Camilleri et al. “The Arabidopsis TONNEAU2 gene encodes a putative novel protein phosphatase 2A regulatory subunit essential for the control of the cortical cytoskeleton.” In: *The Plant cell* 14.4 (Apr. 2002), pp. 833–45. ISSN: 1040-4651.

[37] David Twell et al. “MOR1/GEM1 has an essential role in the plant-specific cytokinetic phragmoplast.” In: *Nature cell biology* 4.9 (Sept. 2002), pp. 711–4. ISSN: 1465-7392.

[38] J Christian Ambrose et al. “The Arabidopsis CLASP gene encodes a microtubule-associated protein involved in cell expansion and division.” In: *The Plant cell* 19.9 (Sept. 2007), pp. 2763–75. ISSN: 1040-4651.

[39] Chris Ambrose et al. “A CLASP-modulated cell edge barrier mechanism drives cell-wide cortical microtubule organization in Arabidopsis.” en. In: *Nature communications* 2 (Jan. 2011), p. 430. ISSN: 2041-1723.

[40] Stéphanie Drevensek et al. “The Arabidopsis TRM1-TON1 interaction reveals a recruitment network common to plant cortical microtubule arrays and eukaryotic centrosomes.” In: *The Plant cell* 24.1 (Jan. 2012), pp. 178–91. ISSN: 1532-298X.

[41] Pankaj Dhonukshe et al. “A PLETHORA-auxin transcription module controls cell division plane rotation through MAP65 and CLASP.” In: *Cell* 149.2 (Apr. 2012), pp. 383–96. ISSN: 1097-4172.

[42] Klementina Kakar et al. “CLASP-mediated cortical microtubule organization guides PIN polarization axis.” In: *Nature* 495.7442 (Mar. 2013), pp. 529–33. ISSN: 1476-4687.

[43] Bruce E. Shapiro et al. “Using Geometric Markers to Predict the Cell Division Plane in Meristem Cells”. In: *Proceedings of the 6th International Workshop on Functional-Structural Plant Models*. Ed. by Theodore DeJong and David Da Silva. Davis, CA, 2010, pp. 129–131.

[44] Daniel Kierzkowski et al. “Elastic domains regulate growth and organogenesis in the plant shoot apical meristem.” In: *Science* 335.6072 (Mar. 2012), pp. 1096–9. ISSN: 1095-9203.

[45] Tony J Collins. “ImageJ for microscopy”. In: *BioTechniques* 43.S1 (2007), S25–S30.

[46] SF Bockman. “Generalizing the Formula for Areas of Polygons to Moments”. In: *The American Mathematical Monthly* 96.2 (1989), pp. 131–132.

[47] L G Smith. “Plant cell division: building walls in the right places.” In: *Nature reviews. Molecular cell biology* 2.1 (Jan. 2001), pp. 33–9. ISSN: 1471-0072.

[48] Karen Alim, Olivier Hamant, and Arezki Boudaoud. “Regulatory role of cell division rules on tissue growth heterogeneity.” In: *Frontiers in plant science* 3 (Jan. 2012), p. 174. ISSN: 1664-462X.

[49] Dorota Kwiatkowska. “Structural integration at the shoot apical meristem: models, measurements, and experiments.” In: *American journal of botany* 91.9 (Sept. 2004), pp. 1277–93. ISSN: 0002-9122.

[50] L. G. Smith and S. Hake. “The Initiation and Determination of Leaves.” In: *The Plant cell* 4.9 (Sept. 1992), pp. 1017–1027. ISSN: 1532-298X.

[51] Donald E. Foard. “The initial protrusion of a leaf primordium can form without concurrent periclinal cell divisions”. In: *Canadian Journal of Botany* 49.9 (Sept. 1971), pp. 1601–1603. ISSN: 0008-4026.

[52] Colin R Goodall and Paul B Green. “Quantitative Analysis of Surface Growth”. In: *Botanical Gazette* 147.1 (1986), pp. 1–15.

[53] Viktor Blåsjö. “The Evolution of the Isoperimetric Problem”. In: *The American Mathematical Monthly* 112 (2005), pp. 526–552.

[54] Bruce E Shapiro, Elliot M Meyerowitz, and Eric Mjolsness. “Using cellzilla for plant growth simulations at the cellular level.” In: *Frontiers in plant science* 4 (Jan. 2013), pp. 1–9. ISSN: 1664-462X.

[55] Bruce E Shapiro et al. “Cellerator: extending a computer algebra system to include biochemical arrows for signal transduction simulations.” In: *Bioinformatics (Oxford, England)* 19.5 (Mar. 2003), pp. 677–8. ISSN: 1367-4803.

[56] Patrik Sahlin and Henrik Jönsson. “A modeling study on how cell division affects properties of epithelial tissues under isotropic growth.” In: *PloS one* 5.7 (Jan. 2010), e11750. ISSN: 1932-6203.

[57] Tim Rudge and Jim Haseloff. “A Computational Model of Cellular Morphogenesis in Plants”. In: *Lecture Note in Computer Science, Advances in Artificial Life*. 2005, pp. 78–87.

[58] M. E. Cunninghame and R. F. Lyndon. “The Relationship Between the Distribution of Periclinal Cell Divisions in the Shoot Apex and Leaf Initiation”. In: *Annals of Botany* 57.6 (June 1986), pp. 737–746. ISSN: 0305-7364.

[59] RF Lyndon. “Leaf formation and growth of the shoot apical meristem”. In: *Physiologie Vegetale* 10 (1972), pp. 209–222.

[60] Romain Fernandez et al. “Imaging plant growth in 4D: robust tissue reconstruction and lineaging at cell resolution.” In: *Nature Methods* May (June 2010). ISSN: 1548-7105.

# Chapter 2

# Modeling and Testing the Effect of Cell Size on Auxin Distribution

## 2.1 Introduction

In the 19th century, Charles Darwin was the first to propose that phototropism is caused by a transmissible substance which was later discovered by Kogl and Haagen-Smit and named auxin [1, 2]. Since then, auxin was determined to be a class of compounds comprised of an aromatic ring and a carbolxylic acid moiety that all have similar phenotypic effects on plants.

This hormone family is now known to be involved in the morphogenesis of many different organs and tissues within Arabidopsis. Members of this family are generally thought to move between cells through both diffusion and active transport and cause proliferation and differentiation where it accumulates in high concentration. This property of auxin is of particular interest because it provides a mechanism for explaining the formation of organs at particular, periodic locations even if the underlying mechanism of auxin transport is not fully understood. And the knowledge that we *do* have about auxin transport has allowed us, in the work described here, to create models that in some instances make accurate predictions about the phenotypes of various mutants. But in order to make such models, we first must understand some of the fundamentals of auxin biochemistry and auxin's role in tissue differentiation.

The transport of auxin through tissue is the focus of this work, but other aspects of auxin biochemistry are just as important during auxin-induced morphogenesis such as biosynthesis, metabolism, and sensing. The details of these processes are critical for the higher-order patterns spanning cells and organs. I this section I will first cover the basics of auxin synthesis, then the mechanisms of auxin transport, and finally the propagation of the auxin signal to the extent that it alters gene expression.

### 2.1.1 Synthesis

The most commonly studied member of the auxin family is Indole-3-acetic acid (IAA), which is found in concentrations as high as 250pg·mg$^{-1}$ in mature leaves, cotyledons, and both shoot and root meristem tissue[3, 4]. There are three known, independent pathways for synthesizing IAA. The first to be discovered was the tryptophan dependent pathway, although isotope labelling experiments showed that this was not the only pathway[5]. Initially this was thought to be the primary mechanism by which IAA is synthesized but experiments involving TRP2 and TRP3 mutants (mutants for tryptophan biosynthesis) showed similar or even *increased* levels of IAA compared to wild type tissue[6].

Once some of proteins required for IAA synthesis became known it became obvious that there were at least two distinct pathways. One of these pathways starts with indole-3-glycerol phosphate as a precursor while the other uses a tryptophan (Trp) precursor[7]. When radioisotope labelled tryptophan and anthranilate were introduced to trp2-1 (10% of wild type tryptophan production) mutants, mass spec isotope analysis of tryptophan showed that the majority of IAA was being produced independent of the labeled tryptophan[5]. Additional evidence of a tryptophan independent pathway was that in tryptophan synthesis mutants such as trp3-1 and trp2-1 the concentration of IAA is similar to that of wild type plants. Indole-3-glycerol phosphate was identified as the secondary pathway when indole-3-glycerol phosphate synthase antisense RNAs were introduced to trp2-1 and trp3-1 mutants and the resulting plants showed auxin deficient characteristics[6].

Today it is known that there are two distinct tryptophan independent IAA synthesis pathways. One of those pathways uses indole-3-acetaldoxime (IAOx) and the other, indole-3-pyruvate (IPA). The indole-3-acetaldoxime pathway is carried out by the two P450 monooxygenases CYP79B2 and CYP79B4[8, 9, 10, 11], although this pathway may be limited to the Brassicales and not play a major part in auxin synthesis across all plants[12]. The other pathway involving IPA is probably more widely used throughout the plant kingdom and recently has been characterized. Genetic screens have identified an aminotransferase that is responsible for catalyzing the synthesis of indole-3-acetaldehyde from IPA[13, 14]. Plants carrying mutations in this aminotransferase look similar to auxin signalling mutants and have severe early development phenotypes[13]. IAA can also be synthesized from IPA through flavin monooxygenase enzymes in the YUCCA family[15]. Over expression of these monooxygenase genes results in an increased concentration of indole-3-acetic acid[13, 16, 17, 18]. Additionally, these monooxygenases have been determined to be the rate limiting step in the IPA dependent pathway[19] and are tightly regulated with multiple redundancies[20, 21, 22, 23].

Even though the synthetic pathways for auxin synthesis have been extensively probed, the exact locations with the plant, tissue, and cellular organelles are still mysterious. In the model used in this study, auxin is assumed to be produced uniformly throughout the tissue at a steady rate and without regard to the subcellular localization. But in order the better understand the mechanisms by which auxin controls plant development, more work will be needed to characterize the spatial and temporal expression of the many genes involved in these synthetic pathways.

### 2.1.2 Transport

In Arabidopsis, auxin is known to be distributed through three distinct mechanisms regardless of the synthetic pathway or location of synthesis: diffusion through cytoplasm and extracellular space, transport (active and passive) across plasma membranes, and movement (diffusion and bulk transport) through vascular tissue. Looking specifically at cross-membrane movement, auxin is often transported in a polarized fashion. This polar auxin transport is critical both for generating local auxin maxima and in long distance transport. This transport occurs in a manner that depends on plasma membrane-localized proteins facilitating the movement of auxin from the cytoplasm to the apoplasm and vice versa. Many auxin carriers are well characterized: the PIN proteins[24] and several proteins of the ABCG and ABCB transporter family[25, 26, 27] are involved in auxin efflux from the cell and the AUX1 and LAX proteins are involved in auxin influx [28, 29].

While there are many proteins that transport auxin across membranes, the rate limiting step in polar auxin transport was determined to be the proteins in the PIN family[30, 31]. In the shoot apical meristem PIN1 specifically is the most highly expressed PIN and mutants of PIN1 have a lack of organ phenotype. But in other tissues other PINs play a larger role. PIN proteins are often found localized to predominantly one side of the cell, which leads to polar auxin transport. The

Figure 2.1: Indole-3-acetic acid (IAA) is a weak acid and is almost completely deprotonated in the neutral pH of the cytoplasm, preventing the charged conjugate base from diffusing through the lipid bilayer membrane. PIN1 transports IAA to the apoplasm where the pH is more acidic around 5.5. A significant portion of the IAA population becomes associated with H(+) ions, neutralizing the molecules' charge and allowing them to diffuse through the membrane into the cytoplasm of either a neighboring cell or back into the originating cell. Auxin importers like AUX1 also transport IAA across the membrane, where it becomes deprotonated and trapped again.

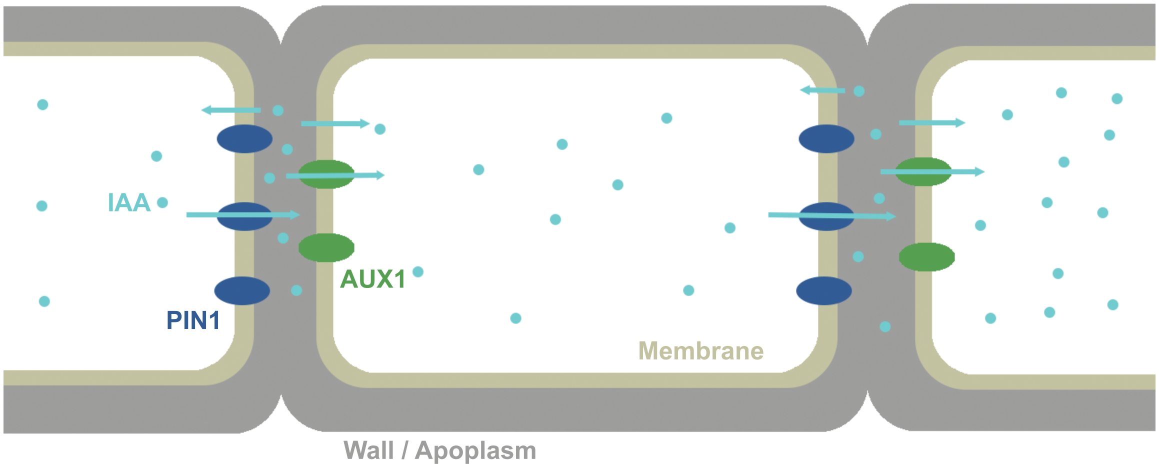

pattern of polarization of these PINs is often found to be correlated with local auxin concentration, as reported by DR5 expression[31]. The mechanism that controls this polarization involves many known components including cytoskeletal elements, vesicles, and ion signals[32, 33, 34, 35].

Currently, the most well accepted model for how PIN is localized involves PIN being secreted (to the plasma membrane, not into the apoplasm) equally to all sides of the cell. Subsequent endocytosis is polar and recycles PIN from only the sides of the cell where PIN will not be present[36]. A key component of this recycling mechanism is the endosome-localized GTPase GNOM, which is critical for endosome structure and required for proper PIN polarization[37, 38]. But there are also GNOM independent recyling pathways. For example, plasma-membrane-localized PINs can be phosphorylated by kinases, which label them for GNOM independent recycling[38, 39].

In addition to controlling the polarization of PIN proteins, recycling of PIN back to the lytic vacuole also regulates the overall concentration of PIN found in the membrane[40, 41, 42]. Part of this regulatory mechanism depends on auxin rather than proteins. Increased or decreased concentrations of indole-3-acetic acid can inhibit or promote the endosome-dependent recycling of PIN but how the concentration is sensed in this case is still unknown[40, 43, 44]. Additionally, through a mechanism unrelated to the processes just described, MAB4 is known to regulate overall PIN concentration at the plasma membrane and possibly have some role in PIN polar localization as well[45, 46, 47, 48]. Although this particular pathway is still largely unmapped, it is speculated that PINs are ubiquinated and the ubiquitin signal controls the movement of PINs through the secretory and endocytosis pathways[40, 49, 50].

Even though secretion and recycling are largely responsible for polar localization of PINs, the mechanism by which the cell "decides" which direction to polarize is not well known. There has long been speculation that mechanical forces are at least partially involved in morphogenesis in plants[51, 52]. Recent work has determined that both ablation and osmotic stress can cause PIN1 to polarize[53, 54]. In the case of cell ablation, PIN1 localized to the side the cell experiencing the most mechanical stress. This presents an intriguing potential mechanism for local accumulation of auxin. If increased auxin concentration leads to increased expansion, this expansion would put mechanical stress on the walls of neighboring cells. These cells would sense (through a yet to be discovered mechanism) one wall under more stress than the others and polarize PIN to that side of the cell, leading to polar auxin transport towards the neighbor with the highest auxin concentration (since that neighbor would generate the most mechanical stress).

It should be noted that most of this work has been done in roots and the exact proteins may vary in other tissues. Also, in the models used in this study, no mechanism is assumed for connecting mechanical forces to PIN localization.

### 2.1.3 Auxin Receptors and Signal Propagation

Auxin perception is mediated by a couple of independent signaling pathways. By far, the most well studied and well understood of these pathways involves the TIR1 receptor family and the transcriptional activators and repressors in the Aux/IAA, ARF, and TPL families.

Aux/IAA, ARF, and TPL proteins form a complex with DNA often within the promoter regions of auxin-responsive genes, and act as repressors[55, 56]. In the presence of auxin, TIR1/AFB and Aux/IAA bind together and additionally promote the ubiquitination and subsequent proteosome-mediated degradation of Aux/IAAs in this complex[57, 58]. It should be noted that each of these families has many members and the individuals form many distinct complexes with varying sensitivities to auxin and affinities for different DNA sequences[59]. The sensitivity to auxin is primarily determined by the Aux/IAA individuals while the DNA binding affinity is determined by both the TIR1 and Aux/IAA individuals.

Individual proteins of the ARF family of transcriptional regulators can act either as activators or repressors[60]. They can act on their own in the absence of other auxin-related factors or can work in tandem with Aux/IAA and TPL. The ARF activators usually form complexes with Aux/IAA while the ARF repressors tend to work independently of other factors[61]. Since the ARFs are not auxin receptors themselves, ARF repressors working independently of Aux/IAA are probably activated completely independently of auxin. This, in theory, provides a mechanism for other currently unknown processes to tune the auxin sensitivity of a particular promoter.

While this pathway is vast and complex, some of the details are important to the research I present here because of my use of the synthetic auxin-responsive promoter DR5. DR5 has long been used as a reporter of auxin signaling because it is activated downstream of the Aux/IAA/TIR1/ARF/TPL complex regardless of which exact individuals from those families were involved. But it is now becoming apparent that the DR5 promoter is probably only good for measuring the ratio of ARF activators and ARF repressors in a given cell. Recently, a new auxin reporter was created (DII-Venus) by fusing the auxin-interacting portion of an Aux/IAA protein with the Venus fluorescent protein[62]. This fusion protein is driven with a constituitive promoter and is on in all cells. When auxin is present, the Aux/IAA domain is ubiquitinated and degraded, destroying the Venus protein as well. This reporter system, while a more direct measurement of local auxin, does not necessarily measure the auxin-dependent transcriptional state[59, 62, 61]. But it does provide more information about the state of auxin distribution within a tissue.

Another auxin signaling pathway is the ABP1 pathway. ABP1 is a protein that can bind to and respond to primarily IAA[63]. It is found in both the apoplasm (outside of the cell) and in the lumen of the endoplasmic reticulum, although it is currently not known if ABP1 is inactive in one of these locations.

ABP1 is known to be involved in auxin-dependent regulation of cell cycle[64, 65]. It seems to be active in many different tissues including the root and shoot both during embryogenesis and later plant development[66, 67, 68]. The exact mechanism is not known but it is known to operate completely independent of the TIR1/Aux/IAA/ARF system just discussed[44, 69]. In fact, it may primarily act through post-transcriptional mechanisms[44, 69]. For example, ABP1 when bound to auxin can interfere with endocytosis, which subsequently can effect the polarization of PIN protein[43, 44], as discussed in section 2.1.2. This function is probably mediated through ROP GTPases[69]. But even though we have evidence of ABP1 acting through post-transcriptional mechanisms, it is known that it can in some instances affect the transcription of auxin responsive genes[68, 70]. But since BP1 is located in the apoplasm and ER while the known auxin-responsive transcription factors are in the nucleus, how this signal is propagated is currently unknown[70].

There is a third, less studied pathway that operates independent of the ABP1 and TIR1 pathways. This pathway involves a protein phosphatase called Indole-3-Butyric-Acid Response 5 (IBR5) which, despite the name, is able to respond to all known forms of auxin, not just IBA. Plants carrying mutations in IBR5 are smaller and have fewer lateral roots just like many mutants defective in auxin synthesis or signaling[71]. Unlike the case with TIR1 signaling, activation of the IBR5 pathway does not cause the deactivation of Aux/IAA proteins, so the transcriptional response is *probably* independent of ARF-mediated activation. But at this time the downstream targets are not known.

Regardless of the exact mechanism through which auxin is sensed, the end result is the activation of certain transcription factors involved in differentiation. This typically happens in local regions of high auxin accumulation.

### 2.1.4 Auxin Maxima

The current model of how organs initiate in Arabidopsis says that auxin accumulates in small regions composed of a few cells and that "maxima" of auxin leads to organ initiation. Multiple lines of evidence show that auxin is a major signal involved with the initiation of organ differentiation in a variety of Arabidopsis tissues and is both necessary and sufficient for the initiation process.

- Applying exogenous auxin to the surface of a wild type meristem causes the formation of organ primordia[72].
- Mutations in genes of auxin transporters lead to plants lacking some organs[73].
- Observations of the auxin transporter PIN1[31] suggest that auxin is being transported towards the locations where new flower primordia eventually form[74, 75, 76, 77].
- The synthetic auxin transcriptional reporter DR5 is highly expressed in areas of the shoot apical meristem where PIN1 appears to be transporting auxin towards and in the early flower primordia tissue[74, 76, 78].
- Observations of the recently developed DII-Venus reporter (see section 2.1.3) has corroborated the DR5 observations, further confirming the presence of auxin maxima at early floral organ sites.

Most of this evidence referenced is from work done in the shoot apical meristem. As a result, much of our current understanding of auxin maxima originated from shoot or root meristem observations. But some of the core concepts of auxin transport and maxima have been transferred to other tissues and have lead to a better understanding of their hormone-driven development. In the following sections I will cover auxin maxima in shoot meristems, roots, leaves, and the shoot vasculature.

### 2.1.5 Meristem Patterning

The Arabidopsis shoot apical meristem (SAM) is a dome shaped structure at the top (apical end) of the shoot that gives rise to all of the above-ground tissue. At the center of this structure is a group of slow-growing cells called the "central zone", commonly thought to be the stem cells of the SAM. Even though the SAM is actively growing the size of the central zone is maintained through a complex signlaing mechanism extensively reviewed by Jennifer Fletcher[79]. Outside of this circular region, cells differentiate and create the leaves or flowers which grow outward from the edge of the shoot in regular and predictable arrangements.

The arrangement of these organs around the SAM is a process called phyllotaxis. The pattern is composed of two components: the angles between successive organs called the divergence angle and the time between subsequent organs called the plastochron. The particular pattern displayed is often constant within a species but will sometimes change patterns when the meristem switches from vegetative to reproductive mode (switches from producing leaves to producing flowers). For example, both the leaves and flowers within Arabidopsis form a spiral pattern where each flower or leaf is positioned approximately 137° from the previous leaf or flower. Other patterns that can be formed by phyllotaxis are

- *alternate* - each successive organ is positioned 180° from the previous organ
- *opposite* - two organs form simultaneously 180° from each other
- *decussate* - like opposite but each 180° pair of organs rotates 90° relative to the previous pair
- *whorl* - similar to spiral but multiple organs are formed simultaneously creating multiple spirals.

The phyllotaxis pattern is the result of auxin patterning. Auxin accumulates in small regions around the periphery of the meristem outside of the central zone as a result of the complex processes described in sections 2.1.1 through 2.1.4. Regions of high auxin concentration begin differentiation into an organ and deplete the immediate surrounding tissue of auxin, preventing organs from forming in that region. Looking at the SAM from the top down and thinking of it as a flat, circular, 2D surface, each organ forms at a location at a particular angle with respect to the previous organ pivoting around the SAM apex. This angle is the phyllotaxis angle.

Since patterning of this tissue as we currently understand is dependent on the synthesis, polar transport, and signaling of auxin, perturbations to various components of this system should lead to disturbances in the wild-type phyllotaxis pattern. But mutations in the genes involved in synthesis, transport, and signaling of auxin don't lead to noticeable phyllotaxis defects, such as switching from a spiral to an alternate pattern. In order to understand how perturbations to the underlying mechanisms affect phyllotaxis in the SAM, precise measurements will be needed.

### 2.1.6 Root Patterning

The roots of Arabidopsis form branches, called lateral roots, similar to the above-ground branches and alternate the site of initiation 180° from the previous lateral root. These lateral root structures are important for gathering water and nutrients from the soil as they greatly increase the surface area. As the primary root grows downward some pericycle cells in the root become "founder cells" which eventually give rise to the lateral root [80]. All pericycle cells can divide when the concentration of auxin in that region becomes elevated with respect to neighbouring regions[81] but only some of these pericycle cell divisions lead to lateral root formation [82].

While we have known that auxin is required for lateral root formation since the discovery of the *alf3* and *alf4* mutation[83], the exact mechanism of the pattern has alluded us until recently. But there have been a number of observations over the past decade that gave us clues to the mechanism.

1. Mechanical stimulation of the root induces lateral root initiation [84]. When the root is forcefully bent a new lateral root often initiates on the outer edge of the bend, similar to how they usually initiate on the outer edge of the waves. Even in *arf7/arf19* double mutants this phenomenon is still observed which suggests the bending activates a pathway downstream of auxin-mediated transcriptional activation. These observations hint at a mechano-sensory component to the phenomenon but to date no one has discovered a mechanical force sensor in Arabidopsis.

2. The spacing of lateral root initiation is influenced by gravity. It has been observed that the lateral roots often form on the outside edge of an oscillating primary root. For example, Lucas et. al. showed through a combination of experiments and modeling that lateral root initiation and root gravitropism are co-regulated and that the gravitropism response has some influence on the lateral root patterning[85]. It it still unclear how much gravitropism influences lateral root initiation since the phenomenon is dependent on a particular geometry (oscillations along the length of the primary root) which is created independent of gravity. The phenomenon could probably be explained through a mechanism parallel to gravity sensing.

3. Auxin influences the space between the founder cells (and therefore the lateral roots) by priming the underlying xylem cells in the basal meristem by accumulating in certain protoxylem cells[86].

Given these observations, it is clear that Arabidopsis roots respond to a variety of inputs. Considering that roots must deliver a wide variety of nutrients, find water at varying depths, and avoid obstacles and traverse heterogeneous soils it is not surprising that they can respond to a variety of different stimuli. But it is still unclear if there is a master regulator of lateral root initiation that is influenced by these different inputs or if there are multiple, independent pathways that lead to lateral root initiation.

### 2.1.7 Auxin-Driven Patterning in other Tissues

It is sometimes assumed that the patterning of the vegetative (leaf producing) shoot apical meristem works similarly to the reproductive (flower producing) meristem with auxin being directed to locations around the periphery of the meristem. In the reproductive SAM, PIN1 mutants do not produce flowers. But in the vegetative SAM, PIN1 mutants still produce leaves[87]. So the assumption that both meristems work exactly the same is obviously flawed. We know that PIN1 is present in the Arabidopsis vegetative meristem[75] and that application of exogenous auxin to *tomato* vegetative meristem causes leaf primordia formation[72]. So assuming that auxin is still playing a similar role in the vegetative meristem is probably safe. But more work will be needed to determine how the vegetative SAM is able to produce leaves without PIN1. In particular, observing fluorescent proteins fused to other PIN proteins would probably yield interesting results.

Beneath the shoot meristem, vascular bundles form that are composed of xylem and phloem elements that transport water and nutrients throughout the plant. These bundles form in a circular pattern with regular spacing[88]. The auxin transporter PIN1 is known to be expressed in xylem and procambium cells, primarily polarized to the basal side of the cells but often laterally as well[24]. Inhibition of PIN1, either through genetic mutation or chemical inhibition, leads to an over-proliferation of xylem cells which spread out around the vascular ring more than in wild type. Additionally, recent work has shown that in brassinosteriod mutants, alterations to the size of the cells in the vascular ring lead to changes in the number of vascular bundles[89]. The authors speculate that an auxin patterning mechanism similar to SAM is at work in the vascular ring.

Leaf edge serrations are also thought to develop with a similar mechanism to the SAM. Leaf primordia arise from founder cells in the periphery of the vegetative SAM at sites of high auxin concentration. Development of a primordium to a mature leaf happens in two distinct stages. During "primary morphogenesis" the primodium grows through a combination of cell divisions and expansion. During this stage the leaf gets its basic shape and the vascular pattern forms and links up with the shoot vasculature. Then during "secondary morphogenesis" the leaf grows primarily through cell expansion until it reaches its final size[90, 91, 92]. It is during the primary morphogenesis stage where serrations at the edges of leaves are formed[93]. Polarized PIN1 transports auxin to sites around the leaf edge where it accumulates as evidenced by observations of pPIN1::PIN1-GFP and pDR5::GFP fluorescent reporters during leaf development[94, 95]. At the site of auxin maxima two things happen. First, PIN1 polarization flips and directs auxin inward through the leaf marking the location of vein formation[96]. Second, the cells in that regions divide and expand more than the cells in the auxin minima, ultimately leading to an outgrowth on the edge of the leaf called a serration. Since this process involves many of the same genes as the analogous process for primordia formation in the SAM, the spacing of the serrations is often thought work through the same mechanism.

Since the processes for auxin patterning just described involve many components and operate in tissues with complex geometry, efforts to understand them through back of the envelope calculations prove difficult. In order to further understand them, computer models than can solve many biochemical differential equations simultaneously are needed.

### 2.1.8 Modeling

As described in section 2.1.2, auxin has been long thought to influence its own distribution[97]. Given that we currently do not have a complete molecular understanding of the mechanism by which auxin is sensed and PIN proteins are localized, our current models for explaining auxin's self-influenced patterning assume two very different underlying phenomena. These models can be grouped into two paradigms: flux-based models and concentration-based models. All of these models have been created in a top-down approach where hypothetical mechanisms are devised to explain the observed patterns. And despite assuming completely different underlying mechanisms, both theoretical model paradigms are capable of producing patterns that look similar to the distribution of auxin in live tissue, as measured via DR5 expression.

The flux models are based on Sachs' canalisation hypothesis[97] which states that cells experiencing flux of a molecule in a certain direction will increase their capacity to transport the molecule in that direction and is based on the observation that during vein formation auxin transport channels become gradually more distinct. In early models, the degree of polar auxin transport is represented by a membrane permeability coefficient[98, 99]. After the discovery of PIN proteins, later models represented the polar auxin transport by coefficients representing concentration of PIN1 on the membranes, degree of polarization, and transport rates[100, 101, 102, 103, 104]. Primarily, these models have been used to understand the process of leaf vein formation. Small differences in initial PIN concentration or polarization are able to self-amplify and create patterns similar to those seen in leaf veins.

Concentration-based models[105, 106, 107, 108] were formulated after the discovery of PIN proteins and therefore all explicitly model membrane PIN levels. In these models, PIN levels increase on the membrane facing the neighbouring cell with the highest auxin level, i.e., up-the-gradient. This proposed feedback mechanism was inspired by observations in the shoot apex, where PINs in the epidermal layer orient toward local auxin maxima that develop into organ primordia [75, 78]. Concentration-based models are sufficient to obtain phyllotaxis-like patterns by amplifying small local increases in auxin into distinct maxima while simultaneously depleting neighbouring cells, resulting in the occurrence of new maxima at fixed distances from older maxima.

More recently, there has been a trend to make concentration based models that can behave like both flux-based and concentration-based models depending on the topology of the tissue and starting conditions[109, 108, 104]. This is the result of thinking that there is a single common mechanism underlying all auxin pattering phenomena. If a single mechanism *is* responsible for all auxin patterning in all tissues then a single model should be able to explain all of these observations. Additionally, even more complex models have been proposed that consider more than just cell geometry, auxin, and PIN1. As mentioned in section 2.1.2, there is evidence that mechanical forces are at play in the PIN1-auxin feedback loop. Based on these observations, models were made that incorporate stress-responsive alignment of microtubules, seeking to understand how mechanical stress is involved in phyllotaxis patterning[110]. Unfortunately, due to the nature of the math involved in calculating stress in an arbitrarily shaped tissue, the finite element method is required in this model which makes it difficult to incorporate other dynamic phenomena like cell division. Thus, while the model adequately explains how a stress-auxin-PIN1 feedback loop would work it cannot demonstrate the process in an actively growing phyllotaxis model. Although, it may be possible in the future to use a remeshed particle method to adequately model mechanical stress, auxin transport, and cell expansion and division in a single model[111].

In this work I seek to understand how universal our current understanding of auxin patterning is within the context of different *Arabidopsis* tissues, specifically SAM, root, leaf, and shoot vascular tissues. I will start by probing the robustness of our current phylloaxis model and determine which parameters alter the phyllotaxis pattern most dramatically. Using these computational observations, I will seek mutants that have defects in the parameters predicted by the model to have a large effect on phyllotaxis. Using these mutants I will observe auxin distribution in different tissues and determine if there are perturbations to the auxin distribution similar to those predicted by the model.

## 2.2 Methods

### 2.2.1 Plants and Growth Conditions

Seeds from the genetic backgrounds Col-0 (wild type), L-er (wild type), *msc3* (a.k.a. sqn-3), Wa-1 and *cycd3;1-3* were used. The wild type lines Col-0 and L-er were acquired from lab stocks. *msc3* seeds were a gift from Dr. Hirokazu Tsukaya at the University of Tokyo. *msc3* was originally identified in a T-DNA insertion library made with Col-0 plants, so *msc3* seeds were back crossed four generations before use. Wa-1 was acquired from the Arabidopsis Biological Resource Center, germplasm ID CS1586. *cycd3;1-3* seeds were acquired from Adrienne Roeder, who made the line using 2 EMS mutants and a T-DNA mutant (*cycd3;1*,*cycd3;2* and *cycd3;3*). This triple mutant was from both Col-0 and L-er backgrounds so it was back-crossed to Col-0 three generations before use. Triple mutant plants were initially identified by their large size and thick stems. Plants with the correct characteristics were self-crossed and lines that showed no segregation were confirmed to have the correct homozygous mutations and insertions using PCR and sequencing.

#### 2.2.1.1 Growing on Plates

When selecting seeds on plates, seeds were sterilized with 70% ethanol and added to agar plates. The agar plates were made with the following composition:

- 1% PhytoAgar
- 4.3g/L Murashige and Skoog Basal Salt Mixture
- 1mL 1000x concentrated Murashige and Skoog Vitamin Solution
- 30g/L sucrose
- 50ug/mL kanamycin monosulfate.
- 1L DI water

All components except for kanamycin were mixed in a 2L flask and then adjusted to a pH of 5.7 while mixing with a stir bar. The solution was autoclaved for 30min. When the temperature reached 60°C the kanamycin was added from a stock ethanol solution. Plates were poured in a sterile environment.

The sterilized seeds were dried on sterile filter paper and then applied to the MS agar plates. Plates were taped closed with filter tape and stored at 4°C. After a three day vernalization at 4°C, seeds were germinated under constant light at room temperature. 10 days after germination, healthy looking plants were transferred to soil.

**Materials for Growing on Plates**

- Murashige and Skoog Basal Medium (Sigma Aldrich, #M9274)
- Murashige and Skoog Vitamin Solution (Sigma Aldrich, #M3900)
- Sucrose
- Phytoagar (Spectrum Chemical, #40100072)
- Kanamycin (Sigma Aldrich, #60615)
- Deionized water
- Western incubation box 2.875" x 2.00" x 1.25" (Crystalgen, #G755)
- Filter tape, nonwoven, pressure sensitive (Carolina, #199708)
- 1M KOH
- Aluminum foil
- 25ml Serological pipet (USA Scientific, #1072-5410)

#### 2.2.1.2 Growing in Soil

When growing in soil, pots of soil were made using the following composition:

- 2 parts Sunshine Mix
- 2 parts SuperSoil Potting Soil
- 1 parts Vermiculite
- 1 parts Perlite
- 0.02 parts Marathon insecticide

Pots were arranged in flats of 12 pots and stored at 4°C for three days before transferring to a growth chamber with 24h illumination. Flats were given 1cm of water every two days.

**Materials for Growing in Soil**

- High wall petri dishes (Electron Microscopy Sciences, #64332)
- Sunshine Mix (McConkey Co, #SUNSM2)
- SuperSoil Potting Soil (SMG Growing Media)
- Vermiculite #2 Coarse (McConkey Co, #TRWVMIC26)
- Perlite (McConkey Co, #TRWPERL6)
- Marathon Insecticide 1% (OHP Inc, EPA #432-1329-59807)

### 2.2.2 Fluorescent Lines

A pDR5::2xGFP-N7 fluorescent reporter construct was built using standard Gateway cloning techniques. That construct was transferred to the pMOA33 plasmid, a binary plasmid carrying a kanamycin resistance cassette. In E. coli this plasmid was selected on LB agar using spectinomycin. This E. coli line was mated with an Agrobacteria tumefaciens line carrying the other half of the binary plasmid system and a helper E. coli line. The resulting Agrobacteria tumefaciens line was selected at 27°C on LB plates containing rifamycin, gentamycin, and spectinomycin as the Agrobacteria tumefaciens line contains a rifamycin cassette in its chromosome and a gentamycin cassette on its plasmid.

All Arabidopsis lines previously mentioned in section 2.2.1 were transformed using this pDR5::2xGFP-N7 line using the floral dip method. To transform these plants, seeds were first grown on soil, four plants to a pot, under continuous light. Primary shoots were clipped to encourage growth of multiple secondary shoots. Plants were ready to dip eight days after clipping. A large liquid culture of the Agrobacteria tumefaciens line was grown with LB rifamycin, spectinamycin, and gentamycin at 28°C. Cells were grown until mid log phase. The culture was spun down at 8,000rcf and then resuspended to an OD600 of 0.8 in a 5% aqueous sucrose solution. Before dipping, Silwet L-77 was added to the bacteria sucrose solution to a concentration of 500uL/L or 0.05% and mixed well. Plants were dipped in the bacteria solution for 30 seconds and then transferred to a covered flat with high humidity for 24 hours. These flats were stored at 16°C for four days and then transferred back to the original growth room, uncovered and exposed to continuous light.

Transformed seeds were grown on MS kanamycin plates as previously described. After roots emerged, plates were inverted and viewed under epifluorescent illumination at 100X magnification (10X 0.24NA objective, 10X eyepieces). Roots with high expression of GFP in the roots were marked and were later transferred to soil. These plants were self crossed and homozygous lines were determined after the third generation. Of these homozygous lines, meristems were dissected and observed with laser scanning confocal microscopy. Lines that had visible GFP expression in the meristem (in addition to expression in the roots) were selected for further experiments.

### 2.2.3 Meristem Experiments

Plants containing the pDR5::2xGFP-N7 fluorescent reporter as described in section 2.2.2 were germinated on MS and kanamycin agar plates and then transferred to soil as previously described in section 2.2.1.2. These plants were grown under continuous light until the shoots entered the reproductive phase and bolted. Flowers were removed with sharp forceps under a dissecting microscope. The meristem and approximately 5mm of stem were removed using forceps and placed in a glass slide. The slide was refrigerated for 15 minutes. This slows endocytosis, which would increase the background noise while imaging FM4-64.

High wall petri dishes were prepared with 1% phytoagar made with DI water. A 1mL solution of 5ug/mL FM4-64 in DI water was prepared from a 200ug/mL stock solution of FM4-64.

After the meristem tissue sat at 4°C for 15 minutes, 50uL of the FM4-64 solution was placed on each meristem using a 200uL pipette. The glass slide containing the meristems was placed back in the refrigerator at 4°C for another 15 minutes. Small holes were poked in the agar in the petri dishes. The meristems were removed from the slide and the drop of FM4-64 solution was removed with a Kimwipe. The Meristems were then stuck into the holes in the agar facing upward so the stems protruded into the holes, holding the meristems firmly in place. DI water was added to the petri dishes to a height 1cm above the top of the meristems.

Meristems in agar were imaged using a Zeiss LSM 510 laser scanning confocal microscope with a 63x 0.95NA Achroplan water dipping objective. The sample was excited using a single 488nm laser through a 488nm dichroic mirror which can excite both FM4-64 and GFP. A 500-525nm bandpass filter was used to capture light from GFP and a 650nm longpass filter was used to capture light from FM4-64 simultaneously.

Images from this procedure were processed using the technique described below in section 2.2.11. Meshes generated in MorphoGraphX were analysed to find the locations of fluorescent nuclei and the distance between those clusters of nuclei.

### 2.2.4 Root Experiments

Plants containing the pDR5::2xGFP-N7 fluorescent reporter as described in section 2.2.1 were germinated on MS and kanamycin agar plates as previously described in section 2.2.1.1. Five days after germination, healthy looking plants were transferred to glass slides. Slides were previously prepared with two pieces of 28 gauge steel wire glued to the slide oriented parallel and spaced apart less than the width of a cover slip to prevent the cover slip from crushing the roots. Each slide contained approximately five plants next to each other oriented in the same direction to make finding root tips easy under magnification. The slide was refrigerated for 15 minutes. This slows endocytosis, which would increase the background noise while imaging FM4-64.

A 1mL solution of 5ug/mL FM4-64 in DI water was prepared from a 200ug/mL stock solution of FM4-64. After the plants sat at 4°C for 15 minutes, 20uL of the FM4-64 solution was placed on each root tip using a 200uL pipette. The glass slide containing the roots was placed back in the refrigerator at 4°C for another 15 minutes. After removing the slides from the refrigerator, the drop of FM4-64 solution was soaked up with a Kimwipe. 75uL of DI water was added to the slide and a cover slip was added, crushing the cotyledons but leaving the roots in good condition. The cover slip was quickly tacked down with two drops of quick drying clear nail polish.

The roots were imaged using a Zeiss LSM 510 laser scanning confocal microscope with a 63x 0.95NA Achroplan water dipping objective. The sample was excited using a single 488nm laser through a 488nm dichroic mirror which can excite both FM4-64 and GFP. A 500-525nm bandpass filter was used to capture light from GFP and a 650nm longpass filter was used to capture light from FM4-64 simultaneously.

In order to capture images up the length of the root, many overlapping images were taken of each sample starting at the root tip and travelling approximately 500um up the root apically. Images were saved as LSM files then processed in the Fiji software suite[112]. The many images from each sample were stitched together into a single z-stack. In order to quantify the distance between DR5 expressing cells in the root, the number of cells between these points of interest were counted manually while the absolute distance was quantified using Fiji's built-in measuring tool.

### 2.2.5 Vascular Experiments

All the fluorescent lines previously generated in section 2.2.2 were used in the vascular experiments. Plants were grown on soil as described in section 2.2.1.2 until the plants were mature. Samples of each plant were taken by cutting a 2mm tall section of shoot using a razor blade. The samples were taken between the first and second carpel starting from the basal end of the shoot. These sections were fixed with formaldehyde, embedded with paraffin, stained and imaged.

**Materials Used**

- Paraformaldehyde (Sigma Aldrich #P6148)
- 1x Phosphate Buffered Saline solution, pH 7.4 (Life Technologies, #10010-023)
- NaOH, pelletized (Sigma Aldrich #221465)
- $H_2HSO_4$ (Sigma Aldrich #320501)
- Triton X-100 (Sigma Aldrich #X100)
- Ethanol, no denatured
- HistoClear (National Diagnostics #HS-200)
- DI water
- Paraplast Plus (Sigma Aldrich #P3683)
- Petri dishes
- Large plastic weigh boats
- Toluidine Blue O (Sigma Aldrich #T3260)
- Razor blades
- Glass scintillation vials (Wheaton Scientific #986746)

**Equipment Used**

- Leica Microtome
- Laboratory oven
- Heated water bath
- Slide Warmer

- Vacuum Chamber
- Glass jars
- Glass slide holders
- Forceps
- Metal spatula

### 2.2.6 Fixing

Fresh 4% paraformaldehyde (PFA) fixative was prepared. For 500 ml, 400 ml 1x PBS (130 mM NaCl, 7 mM $Na_2HPO_4$, 3 mM $NaH_2PO_4$ pH7.4) was warmed to 60°C and two pellets of NaOH were dissolved. In a fume hood, 20 g of paraformaldehyde was added and mixed thoroughly until dissolved. The solution was placed on ice and when cooled, the pH was adjusted to 7.2 with $H_2HSO_4$ (1-2 drops for 100ml). The volume was adjusted to 500 mL with 1x PBS.

Samples were harvested and placed immediately in 15 mL fresh PFA fixative on ice in glass scintillation vials. Large volumes of fixative were used; usually 20 volumes of fixative to one volume of tissue.

A vacuum (~500 mm Hg) was applied to the samples while on ice. The vacuum was held for 20 minutes while bubbles were released from the sample. The vacuum was slowly released and the samples were then transferred to a new solution of fixative to insure that the tissue remained in the right concentration of fixative. This vacuum step is applied repeatedly until the samples sink to the bottom of the jar of fixative, indicating that all the air bubbles have been released. When samples were not easily penetrated by the fixative, 0.1% Triton X-100 is added to the fixative and the procedure was repeated. Finally, the samples were once more transferred to new fixative and stored at 4°C overnight.

### 2.2.7 Embedding

A 1xPBS solution and a series of ethanol solutions were pre-cooled to 4°C. The samples were removed from the fixative solution and rinsed in 1xPBS on ice for 30 minutes. The samples were removed and then put in a fresh 1xPBS solution on ice for another 30 minutes.

The samples were removed from the 1xPBS solution and dehydrated with the following series of ethanol solutions.

- 10% ethanol 30 minutes
- 30% ethanol 30 minutes
- 50% ethanol 60 minutes
- 70% ethanol 60 minutes
- 85% ethanol 60 minutes
- 95% ethanol 60 minutes
- 100% ethanol 60 minutes
- 100% ethanol 60 minutes
- 100% ethanol 60 minutes

After the samples were taken through this entire series they were placed in a solution of 0.1% eosine in 100% ethanol and sat overnight at 4°C. Adding eosine to the samples made it easier to find them later once embedded in the semi-transparent paraffin.

Three ethanol/histoclear mixtures (3:1 v/v, 1:1 v/v, and 1:3 v/v) were prepared at room temperature in glass jars as well as a jar of 100% histoclear. The vials containing the samples in ethanol and eosine were decanted and then the following series of mixtures was added to the vials, decanting in between each one.

- ethanol/histoclear (3:1 v/v) 90 minutes
- ethanol/histoclear (3:1 v/v) 90 minutes
- ethanol/histoclear (3:1 v/v) 90 minutes
- 100% histoclear 90 minutes
- 100% histoclear 90 minutes
- 100% histoclear 90 minutes

Paraplast chips were placed in a beaker and heated to 60°C in a laboratory oven to melt the paraffin. When not being used the beaker of paraffin was stored at 60°C. The samples is histoclear were poured into large plastic weigh boats. Molten paraffin was added to the weigh boats and then the weigh boat was placed in the 60°C for one hour. After an hour, more molten paraffin was poured into each weigh boat. This was repeated every hour for eight hours. Then the histoclear/paraffin mixture was decanted from the weigh boat, leaving the samples behind with a minimal amount of histoclear/paraffin. Fresh molten 100% paraffin was added to the weigh boats. The weigh boats were left overnight at 60°C.

The following day the molten paraffin was replaced with fresh paraffin every four hours, three times. The weigh boats were kept at 60°C the entire time. The following day this procedure was repeated another three times.

The following day a petri dish was filled with molten paraffin and warmed to 60°C. The samples in the weigh boat were transferred to the petri dish using a warm metal spatula. Once all the samples were in the petri dish of paraffin they were arranged to all be oriented the same direction sitting side by side. This makes it easier to cut around them later.

The petri dish was then cooled to room temperature and the paraffin hardened. The dish was left at room temperature for three hours to ensure the paraffin had hardened all the way through. Once it was completely solid a razor blade was used to cut small cubes of parafin out, each one containing a single tissue sample. The cubes were trimmed down to approximately 5mm by 5mm in size so there was a minimal amount of excess paraffin.

Each sample was then placed on a microtome pedestal. The concave surface of the pedestal was filled with molten paraffin and the sample, embedded in a cube of paraffin, was held with forceps on top of the molten paraffin while it solidified. The pedestal was then mounted on the microtome.

### 2.2.8 Sectioning

After a pedestal was mounted on the microtome, the blade was aligned with the sample and the pedestal was rotated so the blade would cut through the narrowest side of the block first. The microtome was set to 10um increments and then gently turned so that the sample formed a ribbon. The ribbon was floated in a 40°C water bath and then removed using a small paint brush. The ribbon was placed on a glass slide. The glass slide was then placed on a 40°C slide warmer and left to dry for one hour.

This procedure was done for each sample and then the slides were labelled with a marker.

Before removing the paraffin, the samples were stained with Toluidine Blue O. A solution of 0.05%

(w/v) Toluidine Blue O was made in 10mL of DI water. This solution was added to a glass slide jar and the slides were placed in the solution for 30 minutes. The slides were then removed and rinsed with DI water.

To remove the paraffin from the samples and slides, first a series of histoclear and ethanol baths were prepared. These liquids were placed in glass slide holders so the slides would easily stand up in the liquid, keeping part of the slide above the liquid for easy handling. The slides were taken through the following series without drying in between.

- histoclear 10 minutes
- histoclear 10 minutes
- 100% ethanol 1 minute
- 95% ethanol (5% DI water) 1 minute
- 85% ethanol (15% DI water) 1 minute
- 70% ethanol (30% DI water) 1 minute
- 50% ethanol (50% DI water) 1 minute
- 30% ethanol (70% DI water) 1 minute
- 10% ethanol (90% DI water) 1 minute
- 100% DI water 1 minute

The slides were then air dried for 30 minutes and then either stored in a slide box at 4°C or imaged immediately.

### 2.2.9 Imaging and Analysis

Slides were viewed on a Zeiss Axioskop with a 5x Plan-Neofluar 0.15NA objective. Bright field illumination was provied by a 10W tungstem bulb. Condenser and light source adjustments were made and then images were taken with a Zeiss Axiocam 105 Color camera.

Image files were exported as TIF files from the Zeiss ZEN software. These files were then opened in Fiji[112]. A plugin call *cell-counter* was added to Fiji to assist in numbering cells. Each cell around the base of the vascular ring was counted and numbered using the labelling tool provided by the *cell-counter* plugin.

Once the cells were done being counted, an XML file containing the label data was exported and stored with the TIF images. The number of cells was recorded for each sample.

### 2.2.10 Leaf Experiments

**Materials Used**

- FM4-64 (Life Technologies #T-3166)
- DI water
- 75mm x 25mm glass slides (Sigma Aldrich #CLS294775X50)
- 25mm x 25mm glass cover slips (Sigma Aldrich #Z692263)
- Superglue (Cyanoacrylate adhesive)

**Equipment Used**

- Zeiss LSM 520 laser scanning confocal microscope
- Zeiss Stemi SV11 dissecting microscope
- Forceps
- 200uL pipette

Plants containing the pDR5::2xGFP-N7 fluorescent reporter as described in section 2.2.1 were germinated on MS and kanamycin agar plates as previously described in section 2.2.1.1. Five days after germination, healthy looking plants were transferred to glass slide using forceps. A dot of Superglue was placed on the glass slide and the plant was stuck into the glue root side down with the cotyledons oriented upward. This holds the small plant in place so the meristem and leaves can be dissected easily. The cotyledons were dissected away with sharp forceps under a dissecting microscope with 10x magnification, exposing the youngest leaves. These leaves were removed by gently pushing with the forceps.

Slides were previously prepared with two pieces of 28 gauge steel wire glued to the slide oriented parallel and spaced apart less than the width of a cover slip to prevent the cover slip from crushing the leaves. Each slide contained approximately five leaves next to each other oriented in the same direction.. The slide was refrigerated for 15 minutes. This slows endocytosis, which would increase the background noise while imaging FM4-64.

A 1mL solution of 5ug/mL FM4-64 in DI water was prepared from a 200ug/mL stock solution of FM4-64. After the plants sat at 4°C for 15 minutes, 20uL of the FM4-64 solution was placed on each leaf using a 200uL pipette. The glass slide containing the leaves was placed back in the refrigerator at 4°C for another 15 minutes. After removing the slides from the refrigerator, the drop of FM4-64 solution was soaked up with a Kimwipe. 75uL of DI water was added to the slide and a cover slip was added. The cover slip was quickly tacked down with two drops of quick drying clear nail polish.

The leaves in agar were imaged using a Zeiss LSM 510 laser scanning confocal microscope with a 63x 0.95NA Achroplan water dipping objective. The sample was excited using a single 488nm laser through a 488nm dichroic mirror which can excite both FM4-64 and GFP. A 500-525nm bandpass filter was used to capture light from GFP and a 650nm longpass filter was used to capture light from FM4-64 simultaneously.

### 2.2.11 MorphoGraphX Image Processing

LSM images of the meristem were processed to extract the positions of the cell walls in the first layer and the locations of fluorescent nuclei. This procedure relies on the software MorphoGraphX[113] and some particular computer hardware and software.

#### 2.2.11.1 Computer Hardware

- At least 16GB of RAM.
- Nvidia graphics card, 2GB of RAM or more recommended.

#### 2.2.11.2 Software

- Linux operating system.
    - Ubuntu or Kubuntu will be simplest if you are not an experienced Linux user.
    - The distribution must be able to run proprietary NVIDIA graphics drivers.
- MorphoGraphX[113] (Lab of Richard Smith, Max Planck Institute for Plant Breeding Research)

  Other software that can be used in place of MorphoGraphX

  - MARS-ALT[114]
  - Bitplane Imaris
- ImageJ[115] (Fiji[112] is preferable)

The first step for importing the data into MorphoGraphX was to convert the z-stack into TIFF format. The easiest tool for this job is ImageJ or Fiji, which is a particular distribution of ImageJ with many useful plug-ins already installed. In this work Fiji was used in place of ImageJ but ImageJ can be used also. In that case a plug-in would need to be installed which allows ImageJ to read the particular z-stack format, in this case an LSM file (LSMToolbox for Zeiss LSM files, Loci_tools for Leica LIF files, Bio-formats for Nikon ND2 or Zeiss CZI files).

In order for MorphoGraphX to interpret the image file correctly the first image in the series to be the top of the meristem. When the order was reversed the data was exported as a series of individual TIFF files rather than a multi-TIFF so the order of the images could be reversed.

Before beginning the image processing, some steps were taken to taken to insure all the software was set up and our data was ready to be processed.

- ImageJ or Fiji was installed
- MorphoGraphX was installed. On Ubuntu this can be done through the built-in package manager.
- The x,y,z dimensions of the voxels from the image file metadata were retrieved.

#### 2.2.11.3 Multiple TIFF Images

When exporting the image data from LSM files into a series of TIF images, the following procedure was used.

1. Open ImageJ or Fiji.
2. Click on *File*, then *Save As*, then *Image Sequence*.
3. Select the TIFF format and start the numbering at 0.
4. Click *OK*.
   - This will create multiple image files.
   - One file for each slice in the z-stack.

Figure 2.2: Example of an image processed in MorphoGraphX. **A.** Z-stack loaded. **B.** After surface detection. **C.** Side view after editing of surface to remove extraneous parts. **D.** Creation of coarse mesh. **E.** Image data mapped onto mesh surface. **F.** Smoothing of the data on mesh surface.

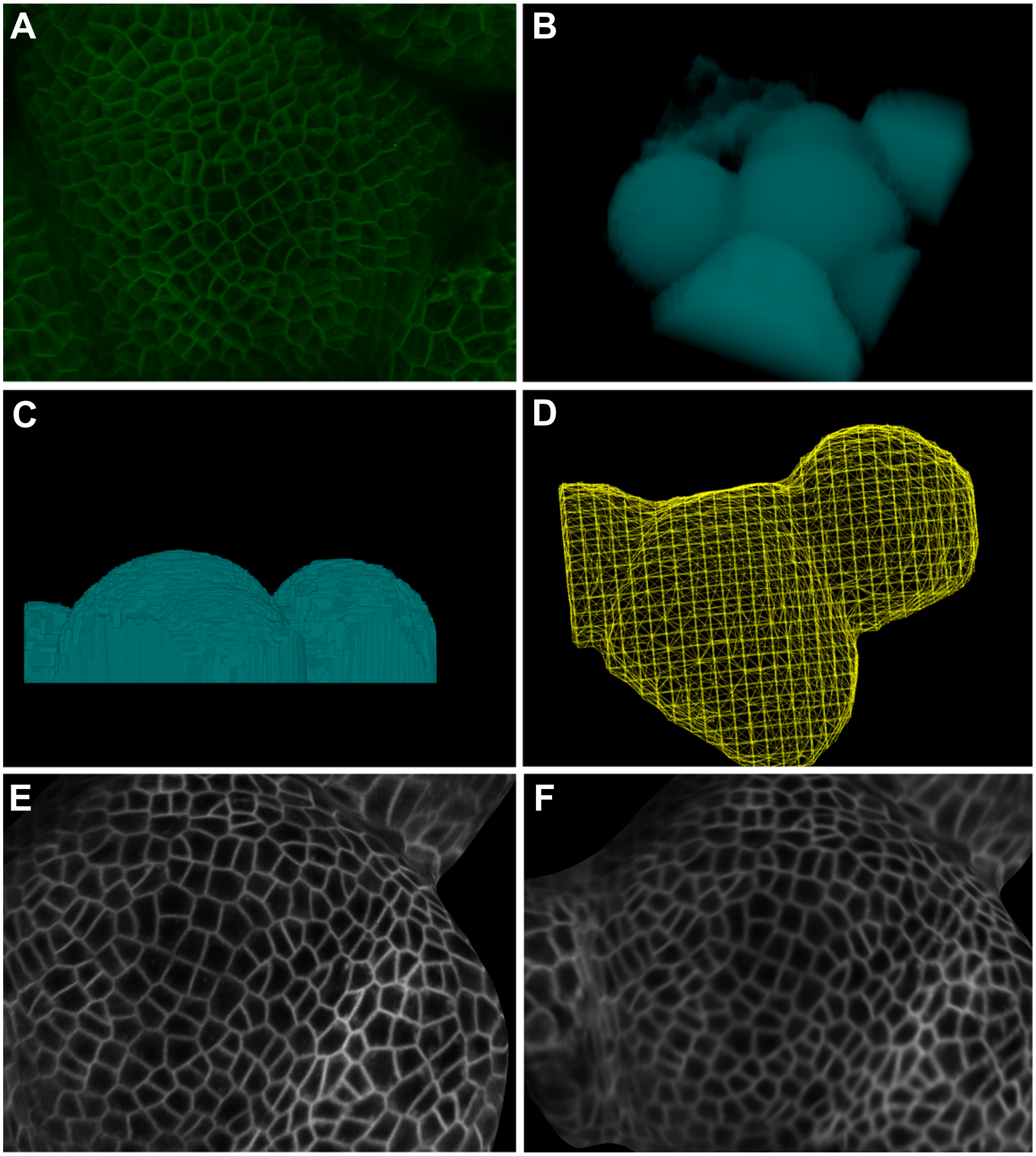

The following Bash script (OSX, Linux or Cygwin environments only) was used to reverse the numerical order of the TIF file names when needed. This assumes the files are named like "image3.tif". The second line of the script can be modified if the files are named differently. The script was copied into the same directory as the multiple TIFF files and run.

```
#!/bin/bash
image=( image*.tif )
MAX=${#image[*]}
for i in ${image[*]}
do
   num=${i:5:3} # grab the digits
   compliment=$(printf ’%03d’ $(echo $MAX-$num | bc))
   ln $i copy_of_image$compliment.tif
done
```

In order to import these TIF images into MorphoGraphX, the following procedure was used:

1. The MorphGraphX program was started.
2. In the top menu bar select *Stack* then *Stack1* then *Main* then *Image Sequence*.
3. Click *Add Files*.
4. Select all of the image files in the series.
5. Click *OK*.
6. Input the X, Y, and Z dimensions of the voxels in micrometers.
    - These data were available in the metadata associated with the original image file.
7. Click *Start* and the stack appears in the main window in a semi-transparent state as seen in Figure 2.2A.

#### 2.2.11.4 Single TIFF Image

In order to export the data as a single multi-TIFF image, the following procedure was used:

1. Click on *File*, then *Save As*, then *Tiff*.
2. Select the TIFF format and start the numbering at 0.

    - This creates multiple image files, one for each slice in the z-stack.
    - This file is imported into MorphoGraphX.

3. Open the MorphoGraphX program.
4. Drag the TIFF file into the main window.
    - This opens a window where the X, Y, and Z dimensions of the voxels in micrometers are manually entered.
    - These data were available in the metadata associated with the original image file.
5. Click *Start* and the stack appears in the main window in a semi-transparent state as seen in Figure 2.2A.

#### 2.2.11.5 Building the Mesh

To convert the image data into a mesh representing the surface of the meristem the following procedure was used:

1. On the right side, select the *Process* tab, then the *Stack* tab.
2. Expand the *Morphology* section.
3. Click on *Closing*.
4. Change the *X Radius*, *Y Radius*, and *Z Radius* parameters to 15.
5. Click *Go*.
6. Confirm that the cell boundaries are no longer visible and the meristem looks like a solid mass.
    - The original data is still unmodified in *Main*, *Stack1*, *Work*.
    - If the cells are still visible, increase the *Radius* parameters.
7. Click on *Edge Detect*.
8. Modify the parameters that appear towards the bottom.
    - The values for these parameters depend on the brightness and the amount of background noise in the data.
    - Start with the default values but change *Threshold* to 100000.

9. Make sure the surface looks relatively smooth as in Figure 2.2B.
    - There should be no large spikes protruding from the surface.
    - Experiment with different parameters.
10. Erase any structures that you do not want included in the mesh like flower primordia.
    - 10.1. At the top of the window select the *Pixel Edit* tool.
    - 10.2. To erase, hold *Ctrl* and *Alt* and click regions with the left mouse button.
    - 10.3. When not holding *Ctrl* and *Alt* use the mouse to move and rotate the image.
    - 10.4. Use the mouse scroll wheel to zoom in and out.
    - 10.5. Look for small extraneous bits around the meristem and erase those, too.
    - 10.6. With the opacity turned up, it should look like Figure 2.2C.
11. In the *Process* tab, click the *Mesh* tab and expand the *Creation* section.
12. Select *Marching Cubes Surface*.
13. Try the default parameters and click *Go*.
14. To view the mesh:
    - 14.1. Go to the *Main* tab, then the *Stack 1* tab.
    - 14.2. Disable *Main* and *Work*
    - 14.3. Enable *Mesh*
    - 14.4. Choose *ALL* from the *View* dropdown menu.
    - 14.5. It should look similar to Figure 2.2D.
15. Go to the *Process* tab, then the *Mesh* tab, in the *Structure* section select *Smooth Mesh* and click *Go*.
16. Select *Subdivide Mesh* and click *Go*.
17. Repeat steps 15 and 16 until there are at least 1 million vertices.
    - This number can be found at the bottom of the window.
    - More vertices will improve accuracy at the expense of memory usage.

- At some point more vertices is no longer helpful.

18. Remove the bottom of the mesh.
    18.1. Position the meristem so you are facing it from the side. Double clicking will snap it into place.
    18.2. On the right side of the window, choose the *Select Points in Mesh* button.
    18.3. Hold hold *Ctrl* and *Alt* and use the mouse to select the entire bottom of the mesh.
    18.4. Use the *Del* key to remove the selected vertices.
19. Map the image data onto the mesh.
    19.1. Select the *Main* tab.
    19.2. Make sure the *Main* stack is selected rather than the *Working* stack.
        - This determines which data will be mapped onto the mesh.
    19.3. Select the *Process* tab.
    19.4. In the *Mesh* tab expand the *Signal* section.
    19.5. Select *Map Signal*.
    19.6. Choose 1$\mu$m for the *Min Dist* parameter and 4$\mu$m for the *Max Dist* parameter.
    19.7. Click *Go*.
    19.8. Go the the *Main* tab. Unselect *Work* and select *Mesh*. This should display the image data mapped onto the mesh.
    19.9. It should look similar to Figure 2.2E.
20. Confirm that the image data mapped on to the mesh looks good.
21. If deeper cells layers are appearing on the surface, experiment with the parameters in step 19.6.
22. Select *Smooth Mesh Signal* from the *Signal* section.
23. Click Go. This will smooth out the image data to help the segmentation algorithm produce straighter boundaries. It should look similar to Figure 2.2F.

Now the data are mapped onto the mesh. The meshed was viewed by turning off the stacks. When the image looked jagged or overly pixelated, more vertices were added to the mesh using steps 15 and 16 and then re-maped the data onto the mesh using step 19. Then the image was ready to be segmented.

The previous steps were automated using MorphGraphX's Python scripting capabilities. The following code performs the steps automatically but can't be paused to view the intermediate steps. When intermediate steps are needed to be viewed, parts of the code were commented out.

To run Python code in MorphoGraphX, the code was first saved to a text file that has the *.py* file extension. In MorphoGraphX click on the *System* tab, then select *Python.* Choose the file that contains the Python code, then click *Go.*

```
Stack.Closing(15,15,15)
Stack.Edge_Detect(100000,2,0.3,30000)
Mesh.Marching_Cubes_Surface(5,5000)
Mesh.Smooth_Mesh(1)
Mesh.Subdivide()
Mesh.Smooth_Mesh(3)
Mesh.Subdivide()
Mesh.Smooth_Mesh(1)
Mesh.Subdivide()
Mesh.Subdivide()
Mesh.Project_Signal("No",1,3,0,50000)
Mesh.Smooth_Mesh_Signal()
```

When running an older version of MorphoGraphX the stack often requires more processing before the edge detection step. In that case the following code was used.

```
Stack.Resize_Canvas("Yes","Yes",0,0,40)
Stack.Shift_Stack(0,0,20)
Stack.Average(1,1,1,1)
Stack.Closing(15,15,15)
Stack.Edge_Detect(100000,2,0.3,30000)
Mesh.Marching_Cubes_Surface(5,5000)
Mesh.Smooth_Mesh(1)
```

Figure 2.3: Segmentation of cells in MorphoGraphX. **A.** Seeds drawn on the mesh. One seed is drawn in the center of each cell. This helps the watershed segmentation algorithm correctly differentiate between different cells. **B.** After watershed segmentation. **C.** Creation of cells using 1$\mu$m line segments. **D.** Side view of the cells.

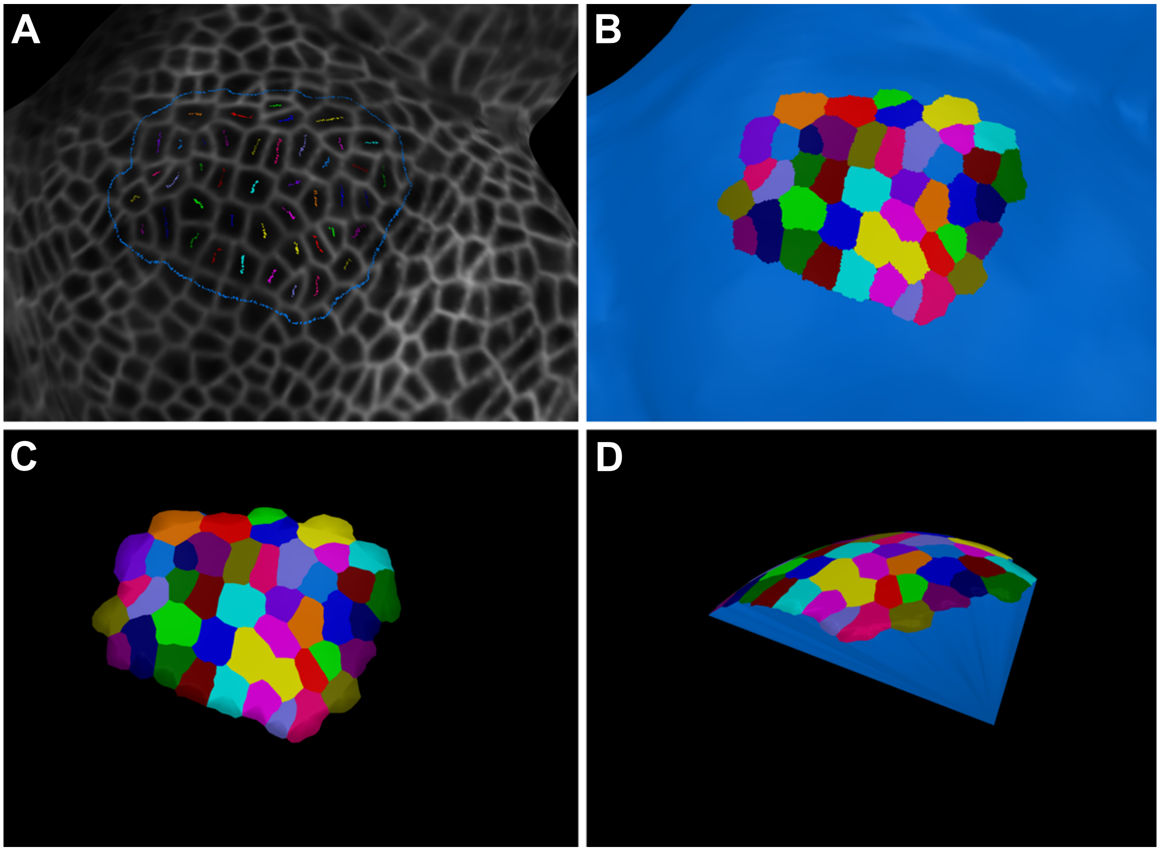

```
Mesh.Subdivide()

Mesh.Smooth_Mesh(3)

Mesh.Subdivide()

Mesh.Smooth_Mesh(1)

Mesh.Subdivide()

Mesh.Subdivide()

Mesh.Project_Signal("No",1,3,0,50000)
```

#### 2.2.11.6 Segmenting

The following procedure was used to detect the edges of the cells in the mesh:

1. At the left side of the window, click the *Add New Seed* tool.
2. Hold hold *Ctrl* and *Alt* and use the mouse to click the interior of a cell.

3. Do this for each cell as seen in Figure 2.3A.
    - Each cell should turn a different color.
    - You can drag the mouse to color a larger portion of the cell interior.
    - This can help if the background noise is high.
    - Each time you click you are drawing with a new cell-seed.
    - If you have already picked the mouse up but want to keep drawing with the same seed, select the *Add Current Seed* tool and draw with that.
    - To revert back to making new seeds, select the *Add New Seed* tool again.
    - To erase a seed:
        (a) Click on the *Label Color* (the colored box at the top of the window). The color should disappear.
        (b) Choose the paint bucket tool.
        (c) Click on the seed that you want to erase.
    - With a new seed, draw a circle around the area you want segmented as seen in Figure 2.3A.
4. In the *Process* tab, expand the *Segmentation* section.
5. Click on *Watershed Segmentation*.
6. Use the default parameters.
7. Click *Go*.
8. Wait for the segmentation to complete.
9. The mesh should look similar to Figure 2.3B.
10. If you are satisfied with the segmentation, proceed to step 13.
11. If there are corners between the cells that are not assigned a color:
    11.1. In the *Process*, *Mesh*, *Cell Mesh* section select *Fix Corners*.
    11.2. Click *Go*.
    11.3. In the *Segmentation* section, choose *Watershed Segmentation*.

    11.4. Click *Go*.

    11.5. The corners should now be fixed.

12. If you are not satisfied with the smoothness of the boundaries:

    12.1. In the *Process*, *Mesh*, *Structure* section select Subdivide Adaptive Near Borders.

    12.2. Map the signal data onto the mesh again using the procedure described previously at step 19 in the section "Building the Mesh".

    12.3. In the *Process*, *Segmentation* section select *Watershed Segmentation*.

    12.4. Use the default parameters.

    12.5. Click *Go*.

13. Expand the *Cell Mesh* section and select *Convert to Cells*.

14. Choose a value of 1$\mu$m for the *Minimum Distance* parameter.

    - This determines the smallest wall segment.
    - Smaller values increase the number of points in the final dataset.
    - Larger values decrease the number of points but may miss small details in the cell boundaries.
    - The mesh should now look similar to 2.3C and 2.3D.

15. Save the cell data.

    15.1. From the top menus, select the *Mesh* dropdown menu.

    15.2. Select *Mesh 1*, then *Export*.

    15.3. Choose *Cells* for the file type.

        - This creates a text file will coordinates of cell boundaries only.
        - The entire mesh data is not included.

    15.4. Click *OK*.

16. Save the mesh.

    16.1. From the top menus, select the *Mesh* dropdown menu.

    16.2. Select *Mesh 1*, then *Save*.

- This creates a .mgxm file.
- All of the mesh data is included.
- This file can be used to re-load the mesh later.

16.3. Click *OK*.

When errors are received while trying to create cells (step 13), there sometimes was a problem with the structure of the mesh. The following Python code was used to try to fix the problem. After running this code, the steps at 13 were used to build the cells again.

```
Mesh.Segment_Mesh(20000)
count = 0
while count < 2:
    try:
        Mesh.Make_Cells(1)
        break
    except:
        Mesh.Fix_Corners()
        Mesh.Smooth_Mesh(1)
        Mesh.Segment_Mesh(20000)
    count += 1
```

At this point the data is exported as a text file (as created in step 15). This file contains the coordinates of all the cell boundaries. This can then be used in the analysis of DR5 expression in the meristem as described in section 2.2.3.

## 2.3 Results

Though we know a lot about the mechanisms of polar auxin transport, we don't fully understand which parts of that system are the most sensitive. Or to put it another way, when perturbed, which parts cause the greatest change in phenotype? To understand this better, I first created computer models to easily tune different parameters. These models led to a number of hypotheses which I then tested.

Figure 2.4: Examples of the graphical output from L-systems. The cells grow over a semi-realistic SAM geometry. Outgrowth of primordia is purely visual and does not affect the functioning of the model in any way.

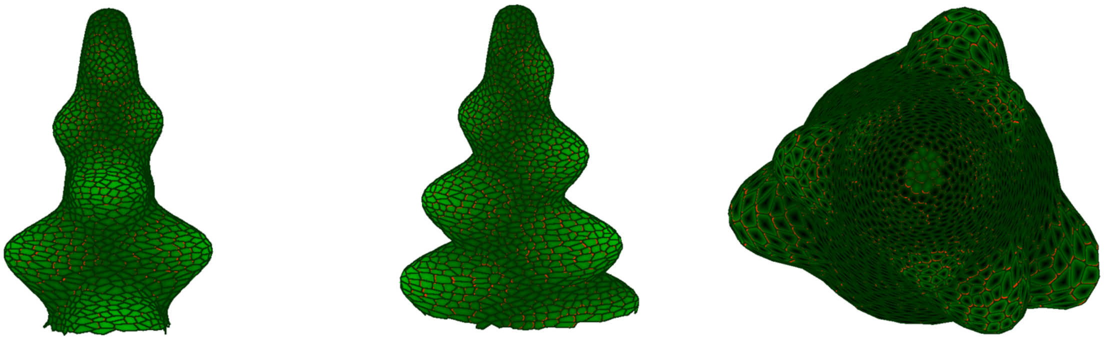

(a) Decussate phyllotaxis (b) Alternate phyllotaxis (c) Spiral phyllotaxis

### 2.3.1 Phyllotaxis Model

Previously, Richard Smith and colleagues created a model of phyllotaxis that incorporated polar auxin transport on a growing mesh of cells that simulate semi-realistic SAM geometry[105]. This model was built in the L-Systems software package in C++ and compiled to run on a Windows operating system. I borrowed this software package and modified the model to incorporate some of the biochemical equations put forth by Jönsson *et al*[107]. This model is capable of generating all of the phyllotaxis patterns commonly observed in plants. Figure 2.4 shows examples of the graphical output. The cells grow and divide over the geometry of a paraboloid. The primordia that grow out from the sides of the paraboloid are only visual and the geometry of the cellular mesh is not actually stretched.

Due to the particular math involved in this model, running it takes a considerable amount of time on a standard laptop. In order to try many different parameter combinations I developed a system for running this software on Amazon's EC2 cloud service. This allows for the model to run on an arbitrary number of computers simultaneously each with a different combination of parameters. My software sends parameters combinations to each model instance and reads the output of each instance, which is composed of a series of divergence angles and plastochron times in text form.

After trying many different values for individual model parameters I found that two of the parameters which effected the phyllotaxis pattern the most were the size of the meristem tissue and the size of the cells. To explore that space more, I tuned both of those parameters, trying each possible pair of values within a certain range, while leaving all other parameters untouched. The results of that experiment are plotted in Figure 2.5.

Figure 2.5

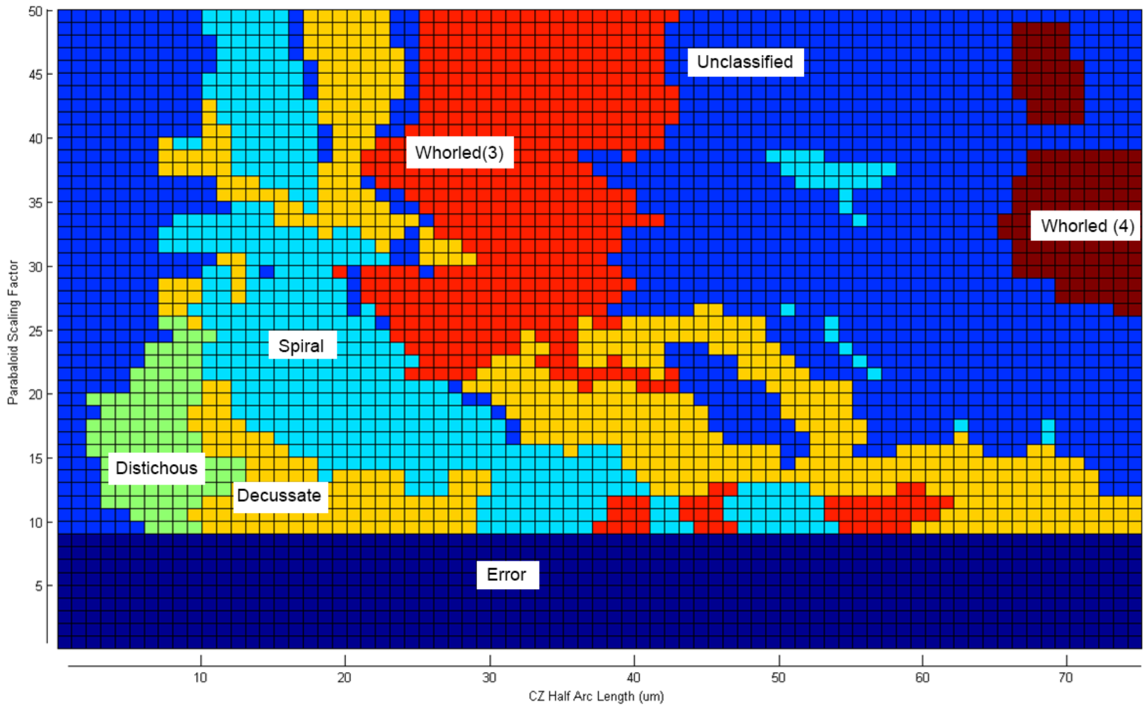

The phyllotaxis patterns were classified into discrete groups (spiral, alternate, etc) which are color coded. It is clear from this plot that the pattern remains steady within particular ranges and then abruptly switches to a different pattern rather than randomly quickly switching between different patterns. This suggests that the model is a multi-stable system with large contiguous parameter spaces that all converge on the same output.

### 2.3.2 Modeling Auxin Movement

In this complex model, cell size appears to play a major part in controlling the phyllotaxis pattern. This could be due to the fact that diffusion within individual cells is not considered (within this particular model). Once a molecule of auxin is transported into a cell it is free to diffuse out of or be transported across any other membrane. *In vivo* diffusion through individual cells definitely occurs but it may have little effect if the rate of other processes (transport across membranes) is slow compared to intracellular diffusion. This means auxin is always well mixed and there is no auxin gradient across a cell. To explore this phenomenon further I created a simple cellular model of auxin diffusion through a single file of rectangular cells implemented in SciPy with functions derived from Cellzilla[116] and Cellerator[117].

In this model passive diffusion across membranes is ignored. Only two factors are considered: transport across membranes between neighbouring cells and diffusion within cells. These factors are modelled using the Cellerator diffusion function $\{X \to X, \mathrm{Diffusion}[f[i,j,k]]\}$ and the Cellzilla transport function $\{X \to X, \mathrm{Transport}[\mathrm{fout}, \mathrm{fin}]\}$. These two functions represent the equations for Fick's law of diffusion

$$J = -D\frac{\partial X}{\partial x} \tag{2.1}$$

and this equation representing facilitated membrane transport

$$\frac{d[X_i]}{dt} = \frac{\ell_k}{A_i}(f_{in}(i,j,k)) - f_{out}(i,j,k) - f_{in}(i,j,k) + f_{out}(i,j,k)) \tag{2.2}$$

Each cell is broken up into many individual elements (finite element method) so that diffusion through the cell can be easily calculated. The transport function is only applied to the elements at the boundaries of the cells.

First, a model was created with 175 cells and was run both with diffusion (2.6A) and without diffusion (2.6B). The model was started with randomized initial auxin concentrations in each cell and ran until a steady state was reached where auxin was no longer transported. As the model runs auxin is transported to the neighbouring cell with the highest auxin concentration. This leads to regions of high and low concentrations of auxin, or "peaks" and "valleys." When the model is run to a steady state condition the peaks turn into single cells containing all of the auxin and valleys containing none. This condition may not actually be encountered *in vivo* but gives a simple method to quantify the number and spacing of peaks: count the cells with greater than zero auxin.

Initially, the parameters of diffusion were intentionally tweaked so that the number of peaks was nearly identical in both the diffusion and diffusion-free models. Then a second model was created with one third as many cells but each cell being three times as wide and having three times as many elements. This model was also run with diffusion (2.6C) and without diffusion (2.6D) using the same diffusion parameters as before.

Then the models were each run 100 times for each condition (400 times total) to determine the average number of "auxin peaks" under each condition. These results show that when intracellular diffusion is considered the spacing of auxin peaks is nearly identical. The auxin peaks accumulate at approximately the same distances apart but with fewer cells in between. When intracellular diffusion is ignored, the spacing of the auxin peaks is dependent on the size of the cells. Auxin peaks

Figure 2.6: Finite Element 1-Dimensional Model of Auxin Transport. **A.** Small cells *with* diffusion. **B.** Small cells *without* diffusion. **C.** Large cells *with* diffusion.**D.** Large cells *without* diffusion.

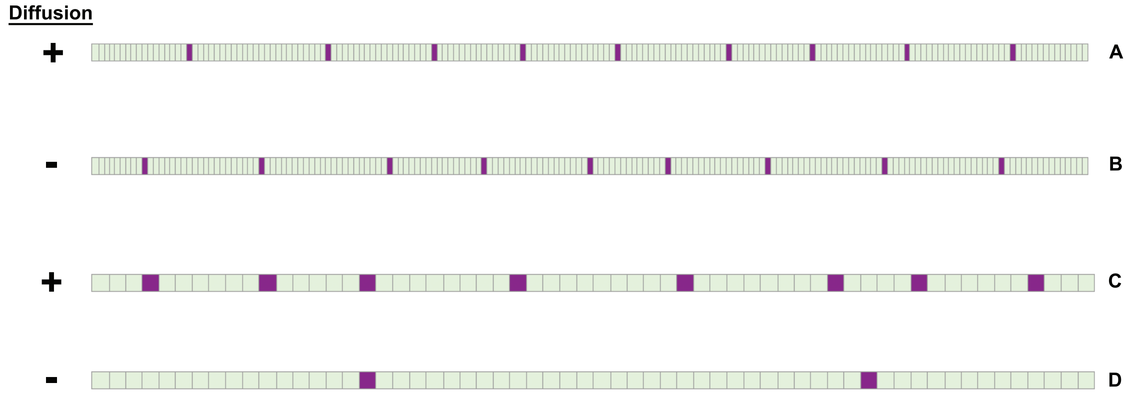

accumulate at different distances apart but with approximately the same number of cells between peaks.

If we assume that *in vivo* intracellular diffusion is rapid compared to intercellular transport then morphological features that result from auxin accumulation should be altered in plants with different sized cells.

### 2.3.3 Shoot Apical Meristem

Auxin accumulates in small regions around the periphery of the meristem at the sites of future organ primordia. The auxin reporter, DR5, is transcribed in high levels in about five to ten cells in each of these regions. Typically these regions form approximately 137 from the last region. Although this tissue is a more complex system than a simple line of rectangular cells, if cell size does play a significant part in controlling the distribution of auxin, the effect should be measurable in mutants with abnormal cell size.

To study the effects that cell size has on auxin distribution in the shoot meristem, auxin transcriptional reporters were added to mutant lines with abnormal cell sizes. The reporter used was pDR5::2xGFP-N7, a nuclear localized GFP that is expressed in areas of high auxin concentration. This reported was transformed into five lines: Ler, Col-0, Wa-1, cycd3;1-3, and msc3. See table 2.1. Transformants were self-crossed to generate homozygous reporter lines. Chosen homozygous reporter lines were picked based on high GFP expression in the roots which is visible under an epifluorescent dissecting microscope.

Table 2.1: Lines Transformed with DR5 Reporter

| **Name** | **Cells** | **Selection** | **Note** |
|---|---|---|---|
| Ler | Wt | Kanamycin | |
| Col-0 | Wt | Kanamycin | |
| Wa-1 | Large | Kanamycin | Tetraploid ecotype |
| cycd3;1-3 | Large | Hygromycin | Triple Cyclin mutant, mixed background |
| msc3 | Small | Kanamycin | Allele of SQN (cyclophilin 40) gene |

Figure 2.7: Comparison of cell sizes in the shoot apical meristem. Two wild type ecotypes and three mutants.

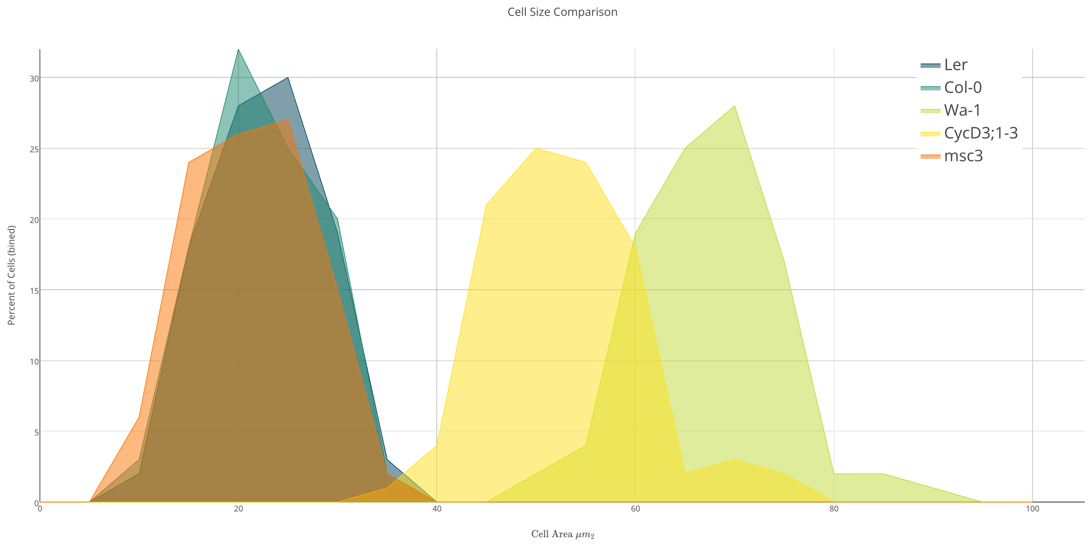

These three mutants were previously reported to have abnormal cell sizes. Wa-1, a tetraploid ecotype, is taller than wild type with a thicker stem, leaves with a larger surface area, and is reported to have larger cells throughout the plant. *cycd3;1-3*, a triple Cyclin mutant, also is taller, thicker, and has broader leaves than wild type, and is reported to have larger cells. *msc3*, an allele of the SQN gene in the Col-0 background, is approximately the same size as Col-0 and has smaller but more numerous cells throughout the plant. To quantify the extent of the cell size abnormalities in the meristem, five meristems from each line were stained with FM4-64 (a fluorescent, lipophilic membrane dye), imaged with laser scanning confocal microscopy, and then processed with MorphoGraphX (see section 2.2.11) to extract the geometry of the cells in the first epidermal layer.

The geometric data extracted from MorphoGraphX were used to calculate the 2-dimensional areas of each cell in each meristem using a custom Python script. The results of this analysis are shown in Figure 2.7. Both wild type lines have approximately the same distribution of cell sizes in the meristem around $20 \mu m^2$. The large cell mutants both have cell areas larger than wild type with

Figure 2.8: DR5 expression in the shoot apical meristem. Processed in MorphoGraphX to only show a projection from the first layer of cells. *Red:* FM4-64. *Green:* pDR5::2xGFP-N7. Scale bar is 20$\mu$m

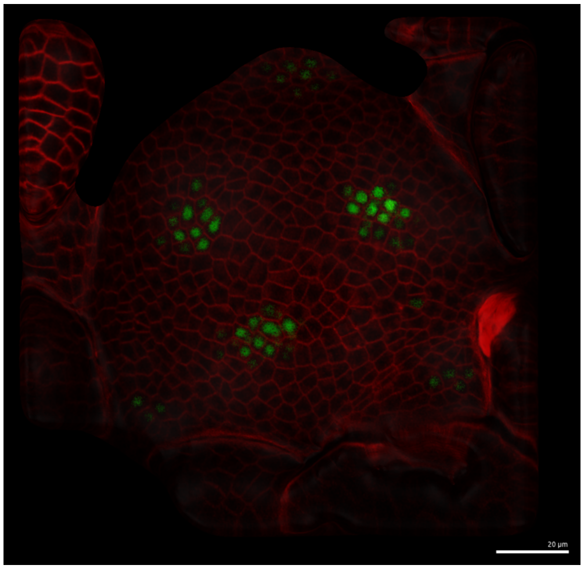

*cycd3;1-3* around $50\mu m^2$ and Wa-1 cells around $70\mu m^2$. *msc3* cells on the other hand were around the same size as wild type cells, around $20\mu m^2$. Further analysis of this line showed that cells in the leaves, roots, and shoot were in fact smaller than wild type as reported.

One possible explanation for this lack of small cells in the SAM is that these cells are already at a minimum size. This lower limit could be set by the size of the nucleus, which could be determined by the size of the chromosomes it contains. In an attempt to lower the minimal cells size in the meristem, the *msc3* line was crossed to *cenh3-1/+ GFP-tailswap/GFP-tailswap*, a line able to induce haploidy[118]. Seeds from this cross either did not germinate or were not haploid, suggesting this particular combination of mutants is embryonic lethal.

To quantify the distribution pattern of auxin in these cell size mutants, the plants were imaged as before this time capturing FM4-64 on one channel and GFP on a second channel as shown in Figure 2.8. The 2-channel images were processed with MorphoGraphX to extract the geometry of the first layer of cells and also classify segmented cells as either DR5 positive or negative, as shown in figure 2.9. This was done for all of the mutants, as shown in figure 2.10.

Using the data extracted with MorphoGraphX, the distances and number of cells between each of the DR5 regions were calculated using a custom Python script. Cells labeled as DR5-positive cells were grouped manually. A centroid (arithmetic mean of points) was calculated using the center of each DR5-positive as an equally weighted point. These centroids were used as the reference points

Figure 2.9: Meristems segmented using MorphGraphX to extract the geometry of the first layer of epidermal cells. *Left:* The segmented cell geometry. *Center:* Cell geometry overlayed with the DR5 signal extracted from the first layer. *Right:* Segmented cells containing DR5 labelled to differentiate them from non-DR5 expressing cells.

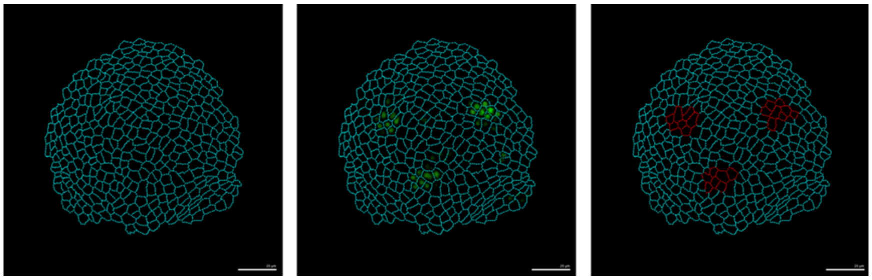

Figure 2.10: Three DR5 Meristem Comparison

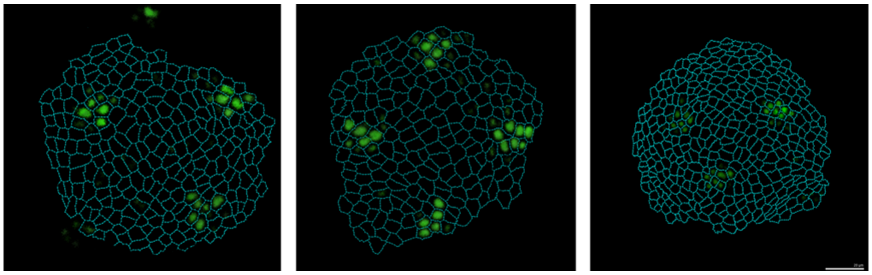

when calculating distances and number of cells. The results of these measurements are shown in figure 2.11.

The difference between wild type and *msc3* and large cell mutants is clear when looking at absolute distances between DR5 regions. The DR5 regions are almost twice as far apart in the large cell mutants compared to wild type and *msc3*. But the difference is not so clear when looking at number of cells in between regions as the error in the measurements is relatively large. This could be due to the method in which the measurement was made. To make that measurement, any cell crossed by the shortest line between regions is counted, even if the line crossed only a small corner of the cell. Also, some regions of the meristem are dividing faster than other, as shown in the first chapter. If the line happens to cross through a region undergoing rapid division then more cells would be counted. Or it is possible that there really is a lot of variability between plants of the same line, or even the same meristem at different points in time. Capturing such variability using snapshots of a highly dynamic process is error prone and increasing the sample size may not yield any more interesting results without a fundamental change to the experiment. One such experiment could be live imaging many plants and quantifying how the number of cells between DR5 regions changes every couple of hours.

Figure 2.11: Distances between regions of DR5 expression in the SAM. **A:** Mean number of cells between regions of DR5 expression. **B:** Mean distance between regions of DR5 expression.

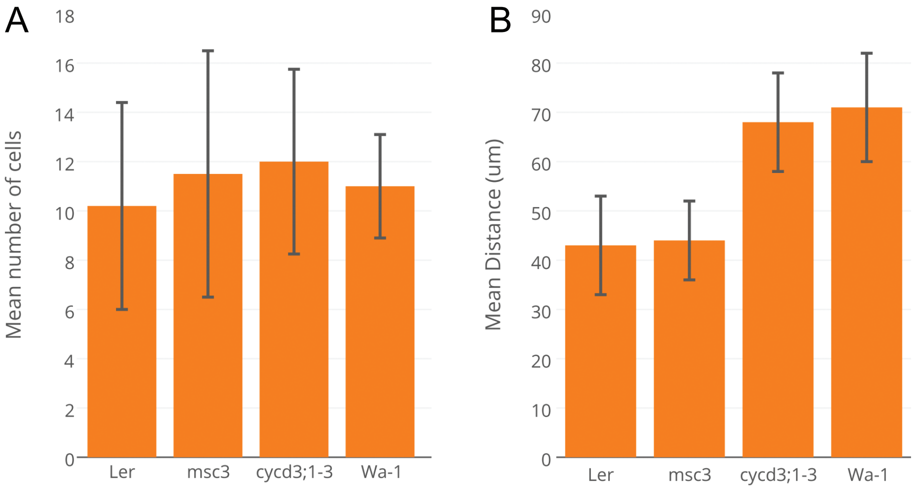

### 2.3.4 Shoots

During early shoot development it is thought that auxin is transported around the base of the vascular ring. In areas where auxin accumulates a vascular bundle is formed. If this is true then vascular development might be under the control of the same mechanisms at play in the meristem and the cell size dependent phenomenon shown in the model might be relevant.

To test this I looked at cross sections of shoots in wild type and cell size mutants to see if there was a correlation between number of cells and number of bundles. Tissue samples of mature plants were taken, fixed in formaldehyde, embedded in paraffin, sectioned, stained with Toluidine Blue O (to increase the contrast of the cells in the vasculature), mounted, and imaged. In the images I manually counted the number of bundles in each sample as seen in figure 2.12A. Additionally I used image processing techniques to assist in the counting of the cells at the base of the vascular ring, as seen in figure 2.12B.

The results of this study shown in figure 2.13 indicate that there is a linear relationship between the number of cells in the vascular ring and the number of bundles in adult shoot tissue. In general, more cells lead to more vascular bundles. Although, it is interesting to note that Wa-1 and *cycd3;1-3*

Figure 2.12: Paraffin embedded sections of the shoot showing vascular bundles stained with Toluidine Blue O. *A:* msc3 shoot showing 9 vascular bundles. *B:* Cells at the base of the vascular ring are counted.

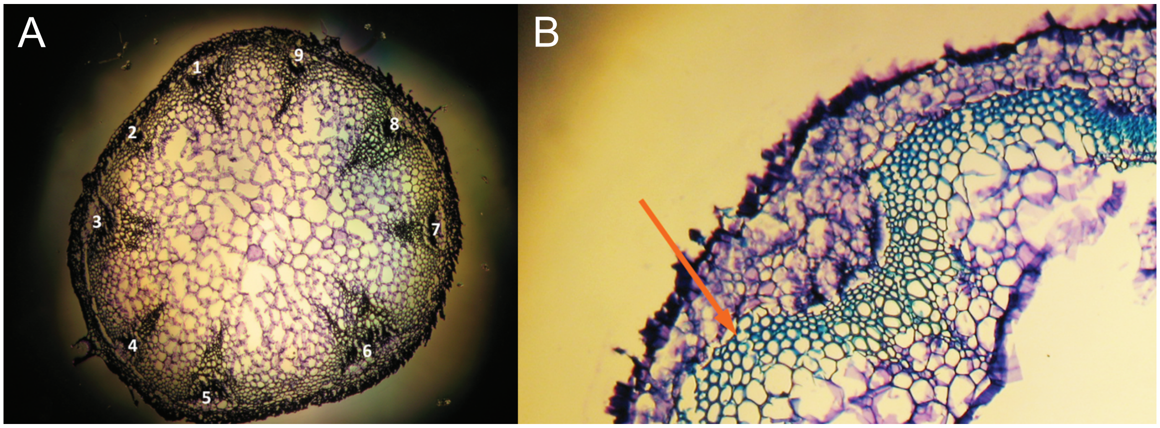

did not have the fewest number of cells, which is what would be assumed if the cells were larger and the shoot was the same size compared to wild type. In these mutants which have more cells than wild type, the vascular cells are in fact larger but the shoot is also larger, which more than makes up for the larger cells. Despite this observation, the more cells more bundles relationship holds up.

### 2.3.5 Roots

In the roots of Arabidopsis, lateral roots develop in an alternating pattern out of the sides of the primary root, usually on the outside edge of a curve. To test if the transport-limited model is at play in this case, large and small cell mutants with the pDR5::2xGFP-N7 reporter were observed. The plants were grown on MS agar and individual plants were removed and imaged at one, three and ten days after germination. These plants were stained with FM4-64 to label the cell membranes and then observed with laser scanning confocal microscopy.

Initially the goal was to find the areas of DR5 expression along the root and using image processing techniques measure the distance and number of cells between these areas. But the images showed that the expression of DR5 in the roots of cell size mutants, particularly the large cell mutants *cycd3;1-3* and Wa-1, was disorganized compared to wild type. In Wa-1 at one day after germination, as shown in Figure 2.14A, there is a repeating DR5 pattern similar to wildtype (pairs of DR5 expressing cells periodically up the root with increasing space in between higher on the root) but with rapidly decreasing intensity as the expressing cells are pushed further from the meristem.

Figure 2.13: Relationship between number of vascular bundles in the shoot and the number of cells around the base of the vascular ring.

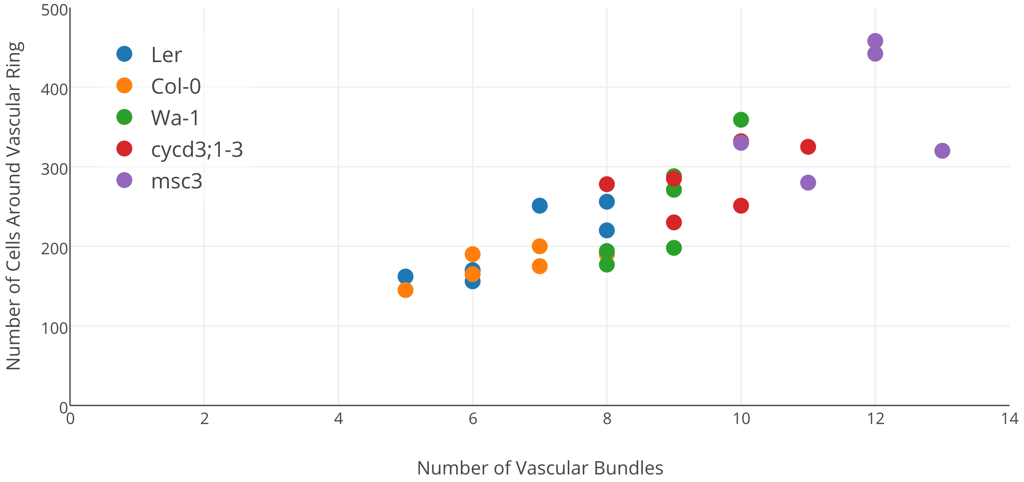

Three days after germination (Figure 2.14B) the pairs of DR5 expressing cells above the meristem have turned into a mass of seeming randomly arranged DR5 expressing cells with a single file of DR5 expressing cells progressing basally away from the meristem. By ten days after germination (Figure 2.14C) the root has enlarged, the meristem has become completely disorganized with DR5 expressing cells scattered throughout, and no DR5 expression basal to the meristem. But despite this breakdown in auxin signalling, or at least in the expression of one particular auxin-sensitive promoter, the plant still makes wild type looking lateral roots at the sites of curvature.

Given that auxin is a critical component in our model, it is difficult to imagine how the transport limited model could be accurate in the root given the disorganization displayed by the auxin reporter.

### 2.3.6 Leaves

During leaf formation, auxin is transported around the periphery of the leaf primordium. Leaf serrations or teeth develop in the areas of high auxin accumulation. Although this is a highly dynamic system like the SAM, one could image the ring of cells along the perimeter being stretched out into a straight line like the simple linear model described earlier. If the assertion that the cells are well mixed (or at least sufficiently mixed given the rate of intercellular transport) is true then

Figure 2.14: Progression of the DR5 expression pattern in Wa-1 root tips. *A:* One day after germination. *B:* Three days after germination. *C:* Ten days after germination.

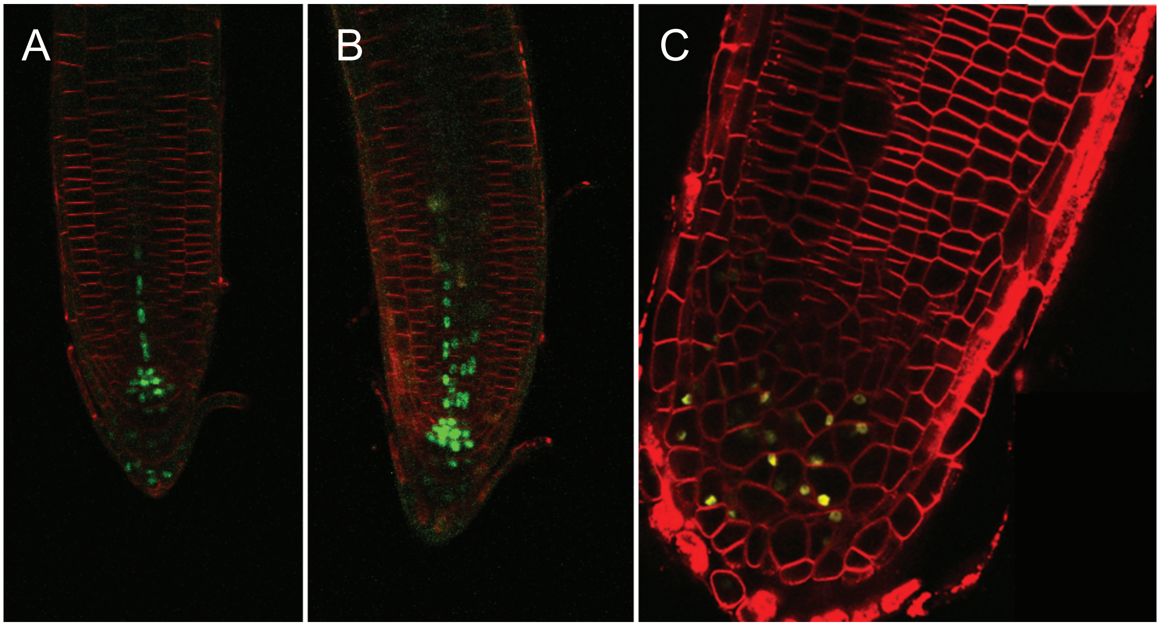

we should expect the spacing of the leaf serrations to be dependent on cell size. Plants with larger cells but the same size leaf as wild type should have fewer teeth. The cell size mutants considered here do in fact have similar size leafs to wild type even though their cells are different sizes.

To quantify this phenomenon 100 leaves were collected from each line, two per plant. The leaves were flattened and the side of the leaf with the most well defined teeth was chosen and the teeth were counted on that side, as shown in figure 2.15. The results from these observations (Figure 2.16) show that the large cell mutants have fewer teeth than wild type while the small cell mutant has more teeth than wild type on average, though, the magnitude of the effect is not as large as one might expect. The cells in Wa-1 and *cycd3;1-3* are at least twice as large as wild type but only have about 25% fewer teeth. Likewise, *msc3* mutants only have about 25% more teeth than wild type.

Given that the cells in Wa-1 and *cycd3;1-3* have approximately twice the diameter and four times the area of wild type cells, one might expect Wa-1 and *cycd3;1-3* leaves to have half as many serrations. So the linear model auxin-gradient-free model does not fully explain this phenomenon.

Figure 2.15: Rosette leaves from wild type and cell size mutant plants. Serrations are counted along one side of a leaf. *A:* Col-0. *B:* CycD3;1-3. *C:* Wa-1. *D:* msc3.

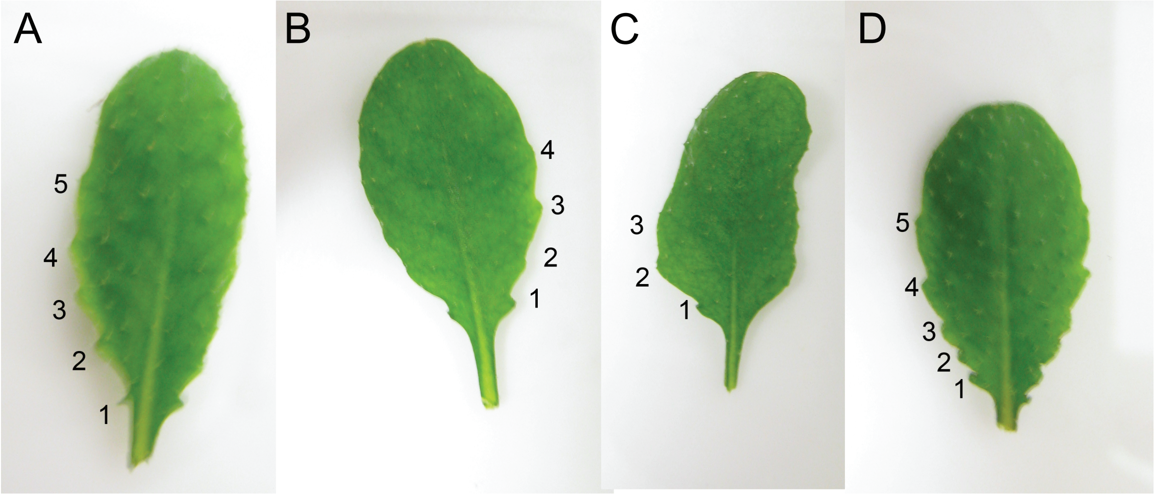

Figure 2.16: Mean number of teeth per rosette leaf. Sample size was 100 leaves per line. Teeth counted on one side of leaf.

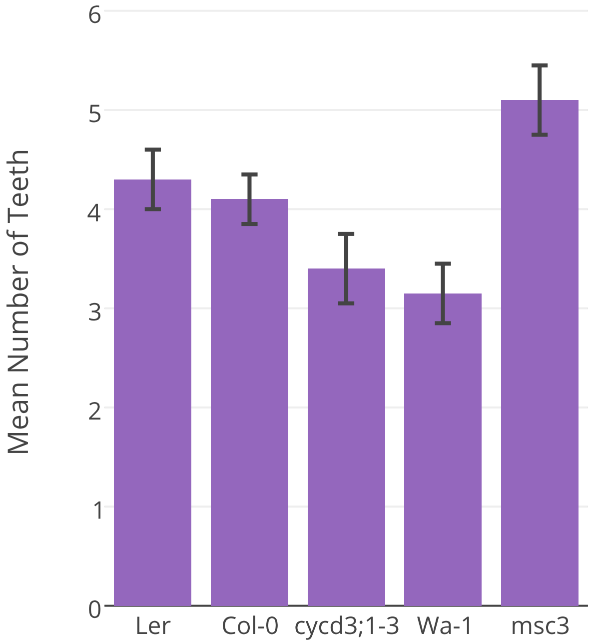

## 2.4 Discussion

Previous work in this field has determined that auxin accumulation is often responsible for organ formation and tissue differentiation. In areas of the plant where auxin accumulates cells expand and divide rapid and differentiate. It has been shown that polar auxin transporters play a key role in the distribution of auxin and therefore control morphogenesis. Currently there are two competing explanations for how these polar auxin transports chose the direction to pump auxin. One is that (through an unknown mechanism) the PIN protein are localized to the membrane adjacent to the neighboring cell with the highest auxin concentration and pump auxin towards that cell. The other is that PIN proteins localize to the side of the cell which is transporting the most auxin and transport more auxin, leading to a positive feedback loop. But given all that is known about this system, none of this explains how the spacing between auxin maxima is determined or controlled.

Here I have shown that cell size is a critical factor in controlling the accumulation of auxin in certain parts of the plant. The model predicts that when transport across the membrane is the rate limiting step, auxin accumulates in regions separated by a consistent number of cells rather than a consistent distance. I tested this by looking at auxin and organ spacing in mutants with different cell diameters. If the model is to be believed then organs should have larger spaces between them in plants with larger cells and smaller spaces in plants with smaller cells.

In the shoot apical meristem, at least during its reproductive phase, the spacing of the floral primordia is affected by the size of the cells. The absolute distance between primordia as measured along the surface of the meristem is about 75% greater in large cell mutants compared to both wild type and *msc3*, which has the same sized cells as wild type in the SAM. When looking at the number of cells between primordia, the average number of cells is approximately the same in all mutants, which supports the model's predictions. But the variability in those particular measurements is great enough that it is possible that there really is a difference in cell numbers between large cell mutants and wild type and the difference is just hidden in the noise.

The amount of variability may be an artifact of the particular measurement used. To measure the number of cells between primordia, a line was created in software between the centers of the primordia being measured. This line followed the curvature of the meristem surface and intersected with cell boundaries. The number of intersections $n$ were counted to determine the number of cells in between the primordia, $n + 1$. Sometimes the line would pass through a very small section of the corner of a cell, which would not contribute much to the distance but would increase the cell count by one. Considering the small number of cells between sequential primordia, adding an extra cell or two could increase the cell count by a relatively large amount. A different algorithm for measuring cell numbers might lead to results with smaller error bars.

In the shoot tissue, the spacing of the vascular bundles also seems to be affected by cell size. It is thought that during early development auxin is transported around a ring of cells in the shoot. In areas where auxin accumulates the tissue differentiates and forms vascular bundles. I have shown that in large and small cell mutants the number of vascular bundles is tightly correlated with the number of cells in the vascular ring. However, in this study the shoot tissue was observed long after the vascular bundles had formed and the size of the cells in the mature tissue probably had no influence on vascular structure. It is possible that during the developmental stage where auxin distribution affected vascular bundle formation the cells in the mutants were also of larger or smaller size, which would support the model.

Previous work has shown that in early leaf primorida, auxin accumulates in areas around the periphery of the leaf [119]. In these areas of high auxin concentration, serrations are formed. If we assume that auxin transport is behaving similar to the model and that the leaves in cell size mutants have the same circumference as wild type then we would expect the number of serrations to vary in proportion to the cell size. The size of leaves in cell size mutants turns out to not be exactly the same as wild type but is similar enough to make a comparison. I observed large cell mutants to have fewer serrations than wild type and the small cell mutant to have more serrations than wild type. The proportions are not exactly what is expected given the magnitude in change of cell size but this could be due to differences in leaf primordia size between the mutants. For example, in large cell mutants a fewer-serrations phenotype due to larger cells could be masked by a larger primordia, which would increase the number of cells and therefore the number of serrations. Nevertheless the direction of change is in agreement with the model suggesting that auxin movement in the leaf is transport limited rather than diffusion limited.

In roots, auxin is thought to play a role in meristem maintenance and also in the formation of lateral roots. If the positioning of the lateral roots is determined by transport-limited auxin movement rather than diffusion-limited movement (or some other mechanism) then large and small cell mutants should show differences in spacing between lateral roots. In this study I observed that auxin distribution, or at least the expression of DR5 (which should be an accurate proxy for auxin distribution), basal of the meristem is disorganized in large and small cell mutants. Yet those plants make a typical number of lateral roots that appear to be phenotypically normal.

One possible explanation for this observation is that auxin distribution is normal in these mutants while DR5 expression is altered and is not acting as a proxy for auxin concentration due to some interference in the upstream auxin signalling pathway. I find this explanation to be unlikely as DR5 expression is normal throughout other parts of the plant in cell size mutants. It is possible that the roots have a slightly different auxin signalling pathway than the above-ground tissue that is particularly sensitive to some difference in the cell size mutants. Additionally, if auxin signalling was actually interrupted in the roots, one would expect other parts of the roots to have phenotypic abnormalities which were not observed.

Another possible explanation is that auxin is not necessary for the patterning of lateral roots. It has been shown that auxin accumulates at bends in the root where a lateral root primordia eventually forms. It has also been shown that auxin is critical to the formation of lateral roots as this tissue is malformed in auxin synthesis mutants. Taking these observations as fact, it is still possible for auxin to not be necessary for the positioning of the lateral roots. For example, the accumulation of auxin at the future sites of lateral roots primordia may be coincidental rather than directly upstream of primordia formation like in the shoot meristem. One could imagine a mechanism (X) that causes both auxin accumulation (Y) and lateral root formation in the same location (Z). In this hypothetical scenario X could cause Y and Z ($X \to Y, X \to Z$) but Y may not be responsible for causing Z ($X \to Y \to Z$). In this scenario the cell size mutants could interfere with auxin distribution without the need for an alternative signalling pathway and still have normal lateral root formation in both the positioning of the primordia and the development of primordia into mature roots.

Overall, the auxin transport limited model is substantiated by observations in the shoot apical meristem, shoot vasculature, and to some extent in the leaves. It is not supported by observations of the root. It is possible that auxin distribution is controlled by two different mechanisms above and below ground, or that a single mechanism (different than the one described) is responsible for all tissue and the observations supporting the model were coincidental. Nevertheless, further experiments will be needed to fully understand the relationship between cell size and auxin distribution.

# References

[1] Charles Darwin and Francis Darwin. *The Power of Movement in Plants.* London: John Murray Publishers, 1880.

[2] Fritz Kogl and Arie Jan Haagen-Smit. “Mitteilung uber pflanzliche wachstumsstoffe. Uber die vhemie des euchsstoffs”. In: *Proc. K. Ned. Akad. Wet* 34 (1931), pp. 1411–1416.

[3] I. Casimiro. “Auxin Transport Promotes Arabidopsis Lateral Root Initiation”. In: *The Plant Cell* 13.4 (Apr. 2001), pp. 843–852. ISSN: 10404651.

[4] I Barlier et al. “The SUR2 gene of Arabidopsis thaliana encodes the cytochrome P450 CYP83B1, a modulator of auxin homeostasis.” In: *Proceedings of the National Academy of Sciences of the United States of America* 97.26 (Dec. 2000), pp. 14819–24. ISSN: 0027-8424.

[5] J Normanly, J D Cohen, and G R Fink. “Arabidopsis thaliana auxotrophs reveal a tryptophan-independent biosynthetic pathway for indole-3-acetic acid.” In: *Proceedings of the National Academy of Sciences of the United States of America* 90.21 (Nov. 1993), pp. 10355–9. ISSN: 0027-8424.

[6] J Ouyang, X Shao, and J Li. “Indole-3-glycerol phosphate, a branchpoint of indole-3-acetic acid biosynthesis from the tryptophan biosynthetic pathway in Arabidopsis thaliana.” In: *The Plant Journal* 24.3 (Nov. 2000), pp. 327–33. ISSN: 0960-7412.

[7] Andrew W Woodward and Bonnie Bartel. “Auxin: regulation, action, and interaction.” In: *Annals of Botany* 95.5 (Apr. 2005), pp. 707–35. ISSN: 0305-7364.

[8] Yunde Zhao et al. “Trp-dependent auxin biosynthesis in Arabidopsis: involvement of cytochrome P450s CYP79B2 and CYP79B3.” In: *Genes & Development* 16.23 (Dec. 2002), pp. 3100–12. ISSN: 0890-9369.

[9] S Bak et al. “CYP83B1, a cytochrome P450 at the metabolic branch point in auxin and indole glucosinolate biosynthesis in Arabidopsis.” In: *The Plant Cell* 13.1 (Jan. 2001), pp. 101–11. ISSN: 1040-4651.

[10] Michael Dalgaard Mikkelsen, Peter Naur, and Barbara Ann Halkier. “Arabidopsis mutants in the C-S lyase of glucosinolate biosynthesis establish a critical role for indole-3-acetaldoxime in auxin homeostasis”. In: *The Plant Journal* 37.5 (Mar. 2004), pp. 770–777. ISSN: 0960-7412.

[11] J Normanly et al. “Arabidopsis mutants resistant to the auxin effects of indole-3-acetonitrile are defective in the nitrilase encoded by the NIT1 gene.” In: *The Plant Cell* 9.10 (Oct. 1997), pp. 1781–90. ISSN: 1040-4651.

[12] Satoko Sugawara et al. “Biochemical analyses of indole-3-acetaldoxime-dependent auxin biosynthesis in Arabidopsis.” In: *Proceedings of the National Academy of Sciences of the United States of America* 106.13 (Mar. 2009), pp. 5430–5. ISSN: 1091-6490.

[13] Anna N Stepanova et al. “TAA1 mediated auxin biosynthesis is essential for hormone crosstalk and plant development.” In: *Cell* 133.1 (May 2008), pp. 177–91. ISSN: 1097-4172.

[14] Yi Tao et al. “Rapid synthesis of auxin via a new tryptophan-dependent pathway is required for shade avoidance in plants.” In: *Cell* 133.1 (Apr. 2008), pp. 164–76. ISSN: 1097-4172.

[15] Kiyoshi Mashiguchi et al. “The main auxin biosynthesis pathway in Arabidopsis.” In: *Proceedings of the National Academy of Sciences* 108.45 (Nov. 2011), pp. 18512–7. ISSN: 1091-6490.

[16] Christina Won et al. “Conversion of tryptophan to indole-3-acetic acid by TRYPTOPHAN AMINOTRANSFERASES OF ARABIDOPSIS and YUCCAs in Arabidopsis.” In: *Proceedings of the National Academy of Sciences of the United States of America* 108.45 (Dec. 2011), pp. 18518–23. ISSN: 1091-6490.

[17] Y Zhao et al. “A role for flavin monooxygenase-like enzymes in auxin biosynthesis.” In: *Science* 291.5502 (Jan. 2001), pp. 306–9. ISSN: 0036-8075.

[18] Youfa Cheng, Xinhua Dai, and Yunde Zhao. “Auxin synthesized by the YUCCA flavin monooxygenases is essential for embryogenesis and leaf formation in Arabidopsis.” In: *The Plant Cell* 19.8 (Aug. 2007), pp. 2430–9. ISSN: 1040-4651.

[19] Xinhua Dai et al. “The biochemical mechanism of auxin biosynthesis by an arabidopsis YUCCA flavin-containing monooxygenase.” In: *The Journal of biological chemistry* 288.3 (Jan. 2013), pp. 1448–57. ISSN: 1083-351X.

[20] Patricia Hornitschek et al. “Phytochrome interacting factors 4 and 5 control seedling growth in changing light conditions by directly controlling auxin signaling.” In: *The Plant Journal* 71.5 (Sept. 2012), pp. 699–711. ISSN: 1365-313X.

[21] Lin Li et al. “Linking photoreceptor excitation to changes in plant architecture.” In: *Genes & Development* 26.8 (Apr. 2012), pp. 785–90. ISSN: 1549-5477.

[22] Jiaqiang Sun et al. “PIF4-mediated activation of YUCCA8 expression integrates temperature into the auxin pathway in regulating arabidopsis hypocotyl growth.” In: *PLoS genetics* 8.3 (Jan. 2012). Ed. by Li-Jia Qu, e1002594. ISSN: 1553-7404.

[23] D Magnus Eklund et al. “The Arabidopsis thaliana STYLISH1 protein acts as a transcriptional activator regulating auxin biosynthesis.” In: *The Plant Cell* 22.2 (Feb. 2010), pp. 349–63. ISSN: 1532-298X.

[24] L Galweiler et al. “Regulation of polar auxin transport by AtPIN1 in Arabidopsis vascular tissue.” In: *Science* 282.5397 (1998), p. 30. ISSN: 0036-8075.

[25] Misuk Cho, Sang Ho Lee, and Hyung-Taeg Cho. “P-glycoprotein4 displays auxin efflux transporter-like action in Arabidopsis root hair cells and tobacco cells.” In: *The Plant Cell* 19.12 (Dec. 2007), pp. 3930–43. ISSN: 1040-4651.

[26] Markus Geisler et al. “Cellular efflux of auxin catalyzed by the Arabidopsis MDR/PGP transporter AtPGP1.” In: *The Plant Journal* 44.2 (Oct. 2005), pp. 179–94. ISSN: 0960-7412.

[27] Kamil Ruzicka et al. “Arabidopsis PIS1 encodes the ABCG37 transporter of auxinic compounds including the auxin precursor indole-3-butyric acid.” In: *Proceedings of the National Academy of Sciences of the United States of America* 107.23 (June 2010), pp. 10749–53. ISSN: 1091-6490.

[28] M J Bennett et al. “Arabidopsis AUX1 gene: a permease-like regulator of root gravitropism.” In: *Science* 273.5277 (Aug. 1996), pp. 948–50. ISSN: 0036-8075.

[29] R Swarup et al. “Localization of the auxin permease AUX1 suggests two functionally distinct hormone transport pathways operate in the Arabidopsis root apex.” In: *Genes & Development* 15.20 (Oct. 2001), pp. 2648–53. ISSN: 0890-9369.

[30] Jan Petrásek et al. “PIN proteins perform a rate-limiting function in cellular auxin efflux.” In: *Science* 312.5775 (May 2006), pp. 914–8. ISSN: 1095-9203.

[31] Justyna Wisniewska et al. “Polar PIN Localization Directs Auxin Flow in Plants”. In: *Science* 312.May (2006), p. 2006.

[32] Pankaj Dhonukshe et al. “Auxin transport inhibitors impair vesicle motility and actin cytoskeleton dynamics in diverse eukaryotes.” In: *Proceedings of the National Academy of Sciences of the United States of America* 105.11 (Mar. 2008), pp. 4489–94. ISSN: 1091-6490.

[33] Jürgen Kleine-Vehn et al. “Recycling, clustering, and endocytosis jointly maintain PIN auxin carrier polarity at the plasma membrane.” In: *Molecular Systems Biology* 7 (Jan. 2011), p. 540. ISSN: 1744-4292.

[34] Jozef Mravec et al. “Cell plate restricted association of DRP1A and PIN proteins is required for cell polarity establishment in Arabidopsis.” In: *Current Biology* 21.12 (June 2011), pp. 1055–60. ISSN: 1879-0445.

[35] Jing Zhang et al. “Inositol trisphosphate-induced Ca2+ signaling modulates auxin transport and PIN polarity.” In: *Developmental Cell* 20.6 (June 2011), pp. 855–66. ISSN: 1878-1551.

[36] Pankaj Dhonukshe et al. “Generation of cell polarity in plants links endocytosis, auxin distribution and cell fate decisions.” In: *Nature* 456.7224 (Dec. 2008), pp. 962–6. ISSN: 1476-4687.

[37] Niko Geldner et al. “The Arabidopsis GNOM ARF-GEF mediates endosomal recycling, auxin transport, and auxin-dependent plant growth.” In: *Cell* 112.2 (2003), p. 30. ISSN: 0092-8674.

[38] Jürgen Kleine-Vehn et al. “PIN auxin efflux carrier polarity is regulated by PINOID kinase-mediated recruitment into GNOM-independent trafficking in Arabidopsis.” In: *The Plant Cell* 21.12 (Dec. 2009), pp. 3839–49. ISSN: 1532-298X.

[39] Marta Michniewicz et al. “Antagonistic regulation of PIN phosphorylation by PP2A and PINOID directs auxin flux.” In: *Cell* 130.6 (Sept. 2007), pp. 1044–56. ISSN: 0092-8674.

[40] Lindy Abas et al. “Intracellular trafficking and proteolysis of the Arabidopsis auxin-efflux facilitator PIN2 are involved in root gravitropism.” In: *Nature Cell Biology* 8.3 (Mar. 2006), pp. 249–56. ISSN: 1465-7392.

[41] Yvon Jaillais et al. “AtSNX1 defines an endosome for auxin-carrier trafficking in Arabidopsis.” In: *Nature* 443.7107 (Sept. 2006), pp. 106–9. ISSN: 1476-4687.

[42] Yvon Jaillais et al. “The retromer protein VPS29 links cell polarity and organ initiation in plants.” In: *Cell* 130.6 (Sept. 2007), pp. 1057–70. ISSN: 0092-8674.

[43] Tomasz Paciorek et al. “Auxin inhibits endocytosis and promotes its own efflux from cells.” In: *Nature* 435.7046 (June 2005), pp. 1251–6. ISSN: 1476-4687.

[44] Stéphanie Robert et al. “ABP1 Mediates Auxin Inhibition of Clathrin-Dependent Endocytosis in Arabidopsis”. In: *Cell* 143.1 (Oct. 2010), pp. 111–121. ISSN: 00928674.

[45] Youfa Cheng et al. “NPY1, a BTB-NPH3-like protein, plays a critical role in auxin-regulated organogenesis in Arabidopsis.” In: *Proceedings of the National Academy of Sciences of the United States of America* 104.47 (Nov. 2007), pp. 18825–9. ISSN: 1091-6490.

[46] Masahiko Furutani et al. “The gene MACCHI-BOU 4/ENHANCER OF PINOID encodes a NPH3-like protein and reveals similarities between organogenesis and phototropism at the molecular level.” In: *Development* 134.21 (Nov. 2007), pp. 3849–59. ISSN: 0950-1991.

[47] Masahiko Furutani et al. “Polar-localized NPH3-like proteins regulate polarity and endocytosis of PIN-FORMED auxin efflux carriers.” In: *Development* 138.10 (May 2011), pp. 2069–78. ISSN: 1477-9129.

[48] Yuanting Li et al. “NPY genes play an essential role in root gravitropic responses in Arabidopsis.” In: *Molecular Plant* 4.1 (Jan. 2011), pp. 171–9. ISSN: 1752-9867.

[49] Johannes Leitner et al. "Lysine63-linked ubiquitylation of PIN2 auxin carrier protein governs hormonally controlled adaptation of Arabidopsis root growth." In: *Proceedings of the National Academy of Sciences of the United States of America* 109.21 (May 2012), pp. 8322–7. ISSN: 1091-6490.

[50] Marie Barberon et al. "Monoubiquitin-dependent endocytosis of the iron-regulated transporter 1 (IRT1) transporter controls iron uptake in plants." In: *Proceedings of the National Academy of Sciences of the United States of America* 108.32 (Aug. 2011), E450–8. ISSN: 1091-6490.

[51] P Green. "Phyllotactic Patterns: A Biophysical Mechanism for their Origin". In: *Annals of Botany* 77.5 (May 1996), pp. 515–528. ISSN: 03057364.

[52] D'Arcy Wentworth Thompson. *On Growth and Form.* Cambridge, UK: Cambridge University Press, 1942.

[53] Olivier Hamant et al. "Developmental patterning by mechanical signals in Arabidopsis." In: *Science* 322.5908 (Dec. 2008), pp. 1650–5. ISSN: 1095-9203.

[54] Naomi Nakayama et al. "Mechanical regulation of auxin-mediated growth." In: *Current biology : CB* 22.16 (Aug. 2012), pp. 1468–76. ISSN: 1879-0445.

[55] Heidi Szemenyei, Mike Hannon, and Jeff A Long. "TOPLESS mediates auxin-dependent transcriptional repression during Arabidopsis embryogenesis." In: *Science* 319.5868 (Mar. 2008), pp. 1384–6. ISSN: 1095-9203.

[56] T Ulmasov et al. "Aux/IAA proteins repress expression of reporter genes containing natural and highly active synthetic auxin response elements." In: *The Plant cell* 9.11 (Nov. 1997), pp. 1963–71. ISSN: 1040-4651.

[57] Nihal Dharmasiri, Sunethra Dharmasiri, and Mark Estelle. "The F-box protein TIR1 is an auxin receptor." In: *Nature* 435.7041 (May 2005), pp. 441–5. ISSN: 1476-4687.

[58] Stefan Kepinski and Ottoline Leyser. "The Arabidopsis F-box protein TIR1 is an auxin receptor." In: *Nature* 435.7041 (May 2005), pp. 446–51. ISSN: 1476-4687.

[59] Luz Irina A Calderón Villalobos et al. "A combinatorial TIR1/AFB-Aux/IAA co-receptor system for differential sensing of auxin." In: *Nature chemical biology* 8.5 (May 2012), pp. 477–85. ISSN: 1552-4469.

[60] W M Gray et al. "Auxin regulates SCF(TIR1)-dependent degradation of AUX/IAA proteins." In: *Nature* 414.6861 (Nov. 2001), pp. 271–6. ISSN: 0028-0836.

[61] Teva Vernoux et al. “The auxin signalling network translates dynamic input into robust patterning at the shoot apex.” In: *Molecular Systems Biology* 7 (Jan. 2011), p. 508. ISSN: 1744-4292.

[62] Géraldine Brunoud et al. “A novel sensor to map auxin response and distribution at high spatio-temporal resolution.” In: *Nature* 482.7383 (Feb. 2012), pp. 103–6. ISSN: 1476-4687.

[63] R Hertel, K S Thomson, and V E Russo. “In vitro auxin binding toparticulate cell fractions from corn coleoptiles.” In: *Planta* 107.4 (Dec. 1972), pp. 325–40. ISSN: 0032-0935.

[64] A M Jones. “Auxin-Dependent Cell Expansion Mediated by Overexpressed Auxin-Binding Protein 1”. In: *Science* 282.5391 (Nov. 1998), pp. 1114–1117.

[65] J G Chen et al. “ABP1 is required for organized cell elongation and division in Arabidopsis embryogenesis.” In: *Genes & Development* 15.7 (Apr. 2001), pp. 902–11. ISSN: 0890-9369.

[66] Nils Braun et al. “Conditional repression of AUXIN BINDING PROTEIN1 reveals that it coordinates cell division and cell expansion during postembryonic shoot development in Arabidopsis and tobacco.” In: *The Plant cell* 20.10 (2008), pp. 2746–62. ISSN: 1040-4651.

[67] Karine M David et al. “The auxin-binding protein 1 is essential for the control of cell cycle.” In: *The Plant Journal* 50.2 (Apr. 2007), pp. 197–206. ISSN: 0960-7412.

[68] Alexandre Tromas et al. “The AUXIN BINDING PROTEIN 1 is required for differential auxin responses mediating root growth.” In: *PloS ONE* 4.9 (Jan. 2009). Ed. by Edward Newbigin, e6648. ISSN: 1932-6203.

[69] Tongda Xu et al. “Cell surface- and rho GTPase-based auxin signaling controls cellular interdigitation in Arabidopsis.” In: *Cell* 143.1 (Oct. 2010), pp. 99–110. ISSN: 1097-4172.

[70] Yunus Effendi et al. “The heterozygous abp1/ABP1 insertional mutant has defects in functions requiring polar auxin transport and in regulation of early auxin-regulated genes.” In: *The Plant Journal* 65.2 (Jan. 2011), pp. 282–94. ISSN: 1365-313X.

[71] Melanie Monroe-Augustus, Bethany K Zolman, and Bonnie Bartel. “IBR5, a dual-specificity phosphatase-like protein modulating auxin and abscisic acid responsiveness in Arabidopsis.” In: *The Plant Cell* 15.12 (Dec. 2003), pp. 2979–91. ISSN: 1040-4651.

[72] D Reinhardt, T Mandel, and C Kuhlemeier. “Auxin regulates the initiation and radial position of plant lateral organs.” In: *The Plant cell* 12.4 (Apr. 2000), pp. 507–18. ISSN: 1040-4651.

[73] K. Okada et al. “Requirement of the Auxin Polar Transport System in Early Stages of Arabidopsis Floral Bud Formation.” In: *The Plant Cell* 3.7 (July 1991), pp. 677–684. ISSN: 1040-4651.

[74] Eva Benková et al. “Local, efflux-dependent auxin gradients as a common module for plant organ formation.” In: *Cell* 115.5 (Nov. 2003), pp. 591–602. ISSN: 0092-8674.

[75] Didier Reinhardt et al. “Regulation of phyllotaxis by polar auxin transport.” In: *Nature* 426.6964 (Nov. 2003), pp. 255–60. ISSN: 1476-4687.

[76] Pierre Barbier de Reuille et al. “Computer simulations reveal properties of the cell-cell signaling network at the shoot apex in Arabidopsis.” In: *Proceedings of the National Academy of Science of the United States of America* 103.5 (Jan. 2006), pp. 1627–32. ISSN: 0027-8424.

[77] Wim Grunewald and Jirí Friml. “The march of the PINs: developmental plasticity by dynamic polar targeting in plant cells.” In: *The EMBO Journal* 29.16 (Aug. 2010), pp. 2700–14. ISSN: 1460-2075.

[78] Marcus G Heisler et al. “Patterns of auxin transport and gene expression during primordium development revealed by live imaging of the Arabidopsis inflorescence meristem.” In: *Current biology* 15.21 (Nov. 2005), pp. 1899–911. ISSN: 0960-9822.

[79] Jennifer C Fletcher. “Shoot and floral meristem maintenance in arabidopsis.” In: *Annual review of plant biology* 53 (Jan. 2002), pp. 45–66. ISSN: 1543-5008.

[80] L Dolan et al. “Cellular organisation of the Arabidopsis thaliana root.” In: *Development* 119.1 (Sept. 1993), pp. 71–84. ISSN: 0950-1991.

[81] W. Boerjan. “superroot, a Recessive Mutation in Arabidopsis, Confers Auxin Overproduction”. In: *The Plant Cell* 7.9 (Sept. 1995), pp. 1405–1419. ISSN: 10404651.

[82] J E Malamy and P N Benfey. “Organization and cell differentiation in lateral roots of Arabidopsis thaliana.” In: *Development* 124.1 (Jan. 1997), pp. 33–44. ISSN: 0950-1991.

[83] J L Celenza, P L Grisafi, and G R Fink. “A pathway for lateral root formation in Arabidopsis thaliana.” In: *Genes & Development* 9.17 (Sept. 1995), pp. 2131–42. ISSN: 0890-9369.

[84] Franck Anicet Ditengou et al. “Mechanical induction of lateral root initiation in Arabidopsis thaliana.” In: *Proceedings of the National Academy of Sciences of the United States of America* 105.48 (Dec. 2008), pp. 18818–23. ISSN: 1091-6490.

[85] M Lucas et al. “Auxin fluxes in the root apex co-regulate gravitropism and lateral root initiation.” In: *Journal of Experimental Botany* 59.1 (Jan. 2008), pp. 55–66. ISSN: 1460-2431.

[86] Ive De Smet et al. “Auxin-dependent regulation of lateral root positioning in the basal meristem of Arabidopsis.” In: *Development* 134.4 (Feb. 2007), pp. 681–90. ISSN: 0950-1991.

[87] Bernadette Guenot et al. “Pin1-independent leaf initiation in Arabidopsis.” In: *Plant Physiology* 159.4 (Aug. 2012), pp. 1501–10. ISSN: 1532-2548.

[88] Taylor A. Steeves and Ian M. Sussex. *Patterns in Plant Development.* 2nd Editio. Cambridge, England, 1989, p. 408. ISBN: 9780521288958.

[89] Marta Ibañes et al. “Brassinosteroid signaling and auxin transport are required to establish the periodic pattern of Arabidopsis shoot vascular bundles.” In: *Proceedings of the National Academy of Sciences of the United States of America* 106.32 (Aug. 2009), pp. 13630–5. ISSN: 1091-6490.

[90] Idan Efroni et al. “A protracted and dynamic maturation schedule underlies Arabidopsis leaf development.” In: *The Plant cell* 20.9 (Sept. 2008), pp. 2293–306. ISSN: 1040-4651.

[91] Nancy G Dengler and Hirokazu Tsukaya. *Leaf Morphogenesis in Dicotyledons: Current Issues.* 2001.

[92] P M Donnelly et al. “Cell cycling and cell enlargement in developing leaves of Arabidopsis.” In: *Developmental biology* 215.2 (Nov. 1999), pp. 407–19. ISSN: 0012-1606.

[93] Kiu Hyung Cho et al. “Developmental processes of leaf morphogenesis inarabidopsis”. In: *Journal of Plant Biology* 50.3 (June 2007), pp. 282–290. ISSN: 1226-9239.

[94] Eiko Kawamura, Gorou Horiguchi, and Hirokazu Tsukaya. “Mechanisms of leaf tooth formation in Arabidopsis.” In: *The Plant journal* 1 (Mar. 2010), pp. 429–441. ISSN: 1365-313X.

[95] Gemma D Bilsborough et al. “Model for the regulation of Arabidopsis thaliana leaf margin development.” In: *Proceedings of the National Academy of Sciences of the United States of America* 108.8 (Feb. 2011), pp. 3424–9. ISSN: 1091-6490.

[96] Carol L Wenzel et al. “Dynamics of MONOPTEROS and PIN-FORMED1 expression during leaf vein pattern formation in Arabidopsis thaliana.” In: *The Plant journal : for cell and molecular biology* 49.3 (Mar. 2007), pp. 387–98. ISSN: 0960-7412.

[97] T. Sachs. “Polarity and the Induction of Organized Vascular Tissues”. In: *Annals of Botany* 33.2 (Mar. 1969), pp. 263–275.

[98] G. J. Mitchison. “A Model for Vein Formation in Higher Plants”. In: *Proceedings of the Royal Society B: Biological Sciences* 207.1166 (Feb. 1980), pp. 79–109. ISSN: 0962-8452.

[99] G. J. Mitchison, D. E. Hanke, and A. R. Sheldrake. “The Polar Transport of Auxin and Vein Patterns in Plants [and Discussion]”. In: *Philosophical Transactions of the Royal Society B: Biological Sciences* 295.1078 (Oct. 1981), pp. 461–471. ISSN: 0962-8436.

[100] Hironori Fujita and Atsushi Mochizuki. “Pattern formation of leaf veins by the positive feedback regulation between auxin flow and auxin efflux carrier.” In: *Journal of Theoretical Biology* 241.3 (Aug. 2006), pp. 541–51. ISSN: 0022-5193.

[101] François G Feugier and Yoh Iwasa. “How canalization can make loops: a new model of reticulated leaf vascular pattern formation.” In: *Journal of Theoretical Biology* 243.2 (Nov. 2006), pp. 235–44. ISSN: 0022-5193.

[102] K Alim and E Frey. “Quantitative predictions on auxin-induced polar distribution of PIN proteins during vein formation in leaves.” In: *The European Physical Journal. E, Soft Matter* 33.2 (Oct. 2010), pp. 165–73. ISSN: 1292-895X.

[103] Francois G Feugier, A Mochizuki, and Y Iwasa. “Self-organization of the vascular system in plant leaves: inter-dependent dynamics of auxin flux and carrier proteins.” In: *Journal of Theoretical Biology* 236.4 (Oct. 2005), pp. 366–75. ISSN: 0022-5193.

[104] Szymon Stoma et al. “Flux-based transport enhancement as a plausible unifying mechanism for auxin transport in meristem development.” In: *PLoS Computational Biology* 4.10 (Oct. 2008), e1000207. ISSN: 1553-7358.

[105] Richard S Smith et al. “A plausible model of phyllotaxis.” In: *Proceedings of the National Academy of Sciences* 103.5 (Jan. 2006), pp. 1301–6. ISSN: 0027-8424.

[106] Alan C Newell, Patrick D Shipman, and Zhiying Sun. “Phyllotaxis: cooperation and competition between mechanical and biochemical processes.” In: *Journal of Theoretical Biology* 251.3 (2008), pp. 421–39. ISSN: 1095-8541.

[107] Henrik Jönsson et al. “An auxin-driven polarized transport model for phyllotaxis.” In: *Proceedings of the National Academy of Sciences* 103.5 (Jan. 2006), pp. 1633–8. ISSN: 0027-8424.

[108] Roeland M H Merks et al. “Canalization without flux sensors: a traveling-wave hypothesis.” In: *Trends in Plant Science* 12.9 (Sept. 2007), pp. 384–90. ISSN: 1360-1385.

[109] Emmanuelle M Bayer et al. “Integration of transport-based models for phyllotaxis and midvein formation.” In: *Genes & Development* 23.3 (Feb. 2009), pp. 373–84. ISSN: 1549-5477.

[110] Marcus G. Heisler et al. "Alignment between PIN1 Polarity and Microtubule Orientation in the Shoot Apical Meristem Reveals a Tight Coupling between Morphogenesis and Auxin Transport". In: *PLoS Biology* 8.10 (Oct. 2010). Ed. by Ottoline Leyser, e1000516. ISSN: 1545-7885.

[111] Gerardo Tauriello and Petros Koumoutsakos. "Coupling Remeshed Particle and Phase Field Methods for the Simulation of Reaction-Diffusion on the Surface and the Interior of Deforming Geometries". en. In: *SIAM Journal on Scientific Computing* 35.6 (Jan. 2013), B1285–B1303. ISSN: 1064-8275.

[112] Johannes Schindelin et al. "Fiji: an open-source platform for biological-image analysis." In: *Nature Methods* 9.7 (July 2012), pp. 676–82. ISSN: 1548-7105.

[113] Daniel Kierzkowski et al. "Elastic domains regulate growth and organogenesis in the plant shoot apical meristem." In: *Science* 335.6072 (Mar. 2012), pp. 1096–9. ISSN: 1095-9203.

[114] Romain Fernandez et al. "Imaging plant growth in 4D: robust tissue reconstruction and lineaging at cell resolution." In: *Nature Methods* May (June 2010). ISSN: 1548-7105.

[115] Tony J Collins. "ImageJ for microscopy". In: *BioTechniques* 43.S1 (2007), S25–S30.

[116] Bruce E Shapiro, Elliot M Meyerowitz, and Eric Mjolsness. "Using cellzilla for plant growth simulations at the cellular level." In: *Frontiers in plant science* 4 (Jan. 2013), pp. 1–9. ISSN: 1664-462X.

[117] Bruce E Shapiro et al. "Cellerator: extending a computer algebra system to include biochemical arrows for signal transduction simulations." In: *Bioinformatics (Oxford, England)* 19.5 (Mar. 2003), pp. 677–8. ISSN: 1367-4803.

[118] Maruthachalam Ravi and Simon W L Chan. "Haploid plants produced by centromere-mediated genome elimination." In: *Nature* 464.7288 (Mar. 2010), pp. 615–8. ISSN: 1476-4687.

[119] Hirokazu Tsukaya. "Mechanism of leaf-shape determination." In: *Annual review of plant biology* 57 (Jan. 2006), pp. 477–96. ISSN: 1543-5008.

# Chapter 3

# Meristem Size and Phyllotaxis

## 3.1 Introduction

In the meristem of plants, leaves and flowers form around the periphery and are pushed radially outward as the cells of the meristem divide and expand. The angles between successive organs, called divergence angles, are fixed in place even as the shoot grows in length and circumference. In many plants, the relative positioning of organs around the shoot, called phyllotaxis, takes on a spiral pattern. This spiral is composed of divergence angles approximately equal to the golden angle of ∼137.5°, which has led many people to wonder about the mathematical nature of the pattern forming mechanism. Phyllotaxis has been studied and speculated about for centuries but with modern technology and methodology we can begin to unravel the complex phenomena underlying these beautiful patterns.

### 3.1.1 History of Phyllotaxis

Leonardo da Vinci was the first to suggest that the spirals found throughout the plant kingdom provide a fitness advantage. He suggested that the spirals maximize the number of leaves or flowers that can fit around the shoot to maximize the collection of sunlight and rainfall[1]. Johann Wolfgang von Goethe, the German poet and philosopher, wrote about the general pattern he observed where plants create a spiral pattern with their leaves[2]. Goethe had extensively written in “Versuch die Metamorphose der Pflanzen zu erklären” about the homologous nature of different organs through the plant's development from the early cotyledons to the photosynthetic leaves to the petals and sepals of the flowers, deducing that they were all modifications of the same basic structure, specialized for different functions like reproduction. He speculated that the same phyllotaxis mechanism was used throughout the life of the plant.

More insight about the mechanism of spiral pattern generation came when Wilhelm Hofmeister proposed in 1868 that organ primordia form in areas of least crowding around the meristem. He suggested that the golden angle arose when successive primordia push on each other through physical forces, guaranteeing that the flowers would not form a straight radial line from the center of the meristem outward[3], similar to how spherical objects will pack with each layer being shifted horizontally from the last simply due to gravity and physical forces between the spheres.

Ten years later Simon Schwendener published the book "Mechanische Theorie der Blattstellungen"[4] in which he asserted that the different observed arrangement of leaves results from pressure exerted by each leaf on its neighbors, similar to Hofmeister's idea. He used a combination of diagrams and calculations along with a mechanical device which he constructed, essentially a specialized analog computer, to compute the forces experienced by leaves during development. While these devices were not built using knowledge of the biochemistry involved, they did provide a plausible mechanism for pattern formation.

Arthur Harry Church in 1904 furthered this mechanical line of thinking and proposed that the shoot apical meristem is the origin of the observed pattern, as opposed to the organs moving around the meristem after formation[5]. He introduced the concept of parastichies which were lines of force that traced the path of the organs down the stem and took on different wavelengths to produce the different observed phyllotaxis patterns. He named this "equipotential phyllotaxis" and created a very thorough theory of the parastichies, analogous to the theory of electromagnetism, with equations describing all the ways in which parastichy forces interact to produce phyllotaxis patterns. Additionally, he proposed many metaphysical theories about how life energy flowed through parastichy force lines. Ultimately he failed to realize that the observed phyllotaxis patterns could arise without the need for incredibly complex waves and force interactions around the shoot.

In the early 20th Century Robert and Mary Snow realized that all the proposed phyllotaxis models fell into one of two categories: either the position of the organ was predetermined by an unknown property in the stem or the positions of the organs were determined by physical contact with other existing organs. They suggested that if the latter model was correct then moving or removing older organs should influence the positions of new organ primordia. This led to the first experiments on phyllotaxis. They surgically removed floral primordia in lupin plants and observed the formation of new primordia under a microscope[6]. In this experiment they determined that isolating a primodium caused the phyllotaxis spiral to reverse and form a new primordium across the meristem from where they would have expected it to form. As a result of this work the Snows developed the concept of "first available space", similar to what had been proposed by Hofmeister 60 years prior. In this theory new primordia form in the area with the widest gap[6, 7, 8].

Following up on the Snows' work, Claude Wilson Wardlaw performed microsurgery on the fern Dryopteris and arrived at a similar but not identical conclusion[9]. Wardlaw built on the "first available space" theory and proposed inhibitory fields emanating from each primordia. This proposal also built on the work of Johannes Schoute in 1913 who had also proposed that the patterning of organ placement involved chemical inhibitors[10]. Wardlaw suggested that the inhibitory field was not a "causal factor" but that new primordia tended to emerge at locations where the inhibitory field was weakest[9]. In this case, the most recently formed primordium was the source of the strongest inhibitory field so the next primordium formed across the meristem from the last. After Wardlaw's work, the idea of inhibitory fields stuck around and became an important factor in subsequent phyllotaxis models.

The British mathematician and WWII cryptanalyst Alan Turning picked up on Wardlaw's work and towards the end of his life developed his own mathematical models incorporating the idea of inhibitory fields. He published "The Chemical Basis for Morphogenesis" where he laid out differential equations describing reaction-diffusion systems that could explain the spiral partterns of phyllotaxis[11]. In this model, small random disturbances to the uniform initial state of the partial differential equations led to pattern formation. After initiation, the spiral pattern became steady.

The work of Hofmeister was later revisited by Stéphane Douady and Yves Couder. They built a system to test if the crowding theory could create the spiralling patterns seen in phyllotaxis. They added drops of ferrofluid (a liquid with microscopic magnetic solid particles in suspension) to a magnetized plate of silicone oil. The ferrofluid drops repelled each other and created spiralling Fibonacci patterns around the circular dish[12, 13, 14, 15]. Their observations showed that the ferrofluid phyllotaxis pattern was controlled by a single simple equation

$$G = \frac{V_0 T}{R_c} \tag{3.1}$$

where $V_0$ is the velocity, in this case determined by the magnetic field gradient, $T$ is the frequency of the drips, and $R_c$ is the radius from the center of the plate that the drop was placed. The resulting parameter $G$ is the ratio of two length scales that affected the pattern of the ferrofluid drops: the radial displacement of the drops during one period ($V_0T$) and the size of the central region ($R$). Or put another way, $G$ was related to the plastochrone ratio proposed by Francis Richards[16] which characterized phyllotaxis patterns with the equation:

$$a = \frac{r_{n-1}}{r_n} \tag{3.2}$$

or the ratio of radii of two successive organ primordia. $G$ turned out to be related to Richard's equation by a simple natural logarithm:

$$G = \ln(a) \tag{3.3}$$

Douady and Couder concluded that all dynamic models where new primordia form in a position repelled by or inhibited by existing primordia will inherently give rise to phyllotaxis organization of Fibonacci order and spirals with angles that eventually converge on the golden angle — a phenomenon which minimizes the value of $G$[13].

Around the same time Paul Green was also working on the idea that phyllotaxis is controlled by geometric ratios but proposed that that chemical gradients or repulsive forces between primordia were not necessary. Green proposed a model where compression, tension, and shear in the outer layer of the meristem epidermis control the placement of new primordia[17, 18]. In this theory, stress and strain accumulated in the epidermis as a result of meristem cells dividing and expanding, pushing on all of the surrounding cells. The sites of buckling (out of plane deflection caused by in plane compression) are the sites where primordia form. Green concluded that this growth-dependent patterning was regulated at the level of the entire meristem rather than being a result of local forces. As the entire meristem grows approximately equal in all directions, wrinkles form similar to those observed in wet skin that expands when its keratin absorbs water. Luis Francisco Hernandez along with Green made computer models of these biophysical forces in the sunflower capitulum and were able to recreate observed phyllotaxis patterns[19].

Hernandez and Green explored this buckling model further *in vivo* by growing sunflowers in devices that constrained the growth of their meristems. These perturbations led to alterations of the phyllotaxis pattern that agreed with predictions made by their previous computer models[19].

They interpreted these results to mean that mechanical buckling was upstream of any biochemical process or tissue differentiation. Through an unknown mechanism, cells that are under increased buckling strain detect that strain and propagate a signal to alter the biochemical state of the cell and ultimately cause the transcriptional changes needed to create a flower or leaf.

The concept of strain and buckling in the meristem causing phyllotaxis patterns was further explored by Dumais and Steele around the year 2000. They experimented with making cuts in different parts of the sunflower capitulum and observing the reaction of the surrounding tissue[20]. When they made cuts at the apex of the meristem the wounds were pulled open, suggesting that the tissue was under tension. When they made cuts around the periphery of the meristem the wounds remained closed, suggesting that the tissue was under circumferential compression. The area of the meristem where primordia are formed was under compression which strongly bolstered Green's theory. Now that the buckling theory had experimental evidence supporting it, Patrick Shipman and Alan Newell expanded the concept with a thorough mathematical treatment and determined that the observed buckling patterns could be explained by the compression of a flat rigid sheet sitting on top of an elastic material[21, 22]. The overarching message from their work is that if the meristem is large enough such that the ratio of its circumference to the buckling wavelength is large then the deformations (sites of organ formation) arise as linear combinations of the cosine of the radial and circumferential coordinates multiplied by their respective wavenumbers.

Meanwhile, biochemical explanations for phyllotaxis also began to fall into favor. It had long been known that organ primordia fail to form in Arabidopsis plants with mutant auxin transporters[23]. But work in Cris Kuhlemeier's lab on both Arabidopsis and tomato showed that auxin is necessary and sufficient for the initiation of organ primordia[24, 25, 26, 27]. They demonstrated that by applying auxin in a waxy paste to the surface of the meristem in a location where a primordia was not expected to form led to the initiation of an organ in that location. Additionally they showed that blocking polar auxin transport by application of N-1-naphthylphthalamic acid blocks the formation of organs. Further, evidence produced by Marcus Heisler showed that auxin was being transported by the polar transporter PIN1 in such a way as to direct all the auxin in an area to a point where an organ primordium would eventually form, solidifying the concept of auxin accumulation being upstream of organ differentiation[28].

As you can see, two different paradigms for regulation of organ formation have emerged. One is mechanical and the other biochemical. Many questions remain to be answered. Is one right and one wrong? If one is wrong, is the supporting evidence just purely coincidental? If they are both right, what is the nature of the connection between the mechanical and biochemical? Do biochemical signals lead to mechanical buckling or is it the other way around? Some progress has been made towards resolving this conflict. Marcus Heisler and Olivier Hamant showed that mechanical perturbation (laser ablation of cells in the meristem) led to the repositioning of auxin transporters in nearby cells[29]. Additionally, through a combination of experiments, image processing and mechanical computer modeling Richard Smith and colleagues were able to determine that mechanical forces can act as a feedback signal on meristem patterning affecting the biochemistry[30]. But while connections between the biochemical and mechanical have been made, critical pieces of the puzzle remain at large, particularly mechanisms for sensing strain and the pathway leading from auxin accumulation to strain.

In this work I seek to push our understanding of phyllotaxis patterning further by exploring the relationship of the meristem size to the divergence angles produced — a relationship suggested by the models in Chapter 2. This ties in closely with Douady and Couder's assertion that phyllotaxis patterns are a result of simple geometric ratios and more recently the work by Oliver Hamant and colleagues, who have also made careful measurements of meristem sizes[31]. By using advanced, modern measurement techniques I seek to quantify relevant geometric parameters in the meristem and compare those with the macroscopically observed phyllotaxis patterns.

### 3.1.2 Measurement of Phyllotaxis

There are two general strategies when it comes to measuring phyllotaxis. One is to measure divergence angles and plastochrons (the spacing between successive organs) of the siliques of mature plants. The other is to measure the divergence angles of primordia by looking at the meristem. Both of these strategies theoretically result in the same output but the measurements may not always be exactly equal as there is a lot of growth, potentially anisotropic, in between the time when primordia emerge and when the siliques have matured. In some cases, anisotropic growth in the stem can create a large disconnect between these two measurements as in the case of the bp-1 multant[32].

Much of the early work on phyllotaxis, such as that by Hofmeister, Schwendener, and Snow, was done by observing leaf primordia around the meristem using compound microscopes. Since cameras were not a staple in biology labs at that point in time, measurements were taken using eye-piece reticles and pictures of the meristems were sketched by hand. While this method did suffice, it left for a lot of guess work. The later additions of comparator reticles and photomicroscopy did help but larger gains in accuracy were made with the development of the scanning electron microscope (SEM).

Beginning in the 1920's physicists experimenting with electron beams found they could steer the beams and detect the reflection, providing a method that, in theory, could create much higher resolution images than optical microscopy[33]. For many decades the technique was limited to specialized labs and was an experiment in itself. In 1965 the first commercial scanning electron microscope, the Cambridge Scientific Mark I Stereoscan, was produced and allowed non-physicists to make high magnification, high resolution, high contrast images of the surfaces of their samples[34]. One of the biggest innovations with this device was the development of long-life CRT phosphors that allowed images to be transferred from the CRT screen (which would typically only allow for temporary viewing of the sample) to photographic film. This meant images could be developed into photographs and features could be measured on paper with good accuracy and repeatability, since the magnification ratios of sample to CRT and CRT to film were known.

The first SEM images of plants, published in 1973, were taken by John Owens and Marje Molder who were looking at rates of mitosis in the meristems of conifers[35]. Shortly after, Paul Green also began using this technique to study the regeneration of stems from leaf tissue[36]. Other plant scientists picked up on this[37, 38, 39, 40] and by the mid 1908s SEM had become a routine procedure for making precise measurements of microscopic plant morphology, including divergence angles between successive primordia[41]. But while this tool provided very detailed images of meristem morphology it had its drawbacks — primarily that the samples have to be fixed under harsh conditions, dehydrated, and placed in a hard vacuum, which can distort some of the morphological features. Additionally, the specimen can only be viewed at one point in time since the process is destructive.

Another technique was developed in Paul Green's lab that preserved the plant tissue but also provided the high resolution of SEM[42]. In this technique a mold is made of the meristem using the same quick-setting polymers used in dental molds. From the negative mold a positive cast is made from a material that can be sputtered with gold and placed in the vacuum for SEM imaging. This technique preserves very fine details of the meristem, even small meristems like those of Arabidopsis, and is non-destructive to the plant. A series of dental molds can be made from the same specimen to track morphology over time. This method is still used today in situations where the non-destructive nature of the technique is critical and high resolution images of the tissue surface are needed[30].

Even with the benefits that SEM and dental molds have provided for measuring microscopic morphological features, there is still room for improvement. While SEM images appear to be three-dimensional since shadows are visible, the appearance of depth is an illusion. In machines with backscatter detectors, the electrons are returned to the detector after being reflected and the returning electrons are blocked in the same way that light would be, leading to shadows. But the images produced by the detector are still only two-dimensional. Measurements taken from these images can not take the z-axis into account.

Advances in light microscopy allow for high resolution fluorescent images of the meristem in three dimensions. In confocal microscopy, out of focus light (light not emitted from the focal plane) is blocked by a pin hole, allowing for samples to be optically sectioned by moving the sample through the focal plane and taking a two-dimensional image at each height. The only limit to resolution is the wavelength of the emitted light which, while not as great as SEM, is sufficiently good enough for measuring distances between organs in three dimensions in the meristem. It also provides a view inside the tissue rather than just the surface. Advances to the imaging techniques have actually allowed for resolutions below the diffraction limit[43, 44] but it has been the advances in 3D image processing that have made the largest impact on our ability to quantify the morphology of the shoot apical meristem[45].

In addition to measuring phyllotaxis at the microscopic level of the meristem, it can also be measured by observations of the whole plant. One technique that has been commonly used throughout the history of research on phyllotaxis is to take a picture from the top of the plant. Divergence angles can then either be measured on a printout (or developed photo) or on a computer using a digital image and basic microscopy software like Fiji[46]. This method provides the benefit of being quick and simple, although it is limited to the apical most leaves or flowers as they will obscure the view of those below. Another approach is to use a divergometer, essentially a protractor that can move up and down the vertical axis of the plant to measure the divergence angles visually. A third approach to this problem is to use tomographic techniques for constructing a 3D model of the entire plant. This would provide the benefit of producing divergence angles for the entire plant all at once instead of just a few as is the case with meristem microscopy and could potentially be faster than a divergometer.

### 3.1.3 Tomography

Tomography is an imaging technique where a three-dimensional image is created by taking multiple two dimensional image "slices". The medium can be radiation, sound or any other type of wave but in this work I will refer only to radiation. Typically, images are taken from multiple angles and a three-dimensional image is created through a process called tomographic reconstruction.

The first use of this technique was developed by an Italian radiologist who figured out that by moving the X-ray tube around a point of interest during the exposure, the point would become brighter while everything out of the focal plane would blur[47]. The use of a similar technique became regular practice in the 1950s where it was used on chest X-rays[48] of tuberculosis patients. Taking X-rays from multiple angles gave the doctors a precise location of lesions prior to surgery. For 20 years, X-ray tomography was limited to manually or semi-manually positioning the X-ray tube and film cassette around the patient to acquire the needed angles. Devices were constructed to aide in positioning the device at precise locations but the resulting images were inspected visually and a three dimensional image was not reconstructed except for in the practitioner's mind[49].

In order to make X-ray tomography the precise and ubiquitous procedure that it is today, new math and electronics were needed. Prior to the first use of X-ray tomography the mathematician Johann Radon proved that any function can be reconstituted using the infinite projections of that function[50]. Since starting with an infinite set is impossible, Stefan Kaczmarz developed techniques for numerically approximating the function using a finite set of projections. This method is called the Algebraic Reconstruction Technique and is represented by a single equation:

$$x^{k+1} = x^k + \lambda_k a_i \frac{b_i - (a_i, x^k)}{||a_i||^2} \tag{3.4}$$

Each pixel is represented by a vector $x$, the measured projections are $b$, and $\lambda$ is a relaxation parameter to balance the accuracy and the number of iterations needed to achieve that accuracy. As more and more projections (images from a different angle) are added, the original function (the 3D object that is being reconstructed) is converged upon. This mathematical technique is the foundation of most tomographic reconstruction and not just limited to X-rays.

With the rise of digital computers and these mathematical methods, Godfrey Hounsfield was able to build the first computed tomography machine for which he was awarded a Nobel Prize. The innovations in this field also helped with progress with other types of 3D reconstruction. X-ray crystallography which, although it measures scattering instead of absorbance, borrows some of the same math and positioning techniques and has made large advances in biology[51]. With advances in digital camera, optical tomography has also become a possibility.

Optical tomography is the technique where multiple images taken with a camera are combined to make a single 3D model of an object or scene. This can be done with multiple stacks of parallel slices as is the case with confocal microscopes or with images of the surface of opaque objects. In the case of confocal microscopy, Christophe Godin's lab developed a software package for reconstructing the cellular structure of meristems in 3D using confocal z-stacks taken from three different angles[52]. The process involves first identifying the locations of common landmarks in all the images by hand to create an initial approximate alignment. Then a rigid transformation (particularly a block matching algorithm[53]) followed by a pyridimal alignment algorithm[54] precisely aligns the images. The end result is that data from one image that was not captured in the another image (due to the angle and slice spacing) are all combined into a single image containing more structures than any of the individual images.

The same concept is used in optical tomography of opaque objects. An image taken from one side of the object will only capture information about the object that is visible on that side. Some features will be partially or completely obscured. By combining images from different angles a more complete model of the object can be built. In a rudimentary set-up the images would need to be aligned manually, which could be difficult considering the differences in working distances and background between images. To rectify this, modern optical tomography software makes use of reference targets that are printed with specific patterns to aid in determining the position of the camera in each image automatically, assuming the targets remain stationary. This technique is frequently used in forensics to create 3D models of a scene[55] or in surveys of archaeological sites[56].

In this work, optical tomography is used to capture and construct 3D models of whole plants with enough detail to extract the divergence angles between the successive siliques. With more advanced imaging techniques at both the microscopic and macroscopic levels and more advanced image processing techniques we should be able to make the most accurate measurements of plant morphology yet. This will aid in determining the relationship between meristem size and phyllotaxis pattern.

## 3.2 Methods

### 3.2.1 Plant Growth Conditions

Wild type and mutants lines as shown in table 3.2 were used. When plants were grown in soil, pots of soil were made using the following composition:

- 2 parts Sunshine Mix
- 2 parts SuperSoil Potting Soil
- 1 parts Vermiculite
- 1 parts Perlite
- 0.02 parts Marathon insecticide

Pots were arranged in flats of 12 pots and stored at 4°C for three days before transferring to a growth chamber with 24h illumination. Flats were given 1cm of water every 2 days.

**Materials for Growing in Soil**

- High wall petri dishes (Electron Microscopy Sciences, #64332)
- Sunshine Mix (McConkey Co, #SUNSM2)
- SuperSoil Potting Soil (SMG Growing Media)
- Vermiculite #2 Coarse (McConkey Co, #TRWVMIC26)
- Perlite (McConkey Co, #TRWPERL6)
- Marathon Insecticide 1% (OHP Inc, EPA #432-1329-59807)

### 3.2.2 Microscopy

Plants from one of the genetic backgrounds listed on table 3.2 were grown in soil as described in section 3.2.1. These plants were grown under continuous light until the shoots entered the reproductive phase and bolted. Flowers were removed with sharp forceps under a dissecting microscope. The meristem and approximately 5mm of stem were removed using forceps and placed in a glass slide. The slide was refrigerated for 15 minutes. This slows endocytosis, which would increase the background noise while imaging FM4-64.

High wall petri dishes were prepared with 1% phytoagar made with DI water. A 1mL solution of 5ug/mL FM4-64 in DI water was prepared from a 200ug/mL stock solution of FM4-64.

- 1% PhytoAgar
- 4.3g/L Murashige and Skoog Basal Salt Mixture
- 1mL 1000x concentrated Murashige and Skoog Vitamin Solution
- 30g/L sucrose
- 50ug/mL kanamycin monosulfate.
- 1L DI water

After the meristem tissue sat at 4°C for 15 minutes, 50uL of the FM4-64 solution was placed on each meristem using a 200uL pipette. The glass slide containing the meristems was placed back in the refrigerator at 4°C for another 15 minutes. Small holes were poked in the agar in the petri dishes. The meristems were removed from the slide and the drop of FM4-64 solution was removed with a Kimwipe. The Meristems were then stuck into the holes in the agar facing upward so the stems protruded into the holes, holding the meristems firmly in place. DI water was added to the petri dishes to a height 1cm above the top of the meristems.

Meristems in agar were imaged using a Zeiss LSM 510 laser scanning confocal microscope with a 63x 0.95NA Achroplan water dipping objective. The sample was excited using a single 488nm laser through a 488nm dichroic mirror which can excite both FM4-64 and GFP (only FM4-64 if not imaging KAN1). A 500-525nm bandpass filter was used to capture light from GFP and a 650nm longpass filter was used to capture light from FM4-64 simultaneously.

Images from this procedure were processed using the technique described below in section 3.2.3. Meshes generated in MorphoGraphX were analysed to find the locations of KAN1 cells so the boundary of the meristem could be determined.

### 3.2.3 Meristem Image Processing

The first step for importing the data into MorphoGraphX was to convert the z-stack into TIFF format. The easiest tool for this job is ImageJ or Fiji, which is a particular distribution of ImageJ with many useful plug-ins already installed. In this work Fiji was used in place of ImageJ but ImageJ can be used also. In that case a plug-in would need to be installed which allows ImageJ to read the particular z-stack format, in this case an LSM file (LSMToolbox for Zeiss LSM files, Loci_tools for Leica LIF files, Bio-formats for Nikon ND2 or Zeiss CZI files).

In order for MorphoGraphX to interpret the image file correctly the first image in the series to be the top of the meristem. When the order was reversed the data was exported as a series of individual TIFF files rather than a multi-TIFF so the order of the images could be reversed.

Before beginning the image processing, some steps were taken to insure all the software was set up and our data was ready to be processed.

- ImageJ or Fiji was installed
- MorphoGraphX was installed. On Ubuntu this can be done through the built-in package manager.
- The x,y,z dimensions of the voxels from the image file metadata were retrieved.

#### 3.2.3.1 Multiple TIFF Images

When exporting the image data from LSM files into a series of TIF images, the following procedure was used.

1. Open ImageJ or Fiji.
2. Click on *File*, then *Save As*, then *Image Sequence*.
3. Select the TIFF format and start the numbering at 0.
4. Click *OK*.
    - This will create multiple image files.
    - One file for each slice in the z-stack.

The following Bash script (OSX, Linux or Cygwin environments only) was used to reverse the numerical order of the TIF file names when needed. This assumes the files are named like "image3.tif". The second line of the script can be modified if the files are named differently. The script was copied into the same directory as the multiple TIFF files and run.

```
#!/bin/bash
image=( image*.tif )
MAX=${#image[*]}
```

```
for i in ${image[*]}
do
   num=${i:5:3} # grab the digits
   compliment=$(printf '%03d' $(echo $MAX-$num | bc))
   ln $i copy_of_image$compliment.tif
done
```

In order to import these TIF images into MorphoGraphX, the following procedure was used:

1. The MorphGraphX program was started.
2. In the top menu bar select *Stack* then *Stack1* then *Main* then *Image Sequence*.
3. Click *Add Files*.
4. Select all of the image files in the series.
5. Click *OK*.
6. Input the X, Y, and Z dimensions of the voxels in micrometers.
   - These data were available in the metadata associated with the original image file.
7. Click *Start* and the stack appears in the main window in a semi-transparent state as seen in Figure 2.2A.

#### 3.2.3.2 Single TIFF Image

In order to export the data as a single multi-TIFF image, the following procedure was used.:

1. Click on *File*, then *Save As*, then *Tiff*.
2. Select the TIFF format and start the numbering at 0.
   - This created multiple image files, one for each slice in the z-stack.
   - This file was imported into MorphoGraphX.
3. Open the MorphoGraphX program.
4. Drag the TIFF file into the main window.
   - This opens a window where the X, Y, and Z dimensions of the voxels in micrometers are manually entered.

- These data were available in the metadata associated with the original image file.

5. Click *Start* and the stack appears in the main window in a semi-transparent state as seen in Figure 2.2A.

#### 3.2.3.3 Building the Mesh

The same general procedure for building a mesh from a z-stack was used as described in Section 2.2.11.5.

#### 3.2.3.4 Segmenting

When using the KAN1 reporter this method was used for detecting the meristem edge cells were segmented from the mesh

1. At the left side of the window, click the *Add New Seed* tool.
2. Hold hold *Ctrl* and *Alt* and use the mouse to click the interior of a cell.
3. Do this for each cell as seen in Figure 2.3A.
    - Each cell should turn a different color.
    - You can drag the mouse to color a larger portion of the cell interior.
    - This can help if the background noise is high.
    - Each time you click you are drawing with a new cell-seed.
    - If you have already picked the mouse up but want to keep drawing with the same seed, select the *Add Current Seed* tool and draw with that.
    - To revert back to making new seeds, select the *Add New Seed* tool again.
    - To erase a seed:
        (a) Click on the *Label Color* (the colored box at the top of the window). The color should disappear.
        (b) Choose the paint bucket tool.
        (c) Click on the seed that you want to erase.

- With a new seed, draw a circle around the area you want segmented as seen in Figure 2.3A.

4. In the *Process* tab, expand the *Segmentation* section.
5. Click on *Watershed Segmentation.*
6. Use the default parameters.
7. Click *Go.*
8. Wait for the segmentation to complete.
9. If you are satisfied with the segmentation, proceed to step 12.
10. If there are corners between the cells that are not assigned a color:
    - 10.1. In the *Process*, *Mesh*, *Cell Mesh* section select *Fix Corners.*
    - 10.2. Click *Go.*
    - 10.3. In the *Segmentation* section, choose *Watershed Segmentation.*
    - 10.4. Click *Go.*
    - 10.5. The corners should now be fixed.
11. If you are not satisfied with the smoothness of the boundaries:
    - 11.1. In the *Process*, *Mesh*, *Structure* section select Subdivide Adaptive Near Borders.
    - 11.2. Map the signal data onto the mesh again using the procedure described previously at step in the section "Building the Mesh".
    - 11.3. In the *Process*, *Segmentation* section select *Watershed Segmentation.*
    - 11.4. Use the default parameters.
    - 11.5. Click *Go.*
12. Expand the *Cell Mesh* section and select *Convert to Cells.*
13. Choose a value of 1$\mu$m for the *Minimum Distance* parameter.
    - This determines the smallest wall segment.
    - Smaller values increase the number of points in the final dataset.

    - Larger values decrease the number of points but may miss small details in the cell boundaries.

14. Save the cell data.
    - 14.1. From the top menus, select the *Mesh* dropdown menu.
    - 14.2. Select *Mesh 1*, then *Export*.
    - 14.3. Choose *Cells* for the file type.
        - This creates a text file will coordinates of cell boundaries only.
        - The entire mesh data is not included.
    - 14.4. Click *OK*.
15. Save the mesh.
    - 15.1. From the top menus, select the *Mesh* dropdown menu.
    - 15.2. Select *Mesh 1*, then *Save*.
        - This creates a .mgxm file.
        - All of the mesh data is included.
        - This file can be used to re-load the mesh later.
    - 15.3. Click *OK*.

When errors are received while trying to create cells (step 12), there sometimes was a problem with the structure of the mesh. The following Python code was used to try to fix the problem. After running this code, the steps at 12 were used to build the cells again.

```
Mesh.Segment_Mesh(20000)
count = 0
while count < 2:
    try:
        Mesh.Make_Cells(1)
        break
    except:
        Mesh.Fix_Corners()
        Mesh.Smooth_Mesh(1)
```

```
        Mesh.Segment_Mesh(20000)
    count += 1
```

At this point the data is exported as a text file (as created in step 14). This file contains the coordinates of all the cell boundaries. This was used to locate the cells expressing KAN1 so that the edge of the meristem can be quantified.

#### 3.2.3.5 Identifying the Saddle Point

In cases when the SAM boundary was determined via the saddle point method, the following protocol was used. The file as generated at the end of section was open in the following Python script that turns the mesh into a set of z-values representing the height of the meristem at each point.

```
fi = open("filename.mgxm","r")
lines = fi.readlines()
fi.close()

data = []
for line in lines:
    items = line.split("\t")
    zvalue = items[4]
    data.append(zvalue)

fi = open("output.txt","w")
for d in data:
    line.write("%s\n" % (d))
fi.close()
```

This file was then imported into Matlab. The following Matlab notebook was run to extract the locations of the saddle points.

```
clear all;

% Read the CSV file with z-values
filename = 'output.txt';
im = csvread(filename)
```

```
% Calculate gradients field
[nr,nc]=size(im);
[dx,dy] = gradient(double(im));
[x y] = meshgrid(1:nc,1:nr);
u = dx;
v = dy;
imshow(im);
hold on
quiver(x,y,u,v)

% Estimate critical points
Cx=diff(Image,4,4); Cx(end+2,:)=nan;
Cy=diff(Image,4,4); Cy(:,end+2)=nan;
[i,j]=find( Cx.*Cy<=0);
```

The point with the negative curvature was determined to be the apex of the SAM. The closest identified saddle point was determined to be the nearest primordia crease. The Euclidean distance through 3D space from the saddle point to the apex was used as the size of the SAM.

### 3.2.4 Divergometer

To measure divergence angles "manually," a divergometer was used. The divergometer used here is a device designed and built by Arun Sampathkumar. It is a device designed to measure divergence angles around the shoot of Arabidopsis plants. It uses moving parts and a protractor to measure the angle. See figure 3.1 for more details.

Mature but still green plants were cut just above the rosette leaves using scissors. The plant was mounted in the divergometer using the clips. The protractor was rotated to line up with the two siliques to be measured. The angles was read off and recorded in a notebook. The data were transcribed into Excel, where distributions were plotted.

Figure 3.1: Divergometer used for measuring divergence angles and plastochon distances. Left panel shows the entire device. Right panel shows a closeup of the rotating protractor.

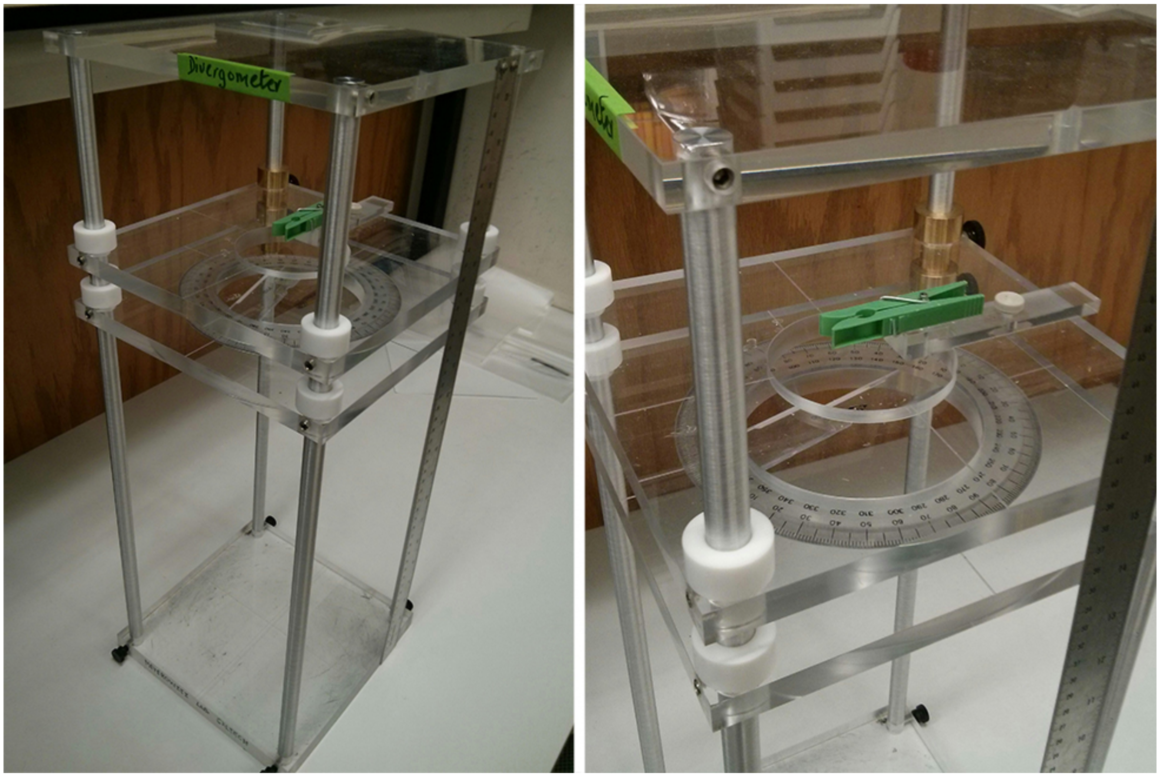

### 3.2.5 Tomography Photography

The shoots of plants grown in were cut off just above the rosette leaves with a pair of scissors. An orange bottle cap was turned upside down and filled with molten paraffin. Before the paraffin hardened the bottom of the shoot was submerged into the paraffin and held in place with a helping-hands device. After the paraffin hardened the cap with the plant was moved into a photography area.

The area had been set up with a black felt sheet to create a uniform background as seen in figure 3.10. Test patterns were printed out from PhotoModeler Scanner on an inkjet printer. The test petterns were cut out and taped to different locations on the black felt. A Nikon D80 camera with 35mm f/1.8 lens was mounted on a small tripod.

Six photographs were taken of each sample. The six photos were composed of three pairs of photos. Each pair was taken at the same angle but shifted horizontally by 10cm. One of the pairs was taken straight on and the other two pairs were taken at 45°to either side. The images were transfered to a computer via an SD card.

Figure 3.2: Photography strategy for tomographic 3D reconstruction. Six photographs are taken at three different angles. Each of the two photographs taken at the same angle are shifted 10cm perpendicular to the direction pointed by the camera.

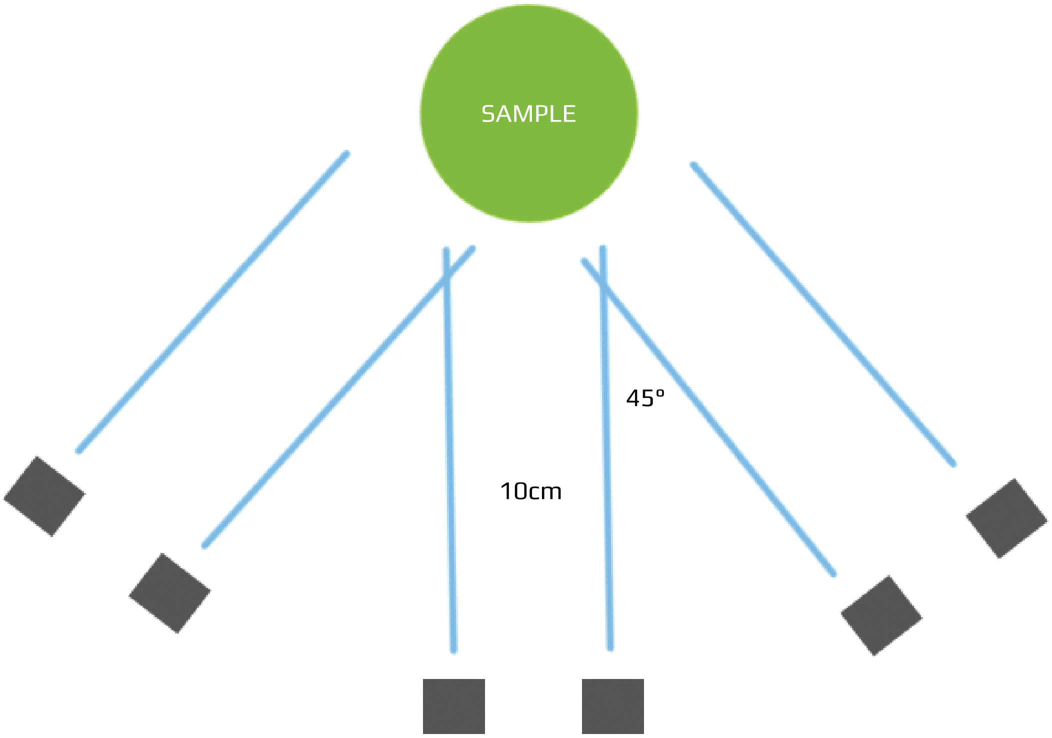

### 3.2.6 Tomography Software

Images collected as described in section were opened in the commercial software package called PhotoModeler Scanner v6.4. A calibration procedure was first run using six images of the test patters without any sample in the frame. This generated coordinates for the exact placement and orientation of each of the test patterns.

The six images of the sample were then loaded into PhotoModeler Scanner. Each image was processed to determine the location of the test patterns. Then a 3D model could be created. Once the model was finished being created, stray bits of mesh were removed manually using the touch-up tool. The 3D mesh was then exported for further processing in VTK format.

A custom software algorithm was developed to extract the divergence angles from the 3D model. This software was run on the VTK file and generated a series of divergence angles and platochrons in a text file. These numbers were then imported into Excel for further analysis.

## 3.3 Results

### 3.3.1 Meristem Size Via Fluorescent Markers

To measure the size of the shoot apical meristem, the edge of the meristem must first be defined as there is no clearly defined edge. One possibility is to use a fluorescent reporter driven by the promoter of a gene that is active around the region where we think the edge of the meristem might be. One candidate gene is KANADI1 (KAN1). KAN1 is thought to be expressed in a ring around the periphery of the SAM which would be useful.

A reporter was built (pKAN1::GFP-N7) by Marcus Heisler using the 5kb upstream promoter region of the KAN1 gene fused to a coding region for a nuclear localized GFP[57]. This construct was transformed into Arabidopsis thaliana ecotype Ler plants. The expression domain of this construct and the boundary of cells stained with FM4-64 were viewed using confocal microscopy. The images (Figure 3.3A) show a ring of expression around the periphery of the meristem in the first layer of cells in the epidermis and also one to two layers below that, depending on the exact location.

The region of KAN1 expressing cells is variable in that sometimes it flanks the primordia on the apical side, sometimes on the basal side, and sometimes on both. Initially, the locations of each nuclei were segmented using Fiji so exact measurements could be made in software. Depending

Figure 3.3: Segmenting KAN1 Expression. KAN1 expression forms a ring around the periphery of the meristem, primarily in the first epidermal layer but also in some deeper layers. In some parts of the SAM the KAN1 region is closer to the apex than other and the ring is broken in some regions. **A.** Maximum intensity projection of KAN1 expression in the shoot apical meristem. KAN1 labeled nuclei are shown in green. **B.** ImageJ segmentation of nuclei expressing KAN1 projected to a 2D plane.

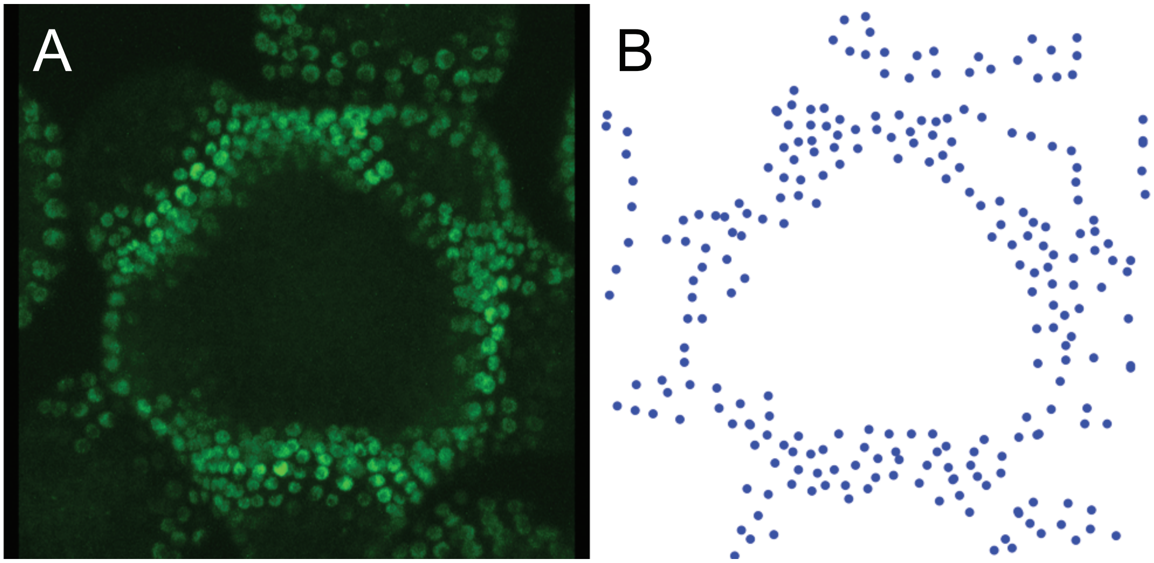

on the exact location in which we might measure from and the time the measurement is taken, the distance between the apex and that point can vary substantially(Figure 3.8), from 20$\mu$m up to 45$\mu$m or approximately the width if a flower primordium. This presents a problem for quantifying meristem sizes so a second approach was tested.

### 3.3.2 Meristem Size Via Topology

Using a geometric marker as landmark for measuring meristem size could excel over a fluorescent marker as the shape of the meristem is relatively stable whereas the KAN1 marker can be turned on and off in different regions through a dynamic process that is not understood. A new flower primordium is produced approximately every 12 hours so there will always be a crease in the meristem, a valley between the meristem and the nearest flower primordium, that is near the apex. In order to use this geometric feature as a landmark, I first need a computational method for mapping the topography of the meristem surface and extracting the 3D coordinates of the features of interest.

To generate a mesh representing the surface of the meristem, a confocal z-stack of the meristem stained with FM4-64 (lipophilic membrane marker) is taken. The z-stack is processed in the Mor-

Figure 3.4: The top layer of cells from a 3D confocal microsocopy z-stack mapped onto a surface generated from the cells in the image. Blue x's indicate maxima in the curvature and green o's indicate saddle points in the SAM topography. In order to determine the radius of the SAM, the distance between the maxima at the apex of the SAM and the nearest saddle point must be determined.

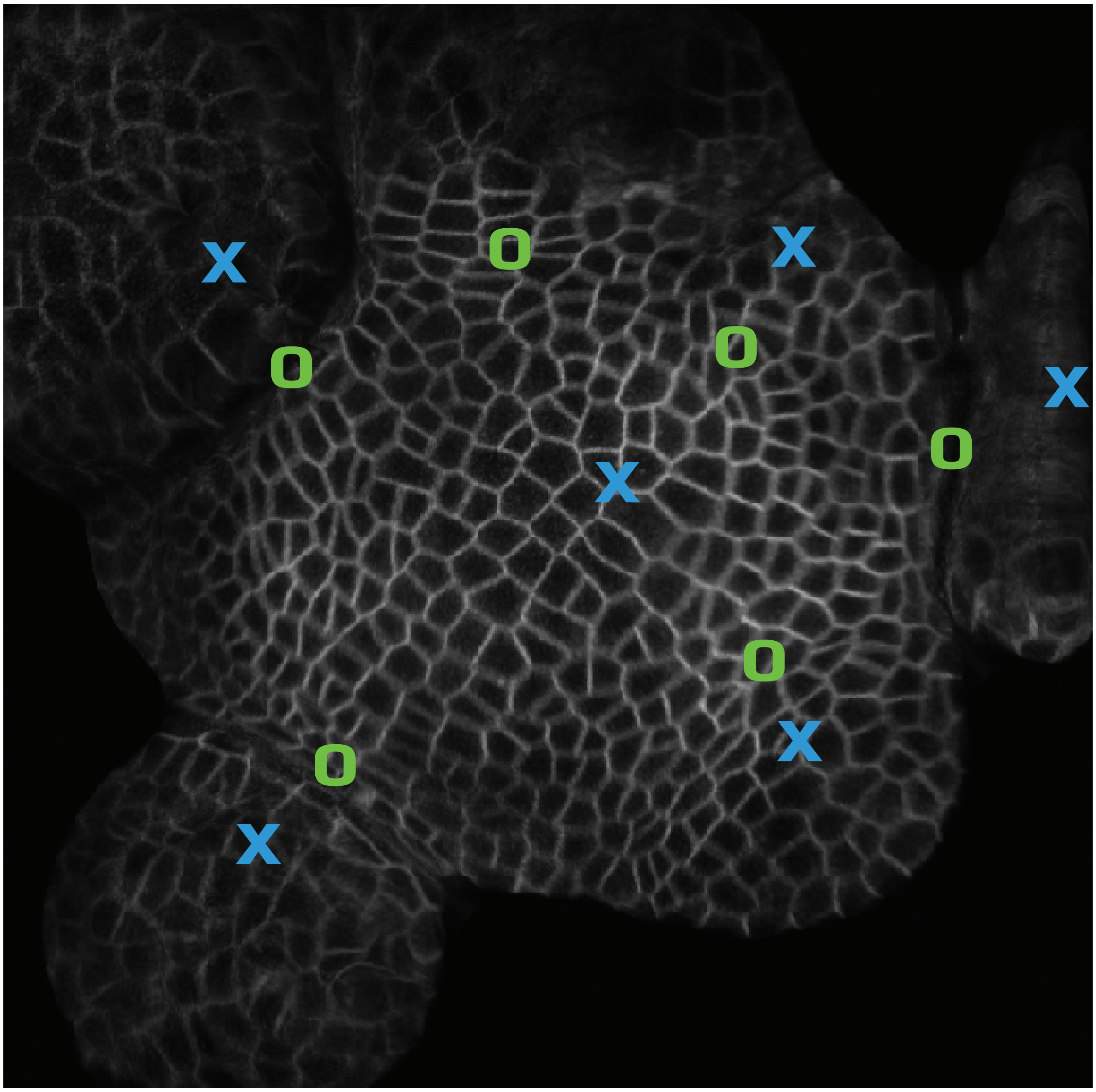

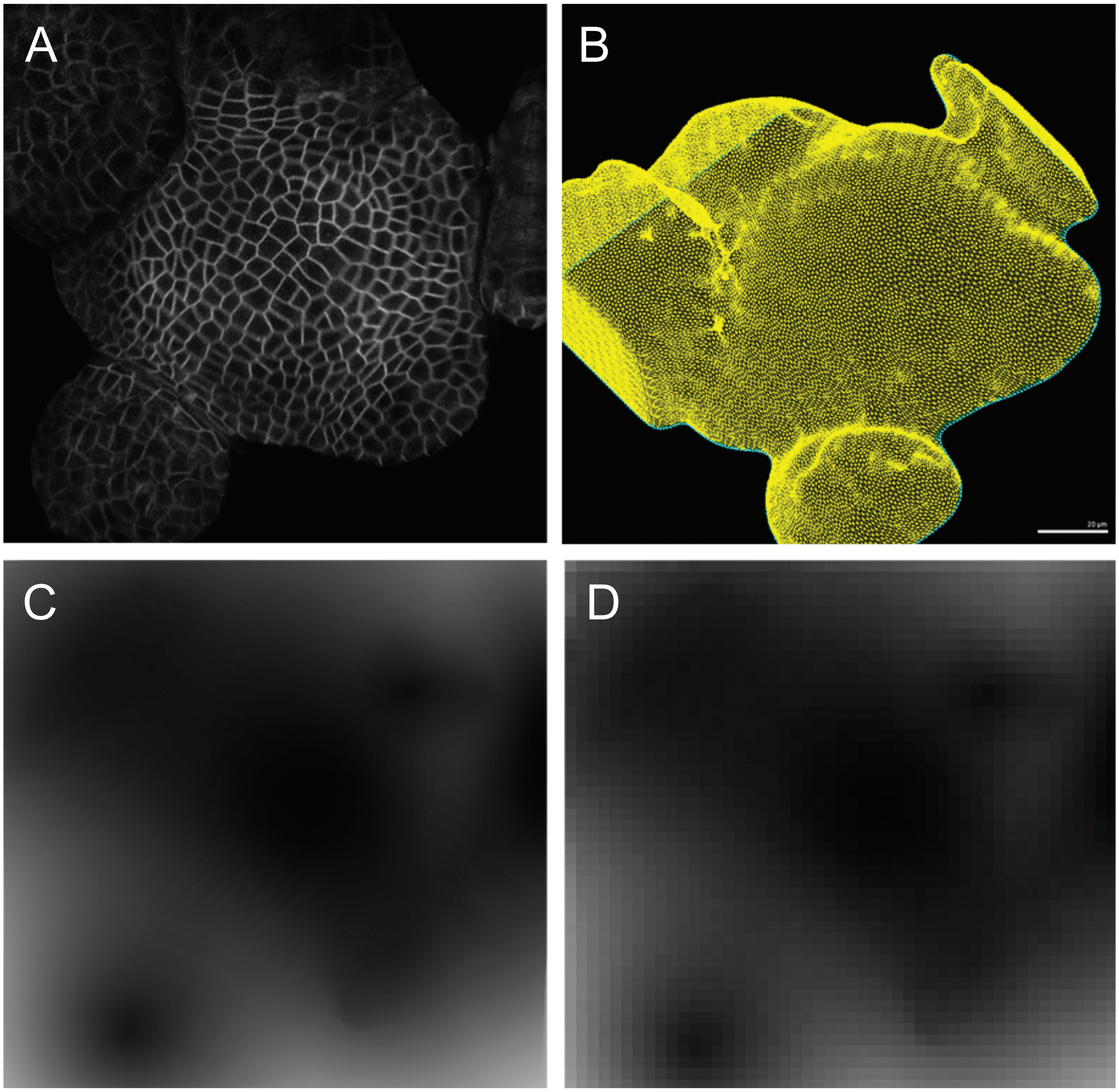

Figure 3.5: Starting with a z-stack of images from a confocal microscope, a heatmap of the height of the SAM is generated. **A.** 3D projection of the image data in MorphoGraphX. **B.** Mesh generated from the image data. **C.** High resolution heatmap generated from the mesh. 1 pixel for each pixel in the original image. The color is inverted so black areas represent higher z-values. **D.** Lower resolution heatmap generated using a reduction kernel.

phoGraphX software pipeline to extract the meristem volume, positions of cells and finally a surface mesh as shown in Figure 3.5 panels A and B. The mesh is then smoothed to remove all small variations. The z-coordinates of each node in the mesh are isolated using a custom software algorithm, described in Section 3.2.3.5. The resulting scalar matrix represents the height at each point and can be visualized with a heapmap (Figure 3.5C). Since that resolution heatmap is not necessary for finding stationary points, the matrix is shrunk with a reduction kernel to a 50 by 50 matrix (Figure 3.5D). This matrix is then used for finding stationary points.

To find the stationary points a gradient field is first calculated (Figure ). Since a true gradient can only be calculated on a continuous function, the field is numerically estimated with a short Matlab routine.

```
Cx=diff(Image,4,4); Cx(end+2,:)=nan;
Cy=diff(Image,4,4); Cy(:,end+2)=nan;
[i,j]=find( Cx.*Cy<=0);
```

This finds points where the slope crosses the zero line which is true for all stationary points, as in Figure 3.7. Each point is then classified as either being a maximum, minimum, or saddle point. The apex of the meristem is defined by the maxima nearest to the center of the image. This is dependent on the specimen being positioned in the focal plane properly during imaging so that the apex is actually the center most maximum. The saddle points represent the places where the primordia meet the meristem.

From here, the size of the meristem can be measured by looking at only the center most maximum and the nearest saddle point. These two stationary points are then mapped back to the original surface mesh in 3D. The distance between these two points on the mesh is then calculated using Dijkstra's algorithm[58]. This algorithm finds the shortest path between two nodes in a graph by making a tree of the connectivity of the nodes starting from one node and throwing out longer paths to any node as it proceeds. The distance between the two points in 3D along the surface of the meristem is calculated by adding up the length of each edge in the shortest path. This method provides a way to measure meristem size in a repeatable, although time consuming, way.

### 3.3.3 Comparison of Meristem Measurement Methods

To compare the merits of both methods, 20 plants of Ler ecotype containing the pKAN1::GFP-N7 construct were grown. The meristems were dissected and stained with FM4-64 and confocal z-stacks

Figure 3.6: Gradient map calculated from the heatmap in figure 3.5D. Gradient is calculated from the scalar field using a local approximation method in Matlab. A topological map, also generated from the same heatmap, is overlaid on top of the gradient vector field.

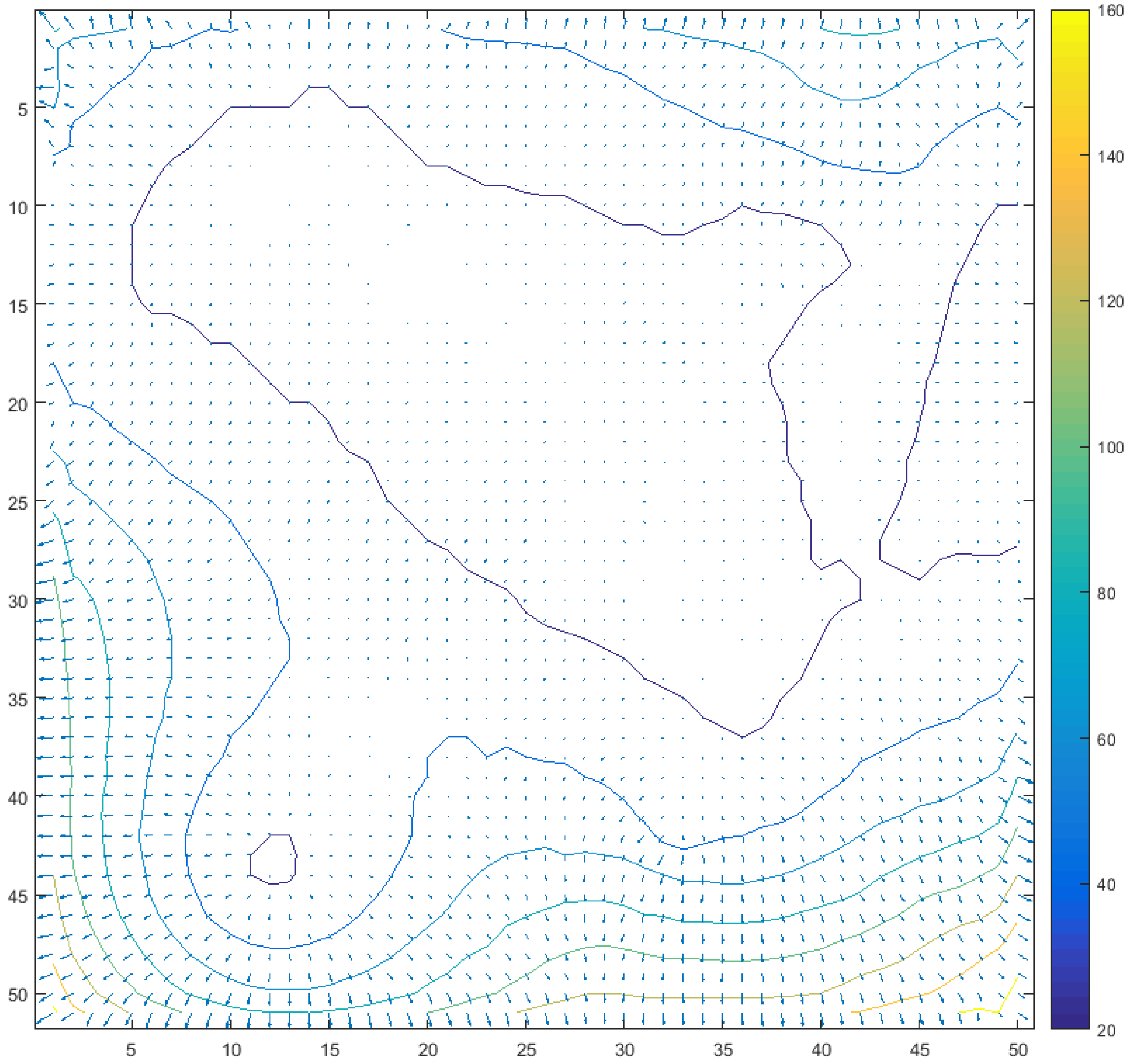

Figure 3.7: Critical Point Map. **A.** All critical points plotted on the topological map, including both maxima and saddle points. Lines represent the height of the tissue. **B.** Two critical points of interest of interest overlaid on meristem projection. Lowest point is the maximum at the apex of the SAM. Highest point is the saddle point nearest the apex (the lower point).

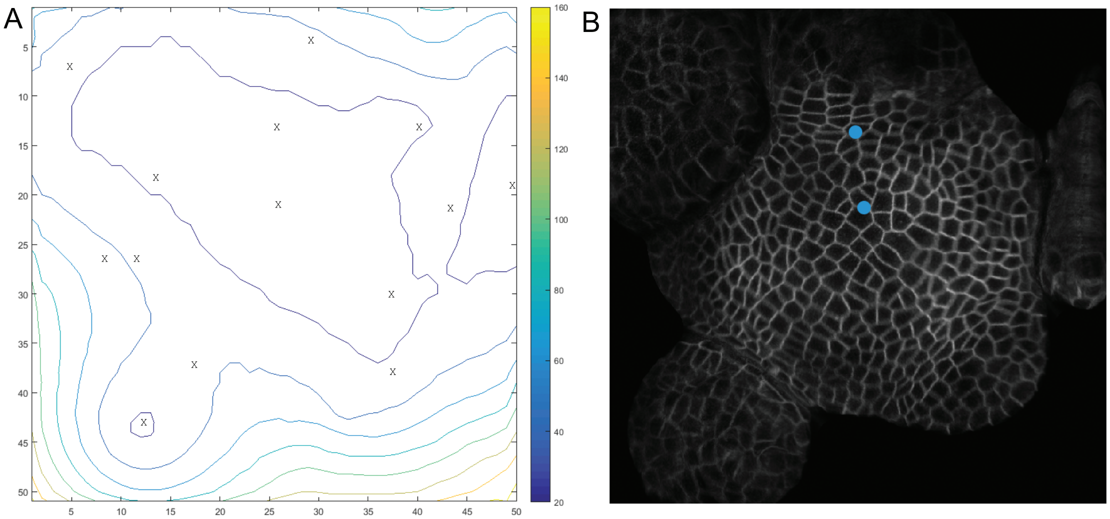

were taken of each meristem. Each image was processed with both methods. The resulting data in Figure 3.8 shows that both methods produce almost the same mean radius (32.5$\mu$m and 34.1$\mu$m), although this could be coincidental. But the variability using the fluorescent method is much higher, 6.8$\mu$m vs 2.2$\mu$m standard deviation.

There is a possibility that given a sufficiently large sample size the means of both methods will still remain nearly the same. In that case either method could be used if the mean value is all that matters. But the closeness of the means could be a coincidence. Given that the geometric method produces a much lower variability I am inclined to trust this method to produce results that represent reality more accurately and precisely. The geometric method takes significantly more time to complete each sample at approximately 5 hours compared to approximately one hour with the fluorescent marker method. But given the increase in apparent accuracy it is a worth-wile trade off. The rest of the measurements of meristem size in this study were done with the geometric method.

### 3.3.4 Measuring Phyllotaxis with 3D Tomography

Before starting this study my standard method for measuring phyllotaxis divergence angles was with a divergometer (see Figure 3.1). The accuracy of this method is dependent on the best judgement of

Figure 3.8: Comparison of SAM sizes of wild type plants using the fluorescent marker (KAN1) method and the saddle point method. 20 plants in the sample. Both methods produce very similar mean values. The fluorescent reporter method produces a much higher variability than the saddle point method so it was not used in the rest of this study. Error bars represent one standard deviation.

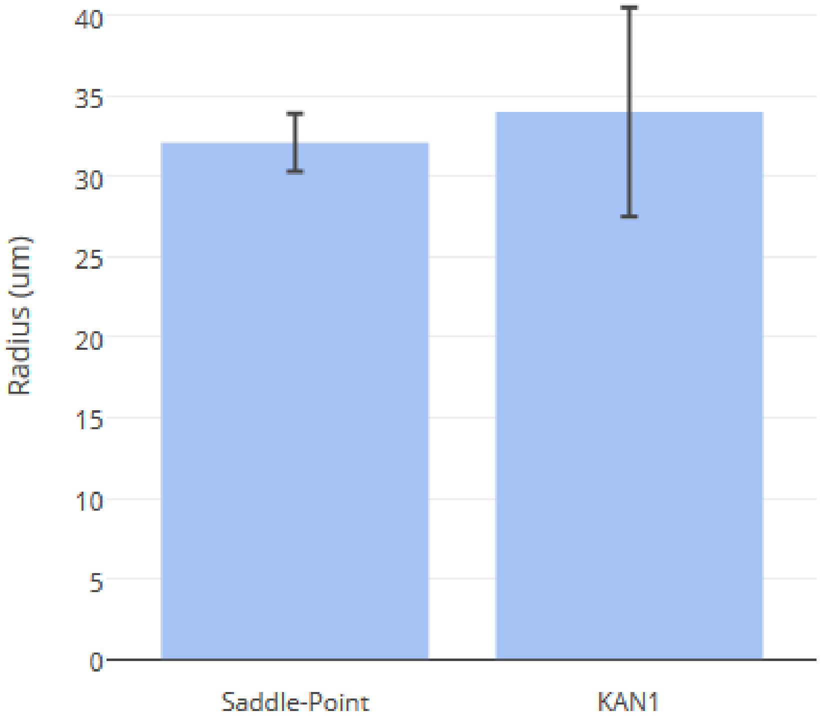

Figure 3.9: Comparison of the radii of SAMs within wild type and various mutant lines. The saddle point method was used rather than the fluorescent marker method. Many of these mutants show a deviation from the wild type radius. Some mutants have a wider variation, *wig-2* in particular, not due to measuring methodology but due to actual differences between individual specimens.

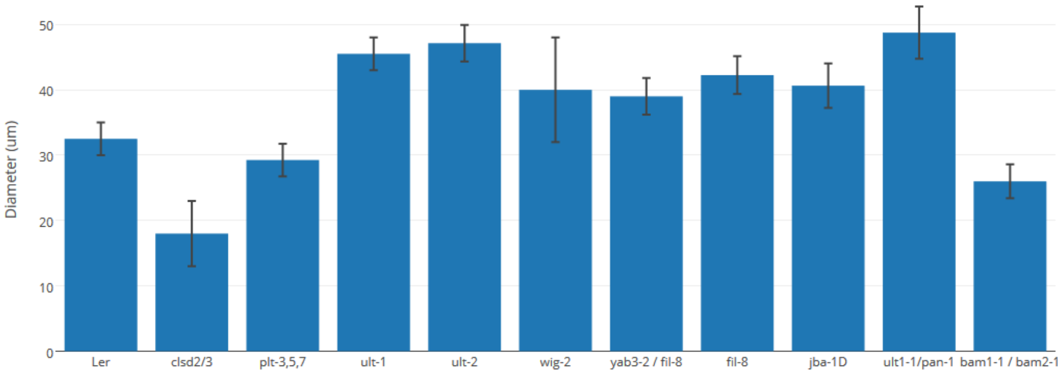

Figure 3.10: A plant mounted in a paraffin base and displayed in front of black felt for photography. The strips of paper next to the specimen are reference targets used by the tomography software to determine the orientation of the camera and the specimen. The area outside of the reference targets is ignored.

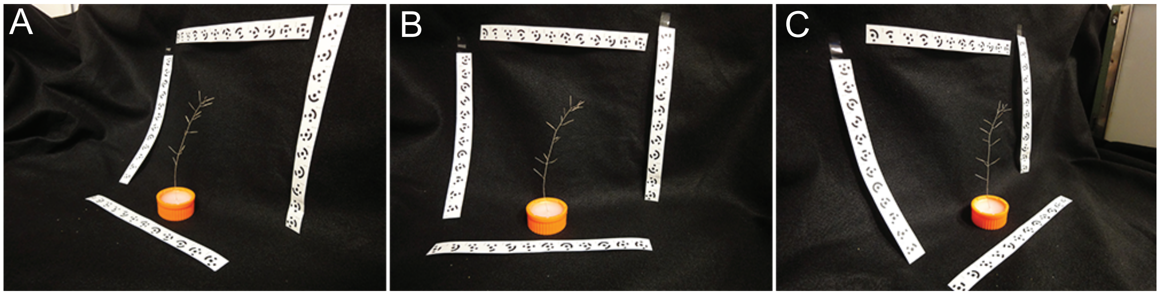

the operator when measuring the divergence angles on the protractor. Additionally, it requires a lot of tedious work and about 45 minutes per plant. To make this process more repeatable and accurate I explored using 3D optical tomography as an alternative method to the divergometer.

The tomography software Photomodeler Scanner was the primary software used. I generated optical reference targets which are unique circular patterns that can be recognized by the software to determine the location of the camera between each photograph. Each plant was photographed six times from three different angles (Figure 3.2). The images were loaded into Photomodeler Scanner and a 3D triangular mesh model was generated. These meshes were edited in MeshLab to remove any extraneous object such as the base used to hold the plant in place and any background objects that were picked up by the software. Once the mesh was devoid of any objects besides the plant, the new mesh was exported. The clean mesh was then processed with a custom algorithm which identified the shoot vs siliques and measured divergence angles between siliques.

This method produces results very similar to those of the divergometer. Figure 3.12 shows the phyllotaxis sequence for a single plant processed measured by both the divergometer and optical tomography. The divergence angles are often with 5°. Consequently I am confident in the accuracy of the optical tomography method but it has drawbacks. While taking the pictures of a single plant take about two minutes, the processing can take hours per plant. This is dependent on how much editing the mesh needs and how easily the custom software can identify the siliques. In situations where a silique sticks above the top of the shoot, the software will identify the silique as the shoot and the shoot as a silique which means the software must be manually forced to change its identifications. This is time consuming to the point where the divergometer measurements are quicker. Since both methods produce comparable numbers and the divergometer takes less time, the divergometer is the preferred measurement method.

Figure 3.11: An example of the software used to tomographically construct a 3D model of a plant, PhotoModeler Sanner v6.4. Raw photographs are loaded into the software. The software used the reference targets to align the images and generate a 3D model, shown in the top right panel. The color data can be mapped back to the surface of the model. In this case, the model was exported as a VTK mesh for further analysis.

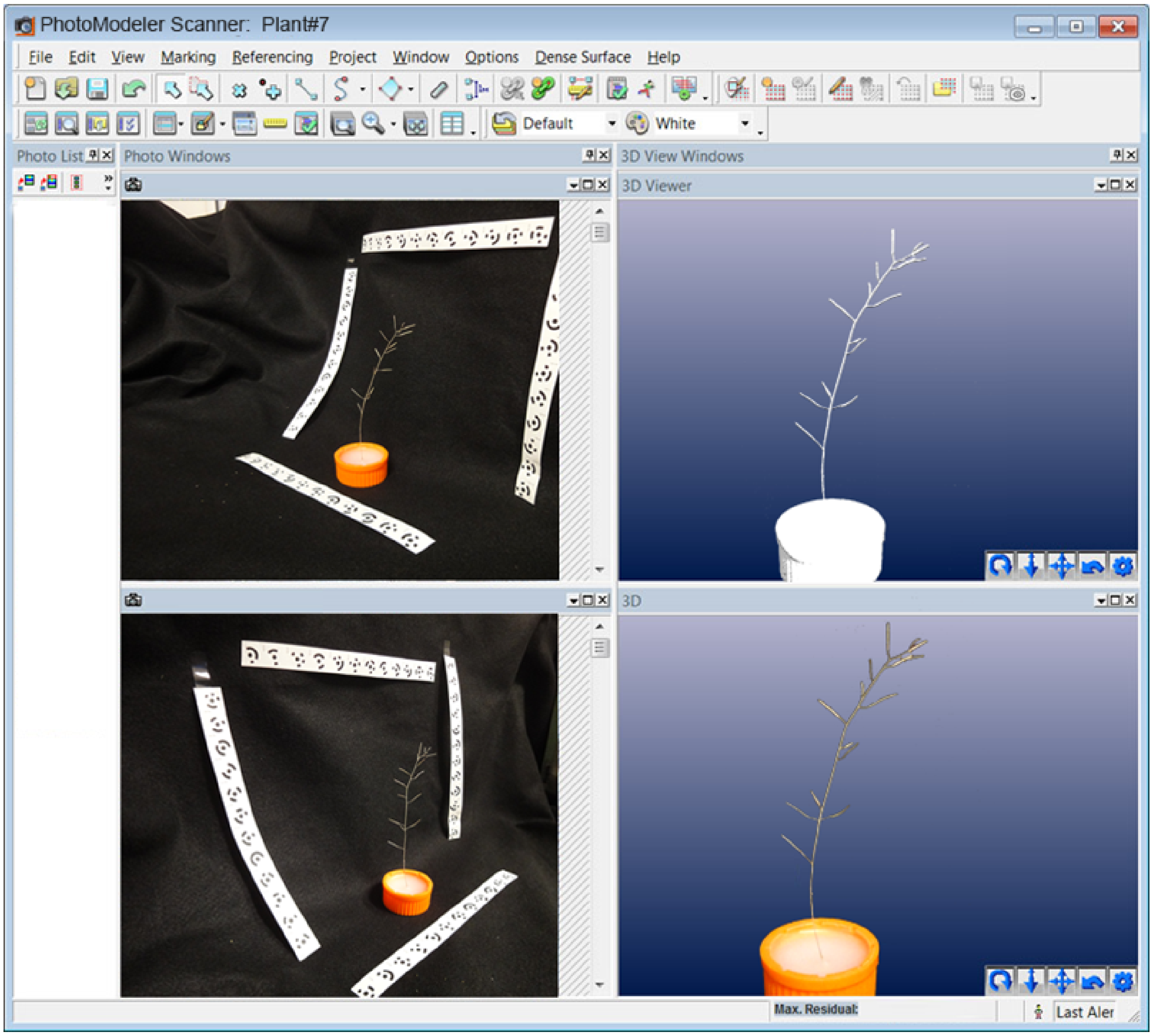

Figure 3.12: Comparison of data produced using two methods on the same sample. Orange shows the sequence of divergence angles produced using photographic tomography. Blue represents the same sequence as measured with a divergometer. Both methods produce very similar numbers, often within 5°.

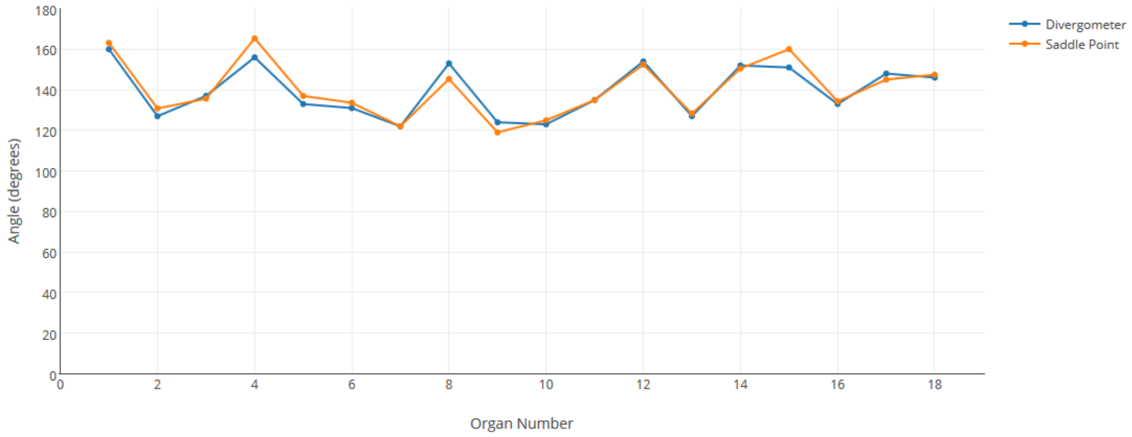

### 3.3.5 Mutant Phyllotaxis Comparison

As previous work has suggested, the size of the meristem plays a part in determining the observed divergence angles, at least in purely physical models[12, 13, 14, 15]. If this is true then altering the size of the meristem should result in altered divergence angles. To determine if there is a correlation between meristem size and phyllotaxis divergence angles I measured these two traits in 11 different genetic lines, which are listed in table 3.1. For measuring the meristem size I used the geometric method and for measuring phyllotaxis I used the divergometer.

The mean meristem radius of the various mutants is highly variable between the selected lines (Figure 3.2). This is not surprising as they were selected because the literature on these lines suggested they had meristem sizes different than wild type. The mean divergence angles on the other hand did not change much. For example, the bam1-1 / bam2-1 double mutant had a mean meristem radius of 26$\mu$m but the mean divergence angle is 134°, which is only a few degrees away from the "golden angle" of 137.5° and only 1° away from what wild type was measured to be in this study. The same goes for lines with larger meristems and those with smaller meristems.

The only obvious exception to this is the clsd2/3 line which had a mean divergence angle of 188°. The meristem of this line is very small, produces fewer flowers than most others, and emerges in a highly irregular pattern. In wild type plants, once the phyllotaxis spiral is initiated going either clockwise or counter clockwise and each successive flower follows the same handedness. Sometimes

Table 3.1: Genetic lines used in this study.

| **Mutant** | **Note** |
|---|---|
| Ler | Wild type |
| csld2/3 | Cell wall biosynthesis |
| plt-3,5,7 | Transcription factor |
| ult-1 | Transcription factor |
| ult-2 | Transcription factor |
| wig-2 | Farnesyl-transferase |
| yab3-2 / fil-8 | Transcription factors |
| fil-8 | Transcription factor |
| jab-1D | Transcription factor |
| ult-1 / pan-1 | Transcription factors |
| bam1-1 / bam2-1 | Receptor kinases |

the handedness switches in the middle of growth but the switch is clear because all the flowers after the switch have divergence angles close to 137° measuring the other direction. In csld2/3 mutants the handedness switches periodically and it is not easy to determine if there has been a switch because the pattern is so erratic to begin with. Many flowers emerge with a 180° divergence angle, which also makes determining the handedness of the phyllotaxis pattern difficult. There is certainly an element of subjectiveness when it comes to determining which direction to measure the angles in this line. The scatter plot in Figure 3.15 shows there is not much correlation between mean meristem radius and mean divergence angle.

Looking at the distributions of the divergence angles in each line tells a different story. While many of these lines have a very similar mean divergence angle, the distribution varies much more (Figures 3.13, 3.14 and 3.15). In wild type there is a narrow distribution around the mean with a few points up in the higher values. In csld2/3 there is actually two peaks; one around 200° and another around 130°. The lines with larger meristems tend to have a wider distribution around the mean with more outliers in the higher value range compared to wild type.

## 3.4 Discussion

The plyllotaxis pattern of plants has been admired and studied for centuries. Early studies were teleological or descriptive in nature and any speculations about the underlying mechanism were arrived at from a top-down approach. It has not been until recently that we gained enough understanding of the molecular mechanisms to make sense of these patterns from first principles. It has been advances in our understanding of polar auxin transport that have lead the way towards understanding this

Figure 3.13: Left column: Distributions of divergence angles for each genetic line, binned in groups of 10°. Right column: A single example of the sequence of divergence angles for a single plant in each line. Plots show only the first 16 siliques to keep the axes equal.

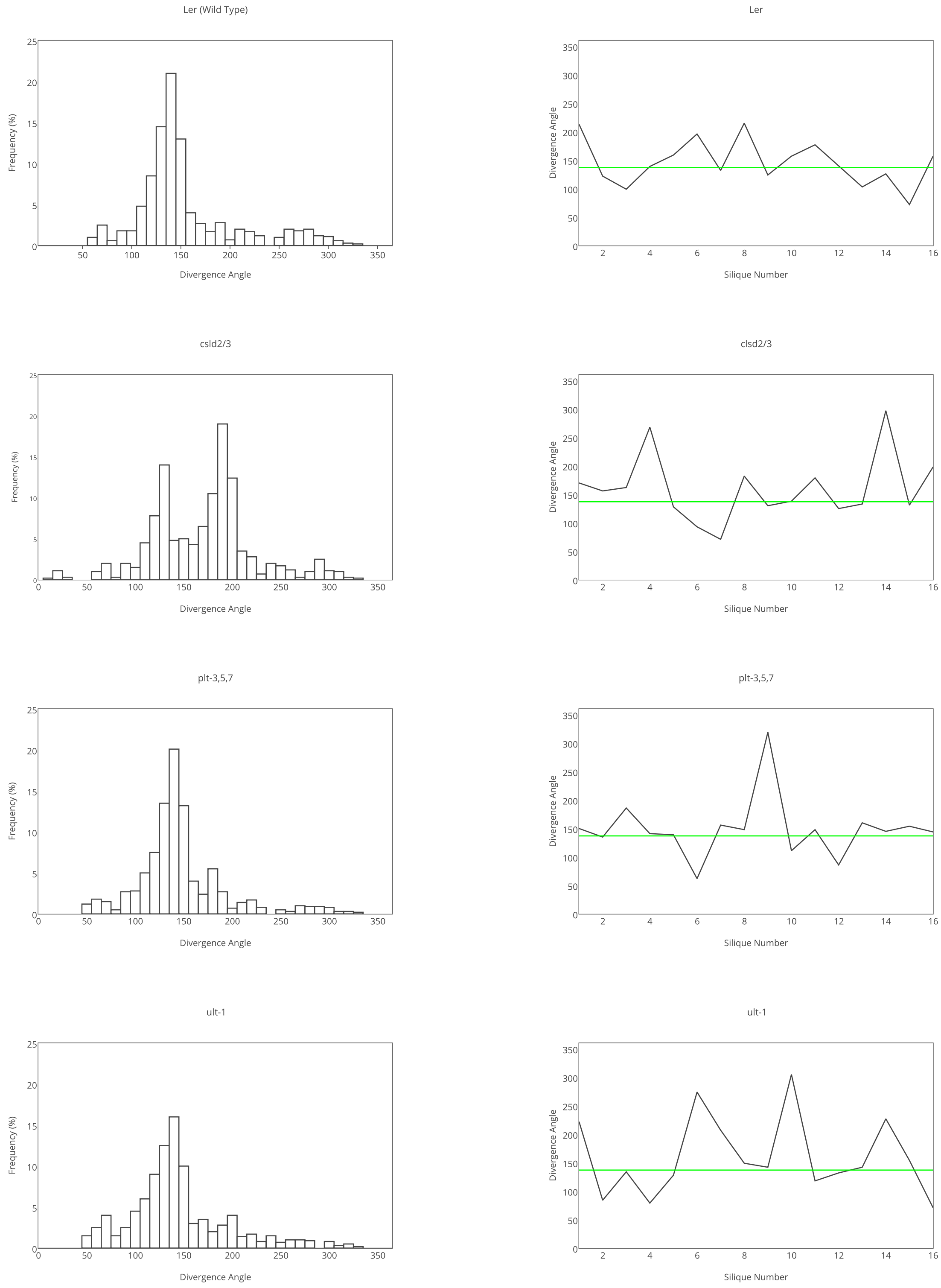

Figure 3.14: Left column: Distributions of divergence angles for each genetic line, binned in groups of 10°. Right column: A single example of the sequence of divergence angles for a single plant in each line. Plots show only the first 16 siliques to keep the axes equal.

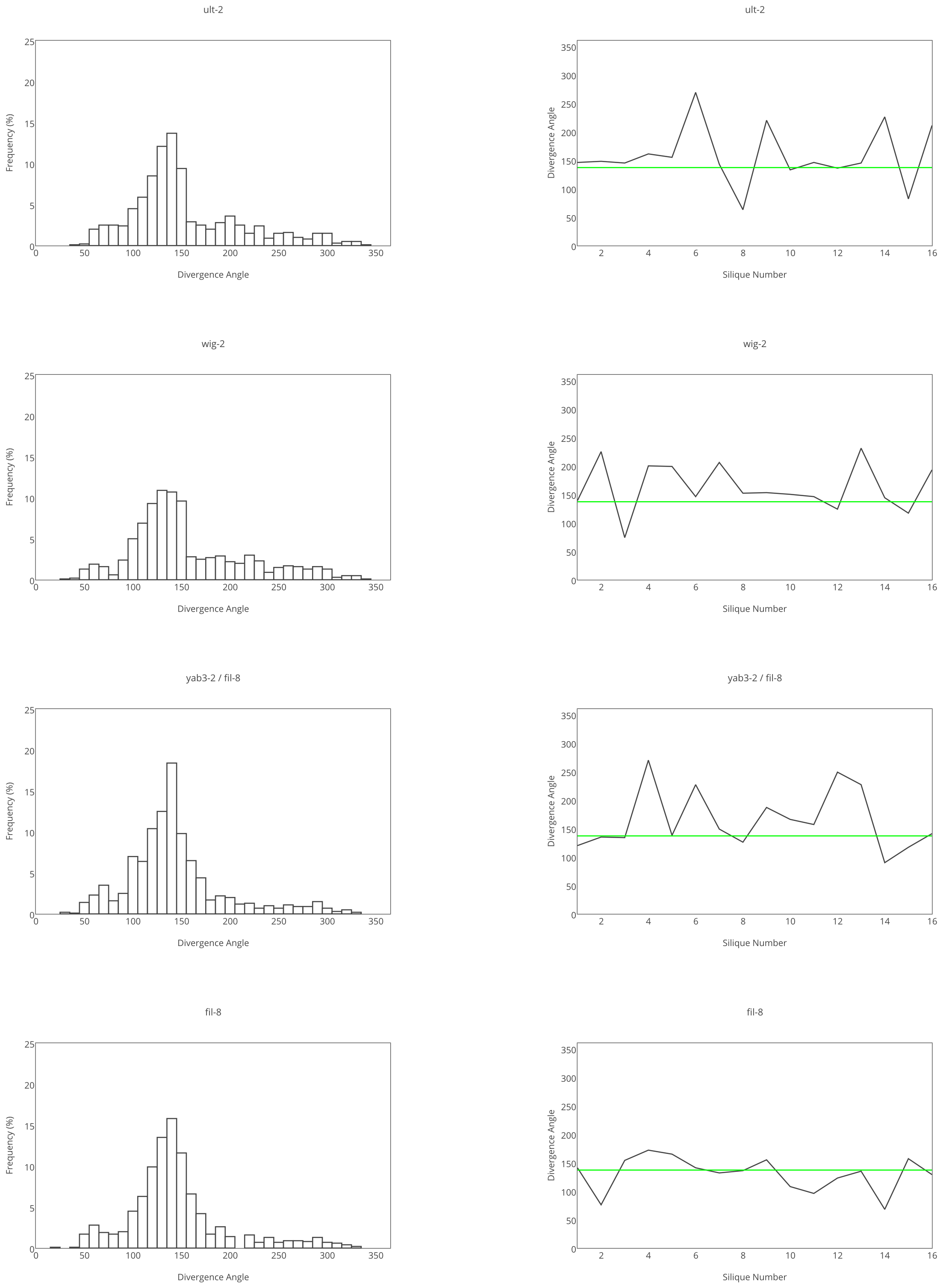

Figure 3.15: Left column: Distributions of divergence angles for each genetic line, binned in groups of 10°. Right column: A single example of the sequence of divergence angles for a single plant in each line. Plots show only the first 16 siliques to keep the axes equal. Bottom: Scatter plot showing the relationship between the mean meristem radius and the mean divergence angle.

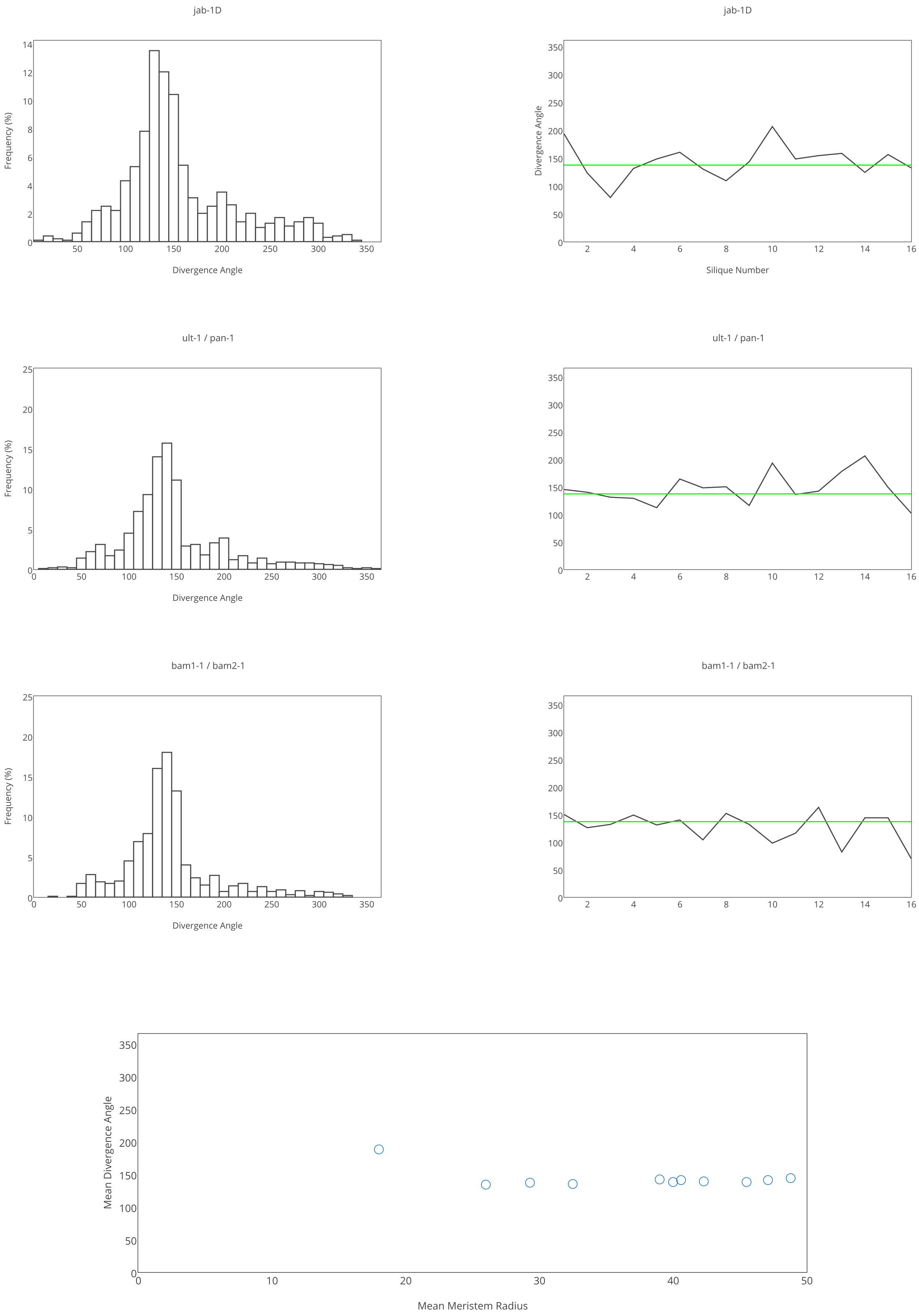

Table 3.2: Mean divergence angle and SAM size Comparison. SAM radius was measured using the saddle-point method rather than the fluorescent marker method. Values are in micrometers. Divergence angles were measured using the divergometer rather than tomography.

| **Mutant** | **Mean Divergence Angle (°)** | **SAM Radius ($\mu$m)** |
|---|---|---|
| Ler | 135 | 32.5 |
| csld2/3 | 188 | 18 |
| plt-3,5,7 | 137 | 29.3 |
| ult-1 | 138 | 45.5 |
| ult-2 | 141 | 47.1 |
| wig-2 | 138 | 40 |
| yab3-2 / fil-8 | 142 | 39 |
| fil-8 | 139 | 42.3 |
| jab-1D | 141 | 40.6 |
| ult-1 / pan-1 | 144 | 48.8 |
| bam1-1 / bam2-1 | 134 | 26 |

remarkable phenomenon.

I sought to make sense of this phenomenon first through computer models based on our first principles, then through experiments to probe the predictions made by those models. Using a multi-scale model run on a distributed computing platform I determined that the model parameters most likely to have an effect on the overall phyllotaxis pattern were the size of the cells and the size of the tissue through which the polar auxin transport acts. In the last chapter I experimentally explored the effects of cell size and in this chapter I similarly explored the effect of tissue size on phyllotaxis. To this end, I compared the sizes of SAM with the phyllotaxis patterns in mutants with altered SAM sizes.

In order to accurately quantify the sizes of SAM I explored different measurement methods. The difficultly with measuring the SAM arises from the fact that the SAM does not have a clear boundary. Initially I tired using a fluorescent reporter, the KAN1 promoter driving a nuclear localized GFP, to delineate the edge of the SAM. The KAN1 gene is expressed around the periphery of the SAM and so it theory would make a good marker for the SAM boundary. It would also be relatively simple to quantify using specialized software since the fluorescent nuclei are simple to segment from the cell boundaries. I developed a software work-flow using MorphoGraphX and a small amount of custom software to (1) segment the cells in the SAM and these nuclei, (2) assign cells to either "boundary" or "not boundary" based on the segmented nuclei, and (3) measure the distance in between the boundary region.

This technique, while relatively simple and convenient, had the problem of a high variability. The region of KAN1 expression flip-flops around the floral primordia. At some points around the SAM it travels in between the SAM and the primordia, at other points it travels around the outside of the primordia, and sometimes it travels around both sides. Since this means that KAN1 does not form a circle around the SAM, picking a single point to measure from is arbitrary and leads to the variability.

To combat this problem, I created a second measurement method based on the topology of the SAM. New primordia form a crease in the surface, or in mathematical terminology, a "saddle point." Since the newest primordia is always approximately the same distance from the center of the SAM across multiple samples and time points, this turned out to be a more reliable method. Compared to the fluorescent reporter method, this method had about 25% as much variability between multiple measurements of different SAMs of the same genetic background. The mean value of the topological method was within 2$\mu$m of the fluorescent method.

The second aspect of this study was to measure phyllotaxis angles. In an attempt to make more reliable and repeatable measurements compared to using a divergometer, I developed a photographic technique and software work-flow for generating 3D models of plants and extracting divergence angles from those models. The technique works and makes beautiful 3D pictures but in practice does not increase the repeatability very much. It also takes about two or three times as long to process each plant. While taking measurements using a divergometer requires patients and squinting, the tomography method transfers most of the tedious work to editing 3D meshes on the computer. The time trade-off does not make sense so ultimately I fell back on the divergometer for all my measurements.

The results of comparing meristem size with phyllotaxis pattern show that the mean divergence angle is relatively stable even when the SAM diameter increases 87% (bam1-1/bam2-1 26$\mu$m, ult-1/pan-1 48.8$\mu$m). Ostensibly this is in contradiction to the model which predicted SAM size to greatly effect phyllotaxis. But the mean divergence angle is not the only metric here. Looking at the distribution of the divergence angles tells a more complex story.

Plants with larger or smaller SAMs than wild type show a wider distribution, or more particularly, a greater quantity distant outliers. So, to a degree, the meristem size is effecting the phyllotaxis, if we assume the correlation is a causal relationship.

One explanation for the lack of diversity in observed phyllotaxis patterns is that phyllotaxis is multistable and we haven't probed a large enough range of SAM sizes to observe the other stable states. In this explanation phyllotaxis is not a gradient and has only a handful of possible states, which *is* corroborated by the model. In order to see the other states we might need to tweak the geometry of the SAM more. This is evident in the csld2/3 mutant which has a mean SAM diameter of 18$\mu$m, the smallest of the mutants considered here, and often produces and alternate phyllotaxis pattern.

Another explanation for the lack of diversity in observed phyllotaxis patterns is that the plant compensates for the altered SAM size in other ways. This is apparent in cell-size mutants (chapter 2). Plants with cells four times as large should have a phyllotaxis pattern similar to csld-2/3 mutants, which have SAMs with approximately one fourth the area as wild type. But those large cell mutants have wild type phyllotaxis. They make up for their larger cells with larger meristems which, if you believe the transport-limited model from chapter 2, makes the meristem the same size from an auxin molecule's point of view. While the meristem-size mutants considered here don't exhibit changes in cell size, one could imagine other aspects of the plant changing to compensate.

This brings up the question of why do plants have such tightly regulated phyllotaxis patterns. One potential answer that I am suggesting is that it's a matter of coincidence. The underlying mechanisms controlling phyllotaxis as proposed in this work are dependent on cell size and tissue size. This connection could have arose purely coincidentally. Since cell size and tissue size are two things that are very tightly regulated in multicellular organisms with multiple layers of redundancies, phyllotaxis can piggy-back on this robustness and become a robust process itself. Robust biological systems are often thought to have arisen through an evolutionary need where individuals expressing a phenotype outside of a narrow range are less fit. For example, individuals with a more loosely coordinated cell cycle may be less fit due to incomplete chromosome replication. But I am proposing that in this particular case a robust phyllotaxis patterning system is not evolutionarily important and arose as a matter of coincidence merely borrowing the robustness of the cell cycle.

Another outstanding question is why 137.5°. There are plenty of proposed answers to this question ranging from the teleological to the numerological. Based on the first principles presented in this work, it appears the answer is that auxin maxima act in a way similar to the inhibitory fields proposed by Alan Turning[11] where organ primordia give off a compound that diffuses through the tissue and inhibits the formation of other primordia in the surrounding region. We now know that the signaling molecule is actually a *positive* regulator rather than a negative one and that it moves *towards* the primordia instead of away. Nevertheless, the outcome is the same and successive primordia are spaced as far from existing primordia as possible, which leads to a scenario where the primordia are optimally spaced with as little undifferentiated tissue as possible, similar to the conclusions of Douadny and Couder[13]. Successive golden angles (137.5°) also lead an optimal packing scenario around the circumference of a circle. So the connection between organ formation and the golden angle (and subsequently, Fibonacci series) is coincidental in that they both lead to optimal spacing around a circle.

One might suggest that this particular spacing regime is actually an evolutionary feature and polar auxin transport evolved to move auxin "up the gradient" to make leaves optimally packed, providing the plant with a particular fitness. Plenty of people have noticed that optimal spacing of leaves leads to optimal sunlight collection or optimal raindrop collection. None of these explanations make sense. Sunlight capture is very rarely the limiting factor in growth. Nutrients like water, nitrogen, phosphorous, or potassium are in smaller supply. If photosynthesis was the limiting factor, plants could have evolved to capture a larger portion of the spectrum or evolved a more efficient RuBisCO enzyme. If optimally spaced leaves were important for water collection then desert plants should all exhibit the same optimal phyllotaxis pattern but this is not the case.

I am not suggesting that phyllotaxis patterning is completely inconsequential to the plant. In an extreme example, imagine all of the leaves developing on one side of the plant with divergence angle 0°. In this case the meristematic tissue on one side would all develop into leaves while the tissue on the opposite side would all form internode tissue. During shoot bolting this would cause the shoot to severely bend as one side would grow at a much faster rate than the side with the leaves, leading to major morphological problems. This would most likely be evolutionarily disadvantageous. So having a mechanism to prohibit primordia from forming near existing primordia prevents disastrous situations like this from arising and coincidentally leads to Fibonacci spiral patterns.

Of course, this too is speculation and partially teleological. To me it seems to be the simplest explanation given the evidence we have about the underlying mechanism. But our current models are not without limitations. More could be done to understand mechanical force propagation and sensing in the meristem. Our computer models will have to unify our current understanding of polar auxin transport with dynamic tissue growth and new knowledge of cellular and meristem mechanics in order to make progress in this field. Ultimately this will lead to greater understanding of both the molecular scale processes and the overall morphogenesis and development of plants.

# References

[1] I Adler. “A History of the Study of Phyllotaxis”. In: *Annals of Botany* 80.3 (Sept. 1997), pp. 231–244. ISSN: 03057364.

[2] Johann Wolfgang von Goethe. “Über die Spiraltendenz der Vegetation”. In: *Versuch die Metamorphose der Pflanzen zu erklären*. Gotha: Bey Carl Wilhelm Ettinger, 1790.

[3] W Hofmeister. *Allgemeine Morphologie Der Gewachse*. Leipzig: Wilhelm Engelmann, 1868.

[4] Simon Schwendener. *Mechanische Theorie der Blattstellungen*. Leipzig: Wilhelm Engelmann, 1878.

[5] Arthur H Church. *On the relation of phyllotaxis to mechanical laws*. London: Williams & Norgate, 1904.

[6] Mary Snow and R. Snow. “Experiments on Phyllotaxis. I. The Effect of Isolating a Primordium”. In: *Philosophical Transactions of the Royal Society of London. Series B* 221 (1932), pp. 1–43.

[7] M. Snow and R. Snow. “Experiments on Phyllotaxis. II. The Effect of Displacing a Primordium”. In: *Philosophical Transactions of the Royal Society B: Biological Sciences* 222.483-493 (Jan. 1932), pp. 353–400. ISSN: 0962-8436.

[8] M. Snow and R. Snow. “Experiments on Phyllotaxis. Part III. Diagonal Splits through Decussate Apices”. In: *Philosophical Transactions of the Royal Society B: Biological Sciences* 225.519 (May 1935), pp. 63–94. ISSN: 0962-8436.

[9] C. W. Wardlaw. “Organogenesis in Ferns: Evidence Relating to Growth centers and Physiological Fields”. In: *Proceedings of the Linnean Society of London* 162.1 (Oct. 1950), pp. 13–18. ISSN: 03700461.

[10] J. C. Schoute. “Beitrage zur Blattstellunglehre. I. Die Theorie”. In: *Recueilde Travaux Botániques Néerlandais* 10 (1913), pp. 153–339.

[11] A. M. Turing. “The Chemical Basis of Morphogenesis”. In: *Philosophical Transactions of the Royal Society of London. Series B, Biological Sciences,* 237.641 (1952), pp. 37–72.

[12] S. Douady and Y. Couder. “Phyllotaxis as a physical self-organized growth process”. In: *Physical Review Letters* 68.13 (Mar. 1992), pp. 2098–2101. ISSN: 0031-9007.

[13] S. Douady and Y. Couder. “Phyllotaxis as a Dynamical Self Organizing Process Part I: The Spiral Modes Resulting from Time-Periodic Iterations”. In: *Journal of Theoretical Biology* 178.3 (Feb. 1996), pp. 255–273. ISSN: 00225193.

[14] S. Douady and Y. Couder. “Phyllotaxis as a Dynamical Self Organizing Process Part II: The Spontaneous Formation of a Periodicity and the Coexistence of Spiral and Whorled Patterns”. In: *Journal of Theoretical Biology* 178.3 (Feb. 1996), pp. 275–294. ISSN: 00225193.

[15] S. Douady and Y. Couder. “Phyllotaxis as a Dynamical Self Organizing Process Part III: The Simulation of the Transient Regimes of Ontogeny”. In: *Journal of Theoretical Biology* 178.3 (Feb. 1996), pp. 295–312. ISSN: 00225193.

[16] F. J. Richards. “Phyllotaxis: Its Quantitative Expression and Relation to Growth in the Apex”. In: *Philosophical Transactions of the Royal Society B: Biological Sciences* 235.629 (Oct. 1951), pp. 509–564. ISSN: 0962-8436.

[17] Paul B Green. “Expression of form and pattern in plants - a role for biophysical fields”. In: *Seminars in Cell & Developmental Biology* 7.6 (1996), pp. 903–911.

[18] Paul B Green. “Pattern Formation in Shoots: A Likely Role for Minimal Energy Configurations of the Tunica”. In: *International Journal of Plant Sciences* 153.3 (1992), S59–S75.

[19] L. F. Hernandez and P. B. Green. “Transductions for the Expression of Structural Pattern: Analysis in Sunflower.” In: *The Plant cell* 5.12 (Dec. 1993), pp. 1725–1738. ISSN: 1532-298X.

[20] J Dumais and CR Steele. “New Evidence for the Role of Mechanical Forces in the Shoot Apical Meristem.” In: *Journal of plant growth regulation* 19.1 (Mar. 2000), pp. 7–18. ISSN: 0721-7595.

[21] P D Shipman and A C Newell. “Polygonal planforms and phyllotaxis on plants.” In: *Journal of theoretical biology* 236.2 (Sept. 2005), pp. 154–97. ISSN: 0022-5193.

[22] Alan C Newell, Patrick D Shipman, and Zhiying Sun. “Phyllotaxis: cooperation and competition between mechanical and biochemical processes.” In: *Journal of Theoretical Biology* 251.3 (2008), pp. 421–39. ISSN: 1095-8541.

[23] K. Okada et al. “Requirement of the Auxin Polar Transport System in Early Stages of Arabidopsis Floral Bud Formation.” In: *The Plant Cell* 3.7 (July 1991), pp. 677–684. ISSN: 1040-4651.

[24] Didier Reinhardt et al. “Regulation of phyllotaxis by polar auxin transport.” In: *Nature* 426.6964 (Nov. 2003), pp. 255–60. ISSN: 1476-4687.

[25] D Reinhardt, T Mandel, and C Kuhlemeier. “Auxin regulates the initiation and radial position of plant lateral organs.” In: *The Plant cell* 12.4 (Apr. 2000), pp. 507–18. ISSN: 1040-4651.

[26] D Reinhardt et al. “Localized upregulation of a new expansin gene predicts the site of leaf formation in the tomato meristem”. In: *Plant Cell* 10.9 (1998), pp. 1427–1437.

[27] Pia A Stieger, Didier Reinhardt, and Cris Kuhlemeier. “The auxin influx carrier is essential for correct leaf positioning.” In: *The Plant Journal* 32.4 (Nov. 2002), pp. 509–17. ISSN: 0960-7412.

[28] Marcus G Heisler et al. “Patterns of auxin transport and gene expression during primordium development revealed by live imaging of the Arabidopsis inflorescence meristem.” In: *Current biology* 15.21 (Nov. 2005), pp. 1899–911. ISSN: 0960-9822.

[29] Olivier Hamant et al. “Developmental patterning by mechanical signals in Arabidopsis.” In: *Science* 322.5908 (Dec. 2008), pp. 1650–5. ISSN: 1095-9203.

[30] Daniel Kierzkowski et al. “Elastic domains regulate growth and organogenesis in the plant shoot apical meristem.” In: *Science* 335.6072 (Mar. 2012), pp. 1096–9. ISSN: 1095-9203.

[31] Benoit Landrein et al. “Meristem size contributes to the robustness of phyllotaxis in Arabidopsis.” In: *Journal of experimental botany* 66.5 (Mar. 2015), pp. 1317–24. ISSN: 1460-2431.

[32] S P Venglat et al. “The homeobox gene BREVIPEDICELLUS is a key regulator of inflorescence architecture in Arabidopsis.” In: *Proceedings of the National Academy of Sciences of the United States of America* 99.7 (Apr. 2002), pp. 4730–5. ISSN: 0027-8424.

[33] A Bogner et al. “A history of scanning electron microscopy developments: towards "wet-STEM" imaging.” In: *Micron (Oxford, England : 1993)* 38.4 (Jan. 2007), pp. 390–401. ISSN: 0968-4328.

[34] P. J. Breton. “From Microns to Nanometers: Early Landmarks in the Science of Scanning Electron Microscope Imaging”. In: *Scanning Microscopy* 13.1 (1999), pp. 1–6.

[35] John N. Owens and Marje Molder. “A study of DNA and mitotic activity in the vegetative apex of Douglas fir during the annual growth cycle”. en. In: *Canadian Journal of Botany* 51.7 (Jan. 1973), pp. 1395–1409.

[36] Paul B. Green and Kenton E. Brooks. “Stem Formation from a Succulent Leaf: Its Bearing on Theories of Axiation”. In: *American Journal of Botany* 65.1 (1978), pp. 13–26.

[37] S. J. Owens and N. J. Horsfield. “A light and electron microscopic study of stigmas in Aneilema and Commelina species (Commelinaceae)”. In: *Protoplasma* 112.1-2 (Feb. 1982), pp. 26–36. ISSN: 0033-183X.

[38] John S. Gardner, W. M. Hess, and E. J Trione. “Development of the Young Wheat Spike: A Sem Study of Chinese Spring Wheat”. In: *American Journal of Botany* 72.4 (1985), pp. 548–559.

[39] Lisa Morrison Baird, Margaret Jorgensen Turano, and Barbara D. Webster. “Ultrastructural and Histochemical Characteristics of the Stigma of Cicer arietinum”. In: *American Journal of Botany* 75.4 (1988), pp. 551–557.

[40] M.H Williams, M Vesk, and M.G Mullins. “Tissue preparation for scanning electron microscopy of fruit surfaces: Comparison of fresh and cryopreserved specimens and replicas of banana peel”. In: *Micron and Microscopica Acta* 18.1 (Jan. 1987), pp. 27–31. ISSN: 07396260.

[41] J Marc and W P Hackett. “Changes in the pattern of cell arrangement at the surface of the shoot apical meristem in Hedera helix L. following gibberellin treatment.” In: *Planta* 186.4 (Mar. 1992), pp. 503–10. ISSN: 0032-0935.

[42] M. H. Williams and P. B. Green. “Sequential scanning electron microscopy of a growing plant meristem”. In: *Protoplasma* 147.1 (Feb. 1988), pp. 77–79. ISSN: 0033-183X.

[43] T A Klar and S W Hell. “Subdiffraction resolution in far-field fluorescence microscopy.” In: *Optics letters* 24.14 (July 1999), pp. 954–6. ISSN: 0146-9592.

[44] Eric Betzig et al. “Imaging intracellular fluorescent proteins at nanometer resolution.” In: *Science* 313.5793 (Sept. 2006), pp. 1642–5. ISSN: 1095-9203.

[45] Pierre Barbier de Reuille et al. “MorphoGraphX: A platform for quantifying morphogenesis in 4D.” In: *eLife* 4 (Jan. 2015), p. 05864. ISSN: 2050-084X.

[46] Magalie Uyttewaal et al. “Mechanical stress acts via katanin to amplify differences in growth rate between adjacent cells in Arabidopsis.” In: *Cell* 149.2 (Apr. 2012), pp. 439–51. ISSN: 1097-4172.

[47] S Webb. *From the Watching of Shadows: The Origins of Radiological Tomography.* 1st Editio. Boca Raton, FL: CRC Press, 1990, p. 347. ISBN: 085274305X.

[48] B. Pollak. “Experiences with Planography”. In: *CHEST Journal* 24.6 (Dec. 1953), p. 663. ISSN: 0012-3692.

[49] T. J. Littleton and M. L. Durzizch Littleton. “Conventional Tomography”. In: *A History of the Radiological Sciences*. Reston, VA: Radiology Centennial, Inc, 1996. Chap. 15, p. 369401.

[50] H Hornich. “A tnrbute to Johann radon.” English. In: *IEEE transactions on medical imaging* 5.4 (Jan. 1986), p. 169. ISSN: 0278-0062.

[51] M S Smyth and J H Martin. “x ray crystallography.” In: *Molecular pathology : MP* 53.1 (Feb. 2000), pp. 8–14. ISSN: 1366-8714.

[52] Romain Fernandez et al. “Imaging plant growth in 4D: robust tissue reconstruction and lineaging at cell resolution.” In: *Nature Methods* May (June 2010). ISSN: 1548-7105.

[53] Scott L. Delp, Anthony M. DiGoia, and Branislav Jaramaz, eds. *Medical Image Computing and Computer-Assisted Intervention – MICCAI 2000*. Vol. 1935. Lecture Notes in Computer Science. Berlin, Heidelberg: Springer Berlin Heidelberg, 2000. ISBN: 978-3-540-41189-5.

[54] O Commowick and G Malandain. “Evaluation of Atlas Construction Strategies in the Context of Radiotherapy Planning”. In: *Proceedings of the SA2PM Workshop (From Statistical Atlases to Personalized Models)*. Copenhagen, 2006, pp. 1–4.

[55] Liselott Slot, Peter K Larsen, and Niels Lynnerup. “Photogrammetric documentation of regions of interest at autopsy–a pilot study.” In: *Journal of forensic sciences* 59.1 (Jan. 2014), pp. 226–30. ISSN: 1556-4029.

[56] F. Chiabrando et al. “Very close nadiral images: a proposal for quick digging survey”. In: *International Archives of Photogrammetry* XXXVIII.5 (2010), pp. 155–160. ISSN: 15740846.

[57] Paz Merelo et al. “Genome-wide identification of KANADI1 target genes.” In: *PloS one* 8.10 (Jan. 2013), e77341. ISSN: 1932-6203.

[58] E. W. Dijkstra. “A note on two problems in connexion with graphs”. In: *Numerische Mathematik* 1.1 (Dec. 1959), pp. 269–271. ISSN: 0029-599X.

# Chapter 4

# Summary of Findings

The aim of this work was to better understand the mechanism that controls organ formation in the Arabidopsis shoot apical meristem. To accomplish this I investigated three aspects of meristem growth and development. First, I tracked cell divisions to understand the factors controlling new wall placement. Second, I measured the affect that cell size plays in controlling placement of new organs (phyllotaxis). Third, I investigated how the size of the meristem affects the phyllotaxis.

## 4.1 Cell Divisions

The morphology of the meristem is dependent on cell divisions and the placement of new walls. To understand how the new walls are positioned I tracked divisions in live plants using time-lapse confocal microscopy. I then converted the image data into 3D coordinates representing cell boundaries and used a mathematical model to understand the properties that best predict the placement of new walls.

I looked at four geometric properties that could potentially affect wall placement and could also be measured in the collected data.

1. Daughter Cell Area ($A$). Measurement of how close the areas of the two daughter cells are from being equal.
2. New Wall Length ($L$). Measurement of how close the new wall is from the shortest possible wall that travels through the center of the mother cell.

3. Growth Direction ($g$). Measurement of how close the new wall is to being perpendicular to the direction of most growth.
4. Primary Axis Direction ($e$). Measurement of how close the new wall is to being perpendicular to the primary axis (longest direction) of the mother cell.

Figure 4.1: Heuristics of cell division.

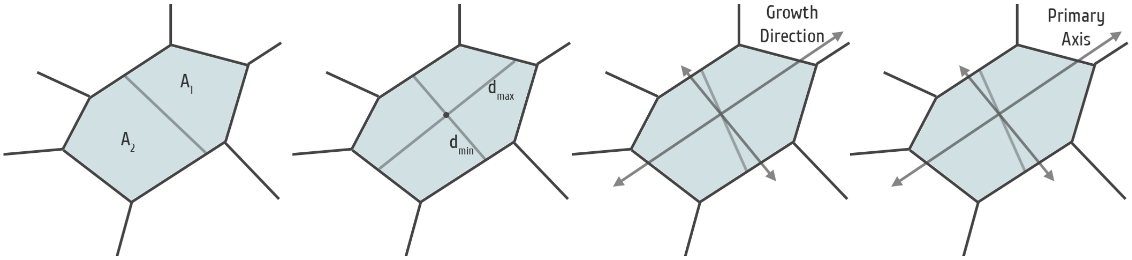

($A$) ($L$) ($g$) ($e$)

Each of those measurements was fed into a corresponding function that compares how close the observed location of the wall ($\Theta_1$) is to the 'ideal' location ($\Theta_2$). The ideal location was the location that minimized a particular geometric property, such as the position where both daughter cells would be exactly equal in area ($V_A$).

$$V_A = \left(\frac{A_1 - A_2}{A}\right)^2 \tag{4.1}$$

$$V_L = \frac{(d - d_{min})^2 + c_L\Delta^2}{(d + d_{min})^2} \tag{4.2}$$

$$V_e = (w \cdot e)^2 + \frac{\varepsilon_g \Delta}{d} \tag{4.3}$$

$$V_g = (w \cdot g)^2 + \frac{\varepsilon_g \Delta}{d} \tag{4.4}$$

Each of the four equations were part of a larger potential function (Equation 4.5). Each of the four components was given its own weight, $w_i$. An optimization algorithm found the optimal weight for each component that minimized the overall potential, essentially indicating which geometric properties are most important for determining the positions of new cell walls.

$$V(\Theta_1, \Theta_2) = \sum_{A,L,e,g} w_i V_i(\Theta_1, \Theta_2) \tag{4.5}$$

The optimal weight vector was determined to be $w = (V_A, V_L, V_e, V_g) = (0.68,\ 0.73,\ 0,\ 0)$. This indicates that the minimization of differences in daughter cell area ($V_A$) and minimization of new wall length ($V_L$) best explain the placement of the new wall. Growth direction ($V_g$) and the length of the cell ($V_e$) are not needed for predicting the location of the new wall.

This result is interesting because our observations show more than 75% of new walls are within 30 degrees of being perpendicular to the primary axis ($e$), far more than would be expected by random chance, even though the model says the primary axis is irrelevant for predicting wall placement. One explanation is that this is a property that emerges in the process of minimizing differences in daughter cell area and new wall length.

This result is also interesting in a historical context as a number of scientists have commented on how different geometric features dictate new wall locations. In particular, Julius von Sachs concluded that new walls split the area of the daughter cells equally while Léo Errera determined that the walls find a minimal length. Both of those assertions were confirmed in this study. Wilhelm Hofmeister determined that new walls form perpendicular to the direction of the primary axis which was determined here to be not true. Although, as just mentioned this phenomenon does seems to emerge frequently as a result of "Sach's Rule" and "Errera's Rule."

## 4.2 Cell Size

The shoot apical meristem is a complex and dynamic system. To better understand which of the many components plays a major role in determining the phyllotaxis pattern I built a large computer model based on other meristem models that tried to incorporate all of the components known to be involved in the patterning process. By running this model many times and changing the values of the parameters I determined that theoretically the two most important factors controlling phyllotaxis were cell size and meristem diameter.

In our current understanding of phyllotaxis (the placement of organs around the meristem), the hormone auxin is pumped out of the cell towards the neighboring cell with the highest concentration of auxin. This creates a positive feedback loop where auxin accumulates in some areas and is depleted from the surrounding areas. New organs form in areas of high auxin. In the model diffusion of auxin across the cell is instantaneous and as a result the limiting factor is the transport rate across the membrane. So the localization of auxin is mostly dependent on the number of walls around the meristem. But this model property does not necessarily represent reality. It is possible that auxin takes considerable time to diffuse through the cytoplasm. If intracellular diffusion is the limiting factor then the number of membranes around the meristem should be irrelevant. In this case the absolute distance between organs should be consistent regardless of how large or small the cells in a particular mutant are.

To test this I measured cell sizes and the distances between organs in mutants that had cells of varying sizes. The mutants *Wa-1* and *cycD3;1-3* had larger cells than wild type while *msc3* had smaller cells. I used confocal microscopy followed by 3D image processing algorithms to extract the dimensions of the cells and morphology of the meristems. These data were then used to make the measurements of cell size and organ positions.

I measured the diameters of cells and the distances and number of cells between subsequent organs. The mean number of cells between organs within a given genotype was between 10 and 12 but the individual measurements had a much higher variability. The absolute distance between organs in large-cell mutants was about twice that of wild-type-sized plants. When I divided the distances between organs by the root of the cell areas (which should be approximately the width of the cell) the distances between organs was very consistent between genotypes. These results indicate that the assumption of the model was correct. The limiting factor in auxin movement is transport across the membrane rather than intracellular diffusion. Further, cell size does impact the placement of organs. Although, the effect is not very noticeable on the macroscopic scale as the meristems in large cell mutants are also enlarged which compensate by having approximately the same *number* of cells as wild type.

Figure 4.2: Effect of cell size on auxin patterning in the shoot apical meristem.

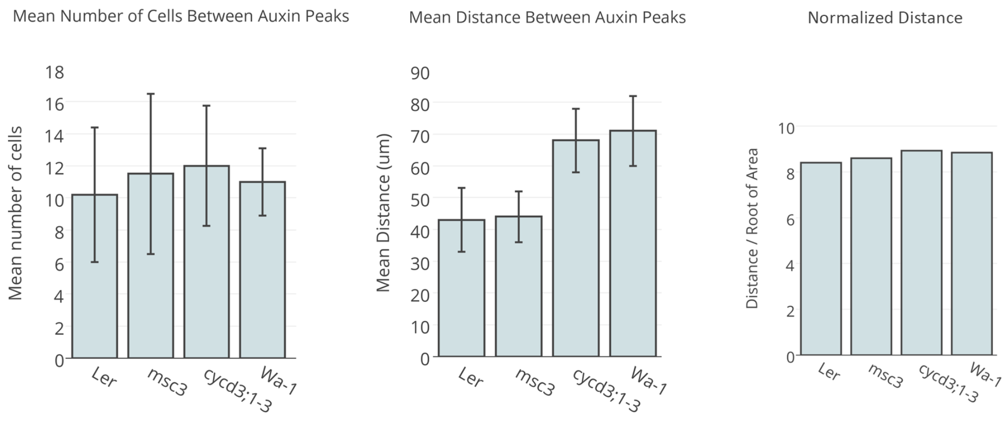

In addition to the meristem, I also explored the effect of cell size on patterning in the roots, leaf margins and shoot vasculature. In the roots, cell size mutants displayed disorganized auxin patterns but overall normal morphology. In areas where auxin would normally accumulate prior to lateral root formation, my fluorescent auxin reporter was not visible but the lateral roots still formed. This is perplexing and indicates that my model of auxin transport in the meristem is insufficient for explaining root development.

In leaves, auxin is transported around the periphery during early development using many of the same components as in the shoot meristem. In areas of high auxin, serrations form through accelerated growth. If cell size plays a role in auxin distribution here then I would expect cell size mutants to have a corresponding change in number of serrations. *msc3* mutants have leaf cells of approximately half the width of wild type cells. Therefore that mutant should have twice as many serrations as wild type. Likewise, the large cell mutants have cells about twice as wide as wild type and should have about half as many serrations.

The data show that *msc3* mutants have about 25% more serrations and large cell mutants have about 33% fewer. So while the direction of change is as predicted, the *magnitude* of change is not what I would expect. My conclusion on leaf serrations is that the model of cell size controlling auxin distribution is not applicable in this tissue.

Figure 4.3: Effect of cell size on auxin patterning in the shoot vasculature (left) and leaf boundary (right).

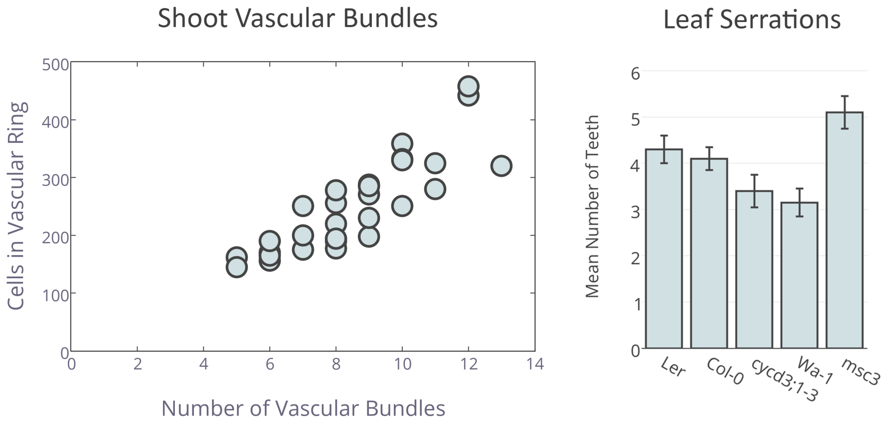

In the shoot vasulature, auxin is thought to be transported around the vascular ring causing vascular bundles to form in areas of high auxin. I counted vascular bundles and number of cells around the ring in the same cell size mutants as before. The data show a linear relationship between number of cells in the ring and number of bundles. So it is possible that the transport-limited auxin model is applicable in this tissue.

Overall, the model is able to closely predict the patterning in the shoot meristem and shoot vasculature but fails in the leaves and roots.

## 4.3 Meristem Size

The other major hypothesis generated by the computer model is that meristem diameter should affect the phyllotaxis pattern by altering the divergence angles between successive organs. In the model this phenomenon was closely tied to the cell-size phenomenon as increasing the size of the meristem increased the number of cells present. Shrinking the cells had many of the same effects as enlarging the meristem.

To test if this happens in reality I measured the sizes of meristems and the divergence angles in a number of mutants with different sized meristems. This required me to develop some new techniques for image processing and analysis.

For determining the size of the meristem I developed a image processing software pipeline that took 3D confocal stacks of meristems, extracted the topology of the meristems and identified important landmark features. To quantify the radius I measured from the apex of the meristem to the nearest crease in between the meristem and the early organ primordium. To quantify divergence angles I initially developed a tomographic imaging technique but soon discovered that the time required per plant was exceeded the time required to measure the angles manually with a divergometer.

Figure 4.4: Mean and median divergence angles as a function of mean meristem radius.

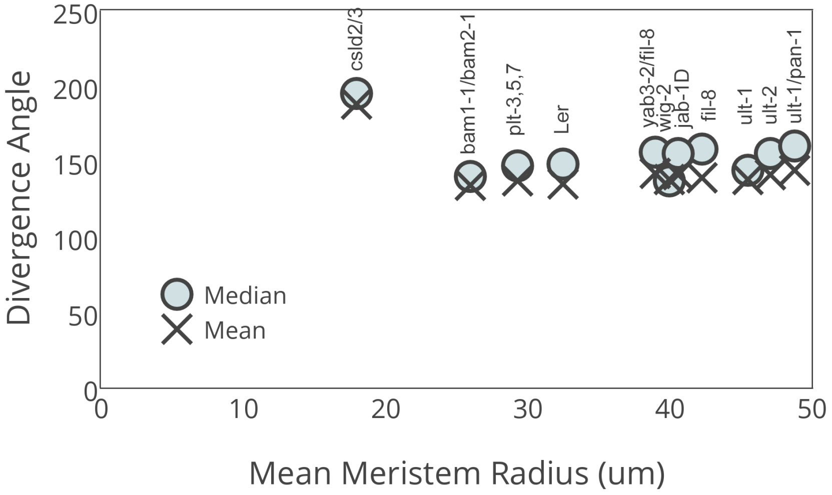

Using these two techniques I measured the meristem sizes and divergence angles of 12 different genotypes. The mean values for these measurements are not particularly interesting. While there is a wide variety of meristem radii, the mean divergence angle is approximately equal in all but one genotype. In that genotype the meristem has about half the radius of wild type and shows a much larger divergence angle. This is apparent at the macroscopic level as the plants have an obvious alternating pattern where each successive flower is about 180 degrees from the previous flower. Most genotypes appear normal to the naked eye.

The distributions of divergence angles of individual genotypes shows more variability than simply looking at means. In many of the genotypes, like the *yab3-2 / fil-8* for example, the mean remained around the "canonical" 137 degree mark but showed a greater number of angles further away from the mean wild type. These non-canonical divergence angles show that the phyllotaxis is being affected by the changes to the meristem even though the mean remains the same.

Figure 4.5: Comparison of distributions of divergence angles of wild type and a mutant.

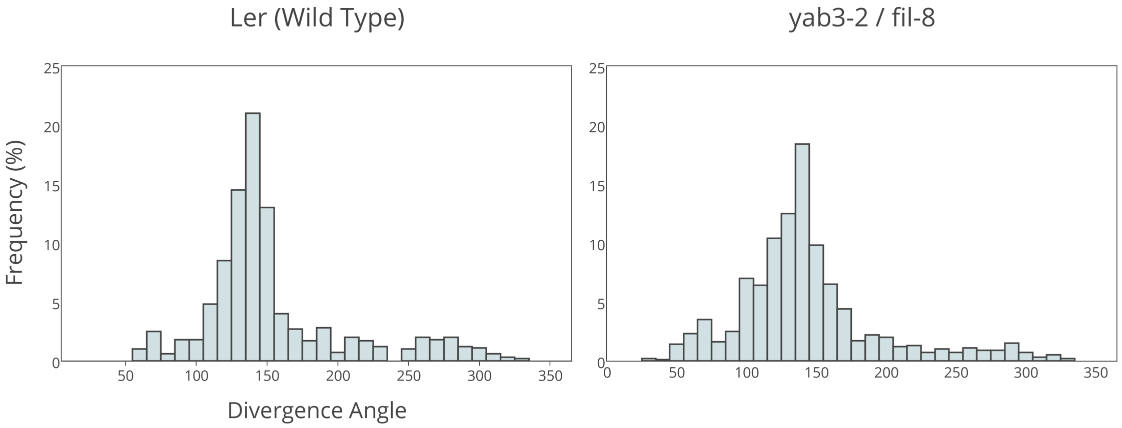

So the hypothesis is partially true in that altering the size of the meristem changes the divergence angles. But the pattern is more robust in plants than in the model. Most changes to the meristem result in very minor changes to the phyllotaxis. Although, it is possible to get more noticeable phenotypes as seen in the model by shrinking the meristem considerably. Presumably there is also an upper threshold where the phyllotaxis will significantly change when the meristem gets large enough.

## 4.4 New Model

The conclusion I have drawn from this research is that our model, while accurately representing reality in some conditions is not sufficiently complete to explain all of the observed phenotypes. As we gain understanding of more components the model will need to be revised to incorporate these new insights.

Along these lines, one of our colleagues has shown that the size of the central zone is critical for modelling phyllotaxis and that the central zone changes in plants with altered meristem size. The central zone is a region of cells in the center of the meristem where auxin accumulation and differentiation is inactive. Changing the size of this region would change the number of cells auxin needs to be transported through in order to achieve the same divergence angles. So a model that captures this phenomenon would probably be a better representation of reality and help us better understand phyllotaxis in the future.